



HAL
open science

Numerical study of femtosecond laser interactions with dielectric materials: application to the definition of damage threshold of optical components

Nikita Shcheblanov

► **To cite this version:**

Nikita Shcheblanov. Numerical study of femtosecond laser interactions with dielectric materials: application to the definition of damage threshold of optical components. Optics [physics.optics]. Université Jean Monnet - Saint-Etienne, 2013. English. NNT : 2013STET4029 . tel-01124302

HAL Id: tel-01124302

<https://theses.hal.science/tel-01124302>

Submitted on 6 Mar 2015

HAL is a multi-disciplinary open access archive for the deposit and dissemination of scientific research documents, whether they are published or not. The documents may come from teaching and research institutions in France or abroad, or from public or private research centers.

L'archive ouverte pluridisciplinaire **HAL**, est destinée au dépôt et à la diffusion de documents scientifiques de niveau recherche, publiés ou non, émanant des établissements d'enseignement et de recherche français ou étrangers, des laboratoires publics ou privés.

Université Jean Monnet - Saint-Étienne

L'école doctorale - “Sciences, Ingénierie, Santé”

**Etude numérique des interactions d'un laser femtoseconde avec des cibles
dielectriques: applications à la détermination du seuil d'endommagement des
composants optiques**

par

Nikita SHCHEBLANOV

**Thèse présentée pour obtenir le grade de Docteur en Sciences
en spécialité Optique, photonique et hyperfréquences**

9 avril 2013

Jury :

Mme. APOSTOLOVA Tzveta, rapporteur

M. BOUKENTER Aziz examinateur

M. DUCHATEAU Guillaume, examinateur

M. GUIZARD Stéphane, rapporteur

Mme. ITINA Tatiana, directrice de thèse

Jean Monnet University – Saint-Étienne

**Numerical study of femtosecond laser interactions with dielectric materials:
application to the definition of damage threshold of optical components**

by

Nikita SHCHEBLANOV

Thesis presented

for the Doctoral degree in Sciences

(major: Optics, photonics and hyperfrequencies)

9 April 2013

Jury:

Mme. APOSTOLOVA Tzveta, rapporteur

M. BOUKENTER Aziz, examinateur

M. DUCHATEAU Guillaume, examinateur

M. GUIZARD Stéphane, rapporteur

Mme. ITINA Tatiana, directrice de thèse

Content

Chapter 1. Introduction	8
1.1 Applications of femtosecond laser pulses	9
1.2 Theoretical and experimental approaches	13
1.3 Open questions, objectives of the present work and manuscript's organization	15
Chapter 2. Main physical processes occurring during ultra-short laser interactions with dielectric materials: Modeling details	17
2.1 System of Boltzmann equations	18
2.1.1 Main physical processes.....	19
2.1.2 Applicability.....	21
2.2 Photoionization process	22
2.2.1 Fundamentals.....	22
2.2.2 Photoionization rate.....	23
2.2.3 Photoionization collision integral.....	24
2.3 Electron-electron scattering process	26
2.3.1 Fundamentals.....	26
2.3.2 Electron-electron scattering rate.....	27
2.3.3 Electron-electron collision integral.....	27
2.4 Impact ionization process	28
2.4.1 Fundamentals.....	28
2.4.2 Impact ionization rate.....	29
2.4.3 Impact ionization collision integral.....	29
2.5 Electron-phonon scattering process (in present/absence of laser wave field)	31
2.5.1 Fundamentals.....	31

2.5.2	Electron-phonon scattering rate.....	33
2.5.3	Electron-phonon collision integral.....	34
2.6	Electron-ion scattering process (in present/absence of laser wave field).....	37
2.6.1	Fundamentals.....	37
2.6.2	Electron-ion scattering rate.....	37
2.6.3	Electron-ion collision integral.....	38
Chapter 3.	Results and discussions.....	39
3.1	Photoionization process.....	40
3.1.1	Role of field amplitude.....	40
3.1.2	Role of laser wavelength.....	42
3.1.3	Structure of above-threshold ionization.....	44
3.1.4	Extreme cases (regimes) of photoionization process.....	46
3.2	Impact ionization process.....	51
3.2.1	Role of laser field amplitude.....	51
3.2.2	Role of laser wavelength.....	52
3.2.3	Screening and free electrons.....	53
3.3	Electron heating.....	54
3.3.1	Heating through the photoionization process.....	54
3.3.2	Heating through the electron-phonon/ion process.....	55
3.4	Heating process and optical properties: QM versus Classical (Drude).....	59
3.5	Nonequilibrium state of electronic subsystem.....	70
3.6	Time observation of the ultrafast excitation/relaxation.....	73
Chapter 4.	On the damage criterion.....	78
Chapter 5.	General conclusions.....	82
Perspectives.	85

Appendix A. Validity	86
Appendix B. Special functions	87
Appendix C. Delta-function approximation	88
Appendix D. Integration and derivation schemes	89
Appendix E. Photo-ionization matrix element derivation	90
Appendix F. Reference data of target properties (SiO₂)	91
Appendix G. Photo-ionization rate expressions	92
Appendix H. Electron-electron collision integral	94
Appendix I. Auger scattering rate	97
References	98
Abstract	114

Chapter 1

Introduction

1.1 Applications of femtosecond laser pulse

With the appearance of new ultra-short laser systems, extremely high laser intensities became accessible thus allowing laser treatment of practically all materials. As a result, extremely precise processing techniques are under development considerably extending the number of the corresponding industrial and medical applications [1,2]. Femtosecond laser marking and machining are thus used in optics, photonics, counterfeiting, ophthalmology and other fields.

The advantage of material processing with femtosecond pulses is most obvious for wide-gap dielectrics, which are transparent to near infrared and visible laser light. Unlike materials such as metals and semiconductors, the possibility of laser machining of dielectric materials is not straightforward. Not only can the high peak power of femtosecond pulses turn these materials into absorbing targets, but also the involved nonlinear absorption processes may lead to a high precision of laser treatment [3]. These effects, together with the associated deterministic breakdown thresholds, make femtosecond machining particularly attractive [4,5,6,7] for microstructuring. The required ultra-short lasers have become available during last decade with the development of several commercial systems, such as Titan:Sapphire. The average power of these systems is limited, typically not exceeding 10 W, but high enough for numerous industrial applications.

During last decade, several important features of femtosecond laser ablation (as opposed to machining with nanosecond pulses) were underlined [3], as follows

- (i) it is possible to process transparent materials;
- (ii) very regular damage patterns as well as a higher reproducibility of structures from shot to shot were obtained [8];
- (iii) high intensities in the focal region at low average power result in low thermal effects;
- (iv) the penetration depth of the pulses can be controlled by changing the pulse duration; it can be as short as 100 nm [9];
- (v) only a small fraction of pulse energy is converted to heat and momentum (small heat-affected zone or shock-affected zone) [10].

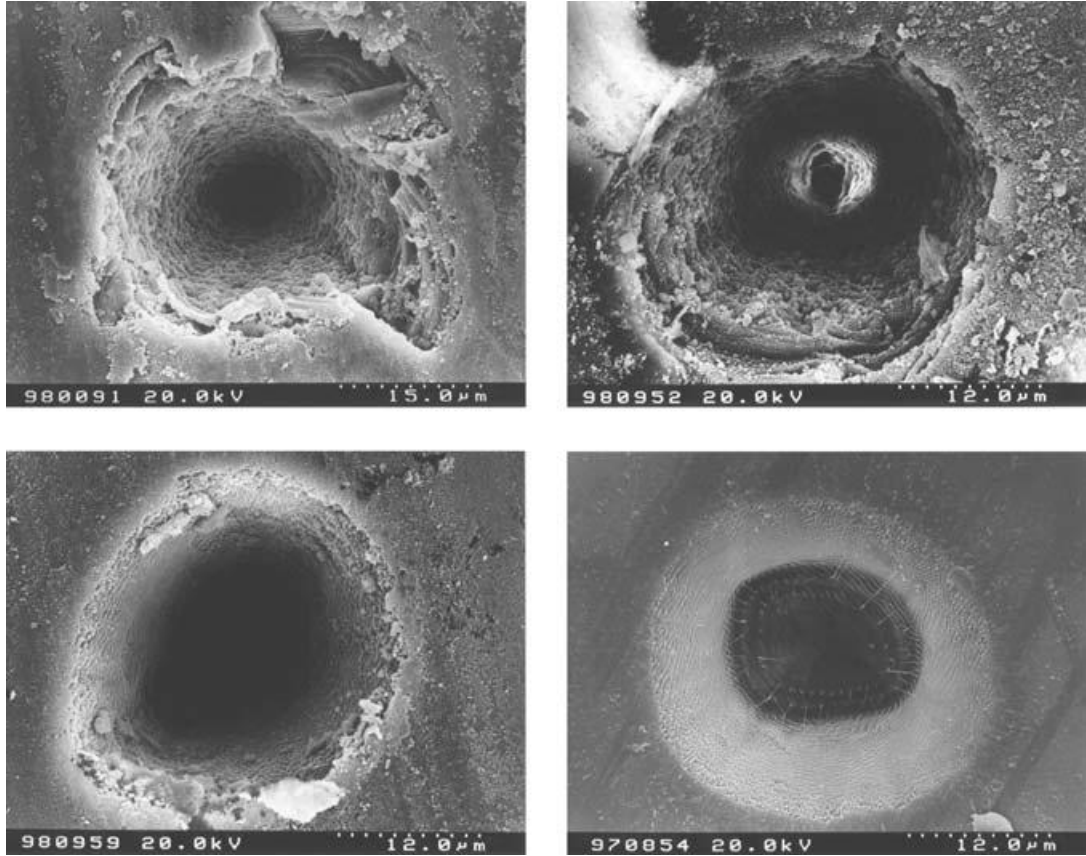


Fig. 1.1. Scanning electron micrographs of fused silica ablated by ultrashort laser pulses [3] with a peak fluence of F_0 , $\lambda = 780$ nm, 80 shots. Pulse duration and fluence are (upper left) $\tau_p = 3$ ps, $F_0 = 19.9$ J/cm²; (upper right) $\tau_p = 220$ fs, $F_0 = 10.7$ J/cm²; (lower left) $\tau_p = 20$ fs, $F_0 = 11.1$ J/cm²; (lower right) $\tau_p = 5$ fs, $F_0 = 6.9$ J/cm².

To qualitatively demonstrate this phenomenon, typical ablation pictures taken from a scanning electron microscope are shown in Fig. 1.1 for fused silica. The holes are obtained for different pulse durations between 5 fs and 3 ps and machined with 80 pulses from a Ti:Sapphire laser system at a repetition rate of 1 kHz. It is obvious that the 5 fs ablation morphology (Fig. 1.1, lower right) is much more precise/deterministic than in the case of longer pulses (Fig. 1.1, upper row). The differences are visible even when compared with the 20 fs pulses (Fig. 1.1, lower left). Although the applied fluence is higher for the picosecond pulses, similar damage threshold fluence can be observed for all pulse durations. A more stochastic behavior of long-pulse ablation accounts for the difference in the hole's edge quality, as will be explained in Section 2.

For materials such as metals or semiconductors, thermal effects play a role and their effect rises with pulse duration. In fact, in these materials free carriers transfer energy to the lattice on a time scale of a few ps, after which melting and evaporation occur. By carefully choosing the parameter range (wavelength, pulse duration, fluence) for laser processing, one can structure these materials with the same high precision using more cost-efficient, longer-pulse, laser systems. Another interesting application of high-intensity laser pulses is laser processing of

transparent materials in bulk. Not only can decorative accessories be produced in this way, but also three-dimensional optical waveguides can be written within such materials [11]. The physical mechanisms of the laser-induced permanent modification of the refractive index is not completely understood. Structural changes of the atomic network rather than optical breakdown are likely to occur [12]. At higher intensities, these material can be also ablated. For instance, microfluidic devices can be manufactured by using this technique [13].

Further progress in these areas requires a better understanding of fundamental processes involved in the laser interactions. In addition, the success of several international projects [French “Laser Mega Joule” project, LMJ (Fig. 1.2), American “National Ignition Facility” project, NIF (Fig. 1.3)] involves the development and use of high power laser systems and depends on the capacity of careful definition of damage threshold of the optical components.

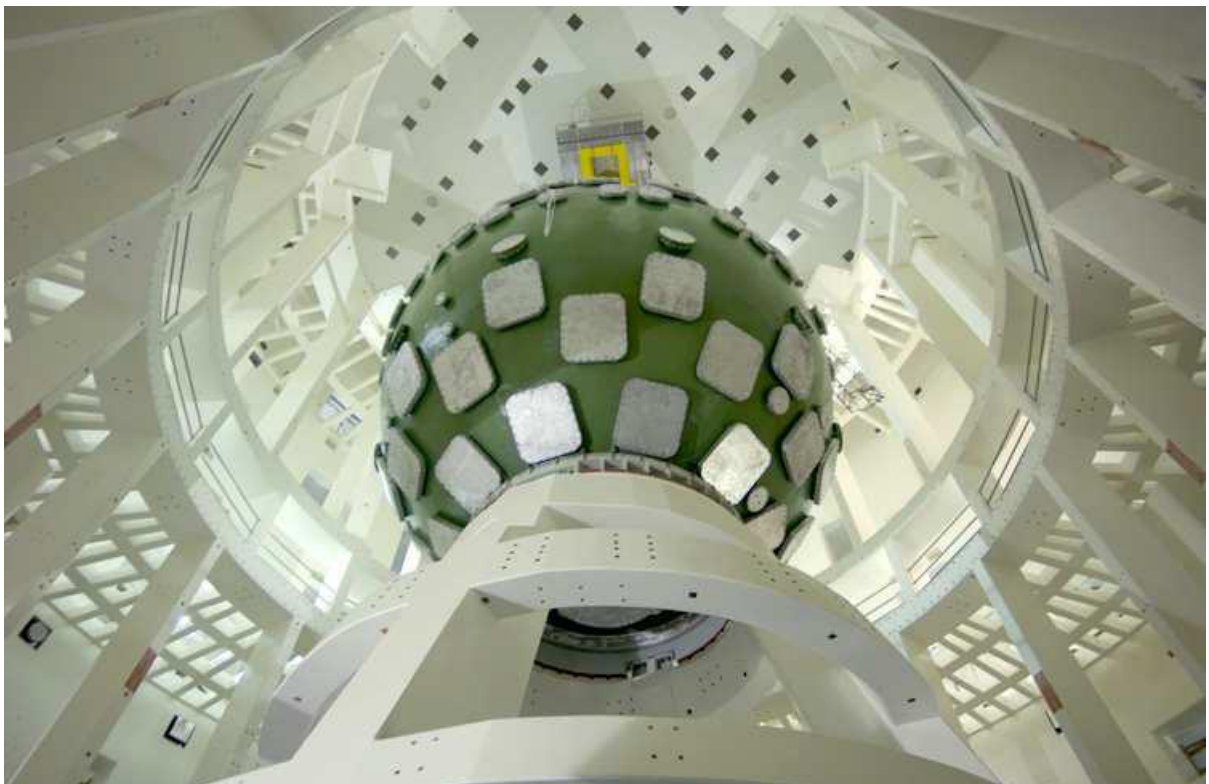


Figure 1.2. LMJ experimental chamber. Laser MégaJoule Project, <http://www-lmj.cea.fr>.

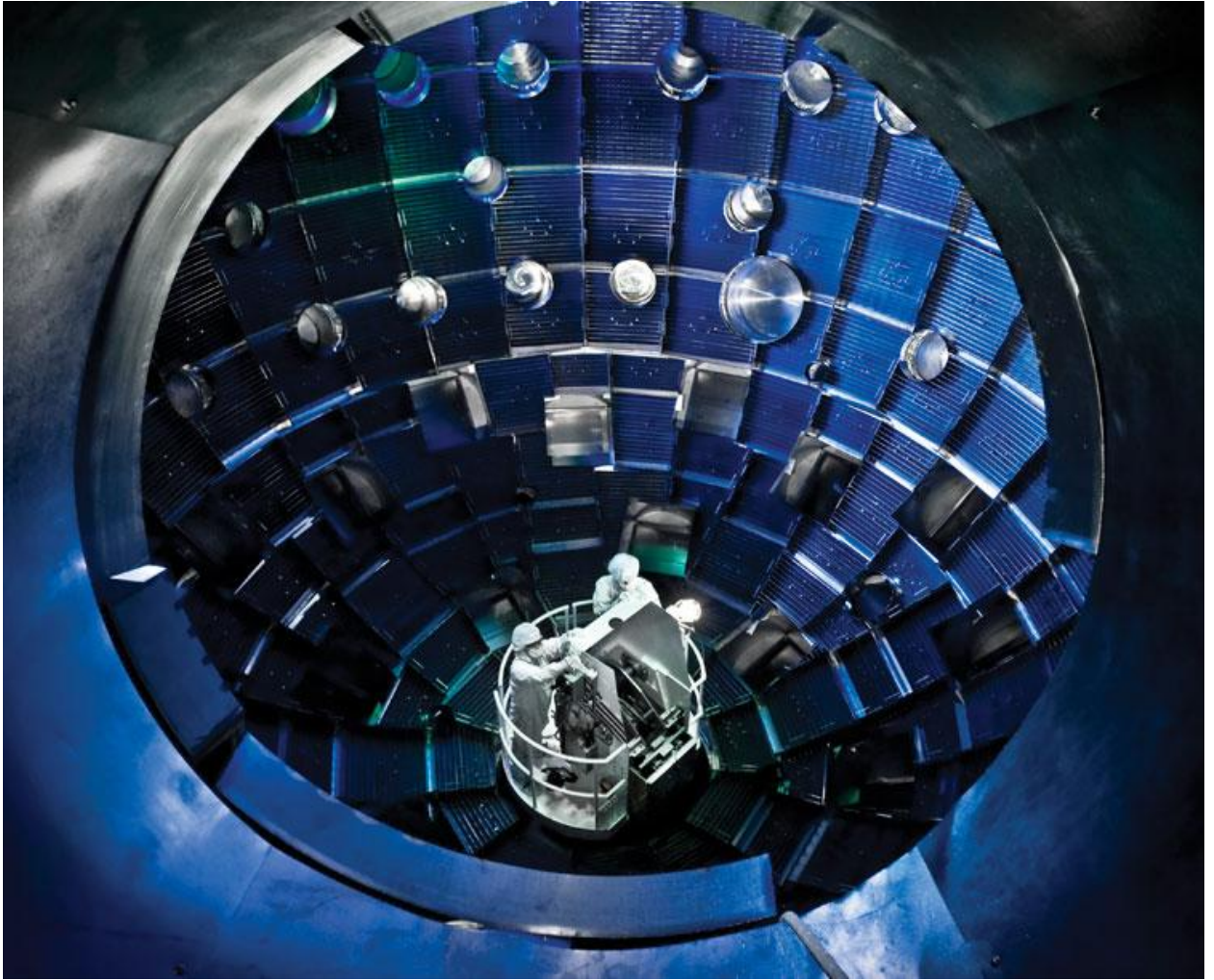


Fig. 1.3. NIF experimental chamber. National Ignition Facility Project, <http://lasers.llnl.gov>.

These points illustrate the importance of a detailed numerical modeling of laser interactions with dielectric materials. In ultra-short laser interaction with dielectric materials, particular attention should be paid to such process as laser-induced electronic excitation, absorption, and relaxation processes. In fact, upon laser irradiation, seed electrons appear in the conduction band of the dielectric materials first due to the photo-ionization process [14,15,16,17]. Colliding with a third-body, these electrons are further heated in laser field. When the threshold electron energy is reached, electron-impact ionization begins. At the same time, the considered laser pulses are so short that the electron sub-system has no time to reach an equilibrium state. The resulting optical properties are thus affected and the definition of the damage criterion should be revised for such non-equilibrium conditions [18,19,20,21,22].

§1.2 Theoretical and experimental approaches

A large number of both experimental and theoretical studies were performed to elucidate the mechanisms of femtosecond laser interactions with transparent materials and to find a possibility of better control over the laser-induced material modifications [23,24,25,26,27,28,29,30,31,32,33,34,35,36,37,38]. Some of these investigations were focused on the effects of non-linear laser propagation in dielectric materials [39,40]. Other studies were mostly focused on material ionization and plasma formation [13,41,42,43,44,45,46,47,48,49,50]. In particular, such strongly non-linear effects as self-focusing, filamentation, multi-photon and tunneling ionization were demonstrated. Several numerical calculations were performed, based both on non-linear Schrödinger equation [39,40], and on full Maxwell equations [51]. To complete these calculations, material ionization models were developed. In particular, Keldysh proposed theoretical treatment of non-linear photo-ionization processes [41,52,53]. In addition, such processes as electron-impact ionization, and electron energy relaxation were also investigated. Several numerical techniques were used in previous calculations of electronic excitation, ranging from quantum mechanics, *ab initio* [25,54] and solutions of the Boltzmann equation by the Monte Carlo method [55,56], numerical solutions by the difference method [14,34,57], and the Fokker-Plank approximation [15,50,58,59,60] to the simplified rate equations [26,28,35]. These calculations revealed many characteristic features of femtosecond laser interactions. In particular, the mechanisms of laser damage and ablation were discussed and threshold laser fluences required to induce laser damage or ablation was examined as a function of laser parameters [24,26,28,31,32,33,35].

Despite a variety of previous studies, the correct definition of the damage threshold remains challenging and unclear both in the experiments and in theoretical models. The proposed criteria were often based on simple models disregarding strong deviations from equilibrium that typically occur in the electron sub-system upon femtosecond interactions. The non-equilibrium electron sub-system was also considered in several papers [14,15]. These calculations provided an information about the relaxation time for metal and dielectric materials, as well as about the final density of the electrons injected in the conduction band (CB) due to both photo-ionization and electron-impact ionization processes. In addition, the role of laser pulse duration in the elucidation of the prevailing ionization mechanism was investigated [61]. Recently, a precise experimental procedure was proposed [62]. In addition, new theoretical criteria were also introduced [35,63,64]. However, many issues are still puzzling. For instance, it is unclear how the calculation results depend on the band structure and on laser parameters. In fact, parabolic band structure was set in most of previous calculations. Moreover, the density of the created electrons in the conduction band (CB) depends strongly on both laser intensity and pulse duration. In addition, it is unclear if Drude model is applicable for the calculation of the heating of the CB electrons. A detailed investigation of these processes is, therefore, required to better understand ultra-short laser interactions with dielectric materials.

Strictly speaking, classical continuum models [33] are not suitable for description of the ultra-short laser excitation. This fact is a direct consequence of the time and space scales of the

processes taking place due to action of the laser irradiation. In fact, both the electron and lattice subsystems strongly deviate from the equilibrium states during the laser pulse. Therefore, to describe these subsystems on the sub-picosecond time scales we apply a kinetic approach based on Boltzmann equation. Furthermore, this approach does not require using high performance computer, contrary to the one based on the Kadanoff-Baym equation by *Otobe* [25]. Our model is based on the *Kaiser* model [14]. The advantages of this method are the following: (i) the model has no approximations, such as the one used by *Epifanov et al.* [59]); (ii) all of the basic mechanisms that influence the kinetics and excitation are taken into account (no phenomenological models, such as Drude model, are used) [60]; (iii) all necessary data, such as parameters of electron-phonon interaction is available for the calculations; and (iv) the proposed model has no adjustable parameters. Additionally, we show how to extend Kaiser's approach by a more detailed consideration of the mechanisms of photoionization and absorption of laser radiation, which are discussed in the Chapter 2.

The proposed approach accounts for the non-equilibrium and provides a detailed description of the major processes involved in the laser interactions. In particular, we consider the photo- and impact- ionization processes, as well as electron-electron, electron-phonon and electron-ion collisions.

The electron energy distribution and heating of electron subsystems is discussed. The role of laser parameters (wavelength, pulse duration, fluence) and material properties (energy gap, band structure) is investigated. The thermalization time is calculated and characterizes the non-equilibrium state as a function of laser pulse duration. A novel thermal criterion is proposed for damage definition based on the electron and phonon energies. The calculated damage thresholds are compared with recent experimental findings. An analysis of the classical (Drude) model and optical breakdown-based criterion is also performed.

1.3 Open questions, objectives of the present work and manuscript's organization

Despite a large number of the previous studies, many questions are still open in the field of ultrashort laser interactions with dielectric materials. In particular, the following points are unclear

(i) role of the laser pulse parameters, material properties and different mechanisms (Umklapp processes and electron-ion collisions) in the electron heating due to the action of the sub-picosecond laser pulses in the wide bandgap dielectrics;

(ii) role of the laser pulse parameters, material properties and basic mechanisms (photo-ionization, impact- and field-assisted impact- ionization) in the electron generation due to the action of the sub-picosecond laser pulses in the wide bandgap dielectrics;

(iii) change in the optical properties during the laser pulse in the wide bandgap dielectrics;

(iv) time thermalization (non-equilibrium problem);

(v) difficulty to determine the adequate damage criterion for the sub-picosecond laser pulses based on both laser pulse parameters and material properties.

To shed light on these puzzling issues, a detailed numerical investigation is required based on a rigorous numerical calculations and a comparison with the most accurate experimental measurements. In this manuscript, I present the results of my work at the Hubert Curien Laboratory that I performed in the frame of my PhD studies at the University Jean Monnet/Lyon (2009-2013). The main objectives of this work are the following

(i) to investigate all possible heating mechanisms which take place on the fs-time scales and to determine the role of each one of them;

(ii) to examine all possible generation mechanisms which take place on the fs-second time scales and to determine the role of each one of them;

(iii) to propose a new adequate definition of the damage criterion based on both laser pulse parameters and material properties and to verify it through the comparison with recent experiments.

For this, I have developed a computer code based on Boltzmann equation. This code has been used for a series of calculations that permit me to obtain the results presented in the present manuscript. The thesis is organized as follows

- After a brief description of the applications and previous studies given in the present Introduction (Chapter 1), Chapter 2 is focused on the description of the model. Here, the main processes and the corresponding equations are described. In particular, I present the description

of the photoionization process, impact ionization process, electron-electron scattering process, electron-phonon scattering process (in present/absence of laser wave field), and electron-ion scattering process (in present/absence of laser wave field). I would like to note that despite the fact that some of the equations were already used in previous studies, I have introduced the correct definition of the photoionization collision integral and corresponding rates; the Umklapp processes in the electron-phonon collisions and additional and correct phonon modes with respect to Kaiser's work [14], the electron-ion collisions, which are new and the importance of these term will be demonstrated.

- Chapter 3 summarizes the main calculation results. In details, one can find here the discussions of (i) the role of laser field amplitude, wavelength and materials properties in the photoionization process; (ii) the role of laser field amplitude, wavelength, and screening effect in the impact ionization process; (iii) the role of the photoionization, electron-phonon, electron-ion processes in the electron heating; (iv) optical properties and comparison with classical (Drude) model; (v) the non-equilibrium electronic subsystem state; (vi) time observation of the electronic excitation/relaxation dynamics and comparison with experimental data.

Among the novel and original results my work has demonstrated the following (a) the importance of the band structure in the PI processes; (b) the role of laser wavelength in the calculation of the mean energy of electron sub-system is clearly shown for the first time; (c) the role of the *Umklapp* processes that are included in both the electron-phonon collisions and in the electron-ion collisions to describe correctly the laser energy deposition; (d) the limits of validity of Keldysh equation at large laser intensity is underlined; (e) for the first time, I have compared free-carrier absorption based on the classical Drude model with the one based on the presented quantum mechanical description; (f) the electron thermalization process is examined as a function of laser parameters; (g) the confirmation of the time observation of the electronic excitation/relaxation dynamics experimental results is demonstrated; (h) the avalanche model is analyzed as a function of laser parameters, and a comparison with previous experiments is performed.

- Chapter 4 is focused on the determination of the damage threshold. This question is very important and the answer to it is very puzzling. Previously, several criteria were proposed. Here, I propose a new one based on the comparison of the electron energy density with that of phonon sub-systems.

General conclusion summarizes the main results of my work. I will also emphasize the importance of the results including both theoretical and practical aspects. Perspectives are finally presented, including both further theoretical development and practical applications.

Chapter 2

Main physical processes occurring during ultra-short laser interactions with dielectric materials: Modeling details

§2.1 System of Boltzmann equations

The evolution of the electron sub-system is considered by using Boltzmann equation (BE). The distribution function of the conduction band electrons in the phase space (\mathbf{r}, \mathbf{k}) is called f . This function depends on the position \mathbf{r} , on the wave vector \mathbf{k} , and on time t . Then, the Boltzmann equation is given by [65,66,67,68,69,70,71]

$$\left(\frac{\partial}{\partial t} + \frac{\hbar \mathbf{k}}{m_{cb}} \nabla_{\mathbf{r}} + \frac{\mathbf{F}(\mathbf{r}, t)}{\hbar} \nabla_{\mathbf{k}} \right) f(\mathbf{r}, \mathbf{k}, t) = \sum \left. \frac{\partial f}{\partial t} \right|_{CI}, \quad (2.1)$$

where m_{cb} is the effective mass of the free colliding electron, and $\mathbf{F}(\mathbf{r}, t)$ is the force acting on the electron conservative force field.

Spatial effects can be neglected if laser field is homogeneous in space. Furthermore, the effect of the field is taken into account directly in the collision integrals [72,73,74]. Then, the equation takes the following form

$$\frac{d}{dt} f(\mathbf{k}, t) = \sum \left. \frac{\partial f}{\partial t} \right|_{CI}. \quad (2.2.1)$$

Because electrons interact with phonons, additional equations for the phonon subsystem should be added. The model also assumes a local homogeneous space with respect to the phonons. An analogy with the equation (2.2.1) results in a Boltzmann equation for the phonons. Here, the electron distribution function $f(\mathbf{k}, t)$ is replaced by the $g_{\beta}(\mathbf{q}, t)$, where the index β denotes the phonon mode, \mathbf{q} is the phonon wave vector. Thus, the equations for the phonon modes are

$$\frac{d}{dt} g_{\beta}(\mathbf{q}, t) = \sum \left. \frac{\partial g_{\beta}}{\partial t} \right|_{CI}. \quad (2.2.2)$$

Completing the BE equations by the initial conditions, we obtain the following system of equations to be solved

$$\left\{ \begin{array}{l} \frac{d}{dt} f(\mathbf{k}, t) = \sum \left. \frac{\partial f}{\partial t} \right|_{CI} \\ f(\mathbf{k}, t=0) = f_0(\mathbf{k}) \\ \frac{d}{dt} g_{\beta}(\mathbf{q}, t) = \sum \left. \frac{\partial g_{\beta}}{\partial t} \right|_{CI} \\ g_{\beta}(\mathbf{q}, t=0) = g_{\beta,0}(\mathbf{q}) \end{array} \right. . \quad (2.3)$$

The collision terms, $\sum \left. \frac{\partial f}{\partial t} \right|_{CI}$ and $\sum \left. \frac{\partial g_{\beta}}{\partial t} \right|_{CI}$ are composed of separate collision integrals

describing the individual scattering processes. In what follows, we present them in more detail.

2.1.1 Main physical processes

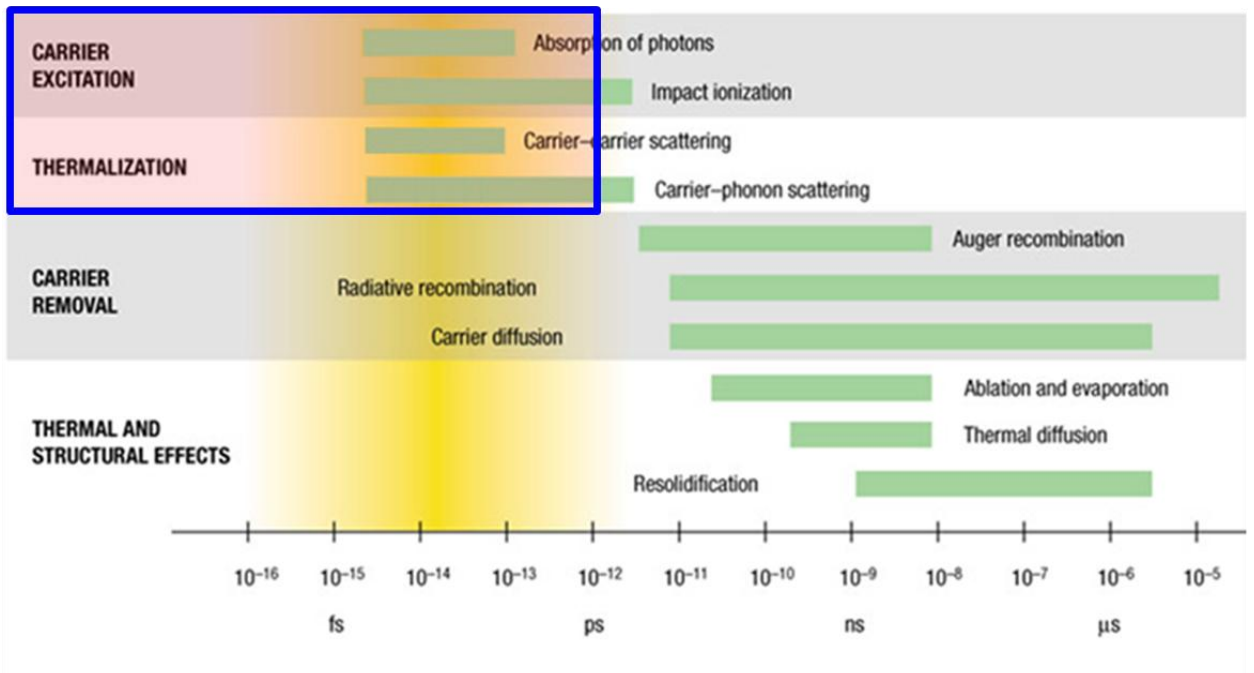


Figure 2.1. General schematics of excitation/relaxation processes in an insulator [75].

Since we consider femtosecond time scales (Fig. 2.1), the following electron scattering processes are taken into account in our model

- (i) *Photoionization collision integral (p_i)*

The photoionization collision term describes the electron transitions from the valence band to the conduction band under the action of the laser irradiation.

- (ii) *Electron-electron collision integral ($e-e$)*

The electron-electron collision term describes the collisions between two electrons in the conduction band.

- (iii) *Electron-phonon collision integral ($e-ph$)*

The electron-phonon collision term describes the collisions between conduction band electrons and phonons. The electron can emit and absorb the phonons.

(iv) *Electron-phonon-photon collision integral (Index: e-ph-pht)*

The electron-phonon-photon collision term describes collisions between conduction band electrons and phonons in external laser field. The electrons emit and absorb photons and occupation numbers of electrons and phonons change due to these collisions.

(v) *Electron-ion-photon collision integral (Index: e-ion-pht)*

The electron-ion-photon collision term describes collisions between conduction band electrons and ions in external laser field. The electrons emit and absorb photons due to these collisions, but the ion state does not change.

(vi) *Impact ionization collision integral (Index: imp)*

The impact ionization collision term describes collisions between two electrons, from conduction band and valence band. The conduction band electron transfers energy to the valence band electron and the valence band electron transits to the conduction band in result of this process.

The spatial dependency is neglected. Thus, the electron occupancy of f and the phonon occupancy of g_β are calculated in a point, and no transport processes is considered here.

The occupation numbers and the momentum space of the electron and phonon wave vector are set to be isotropic. Thus, the occupations (distribution functions) depend only on the absolute value of the wave vectors and not on their directions. Then, the momentum space is replaced by the energy space to describe the electronic subsystem. We obtain the system of coupled non-linear integro-differential equations

$$\left\{ \begin{array}{l}
\frac{df}{dt} \Big|_{\varepsilon, t} = \frac{\partial f}{\partial t} \Big|_{pi} + \frac{\partial f}{\partial t} \Big|_{e-e} + \frac{\partial f}{\partial t} \Big|_{imp} + \frac{\partial f}{\partial t} \Big|_{e-ph-ph} + \frac{\partial f}{\partial t} \Big|_{e-ion-ph} \\
f \Big|_{\varepsilon, t=0} = f_0 \Big|_{\varepsilon} \\
\frac{dg_{\beta}}{dt} \Big|_{q, t} = \frac{\partial g_{\beta}}{\partial t} \Big|_{ph-e-ph} \\
g_{\beta} \Big|_{q, t=0} = g_{\beta,0} \Big|_{q}
\end{array} \right. \quad (2.4)$$

The expression containing the *electron-phonon* collision integral, $\frac{\partial f}{\partial t} \Big|_{e-ph}$, as a special case for

the *electron-phonon-photon* collision integral, $\frac{\partial f}{\partial t} \Big|_{e-ph-ph}$, is used. Similarly, the *phonon-electron*

collision integral, $\frac{\partial g_{\beta}}{\partial t} \Big|_{ph-e}$, is included in the *phonon-electron-photon* collision integral,

$\frac{\partial g_{\beta}}{\partial t} \Big|_{ph-e-ph}$, as we explain below.

2.1.2 Applicability

We note that Fermi's Golden Rule [22,57,70] is used in the calculation of collision integrals [14,76,77,78], so that the first step is to identify the scattering potential. Then, the corresponding matrix elements are evaluated. Below we provide the details of matrix element calculations based on Bloch and Volkov-Bloch wave functions [17,19,41,73,74,68,70,71,79,80,81,82,83]. Additional explanation can be find in Appendix A.

§2.2 Photoionization process

The transition probability of an electrons from the valence band to the conduction band caused by the laser field was studied by Keldysh [41].

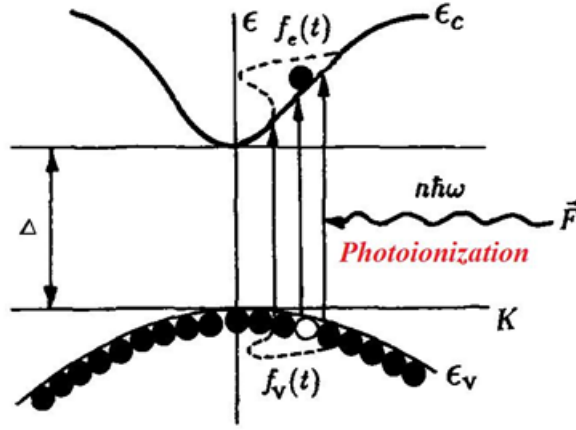


Fig. 2.2. Schematics of the photoionization in a two-band model. The laser field excites an electron from the valence (v) to the conduction band (c), creating a non-equilibrium electron distribution.

2.2.1 Fundamentals

The key issue in the Keldysh's approach is a choice of the electronic functions for the initial and final states. For this, Volkov-Bloch functions are taken as follows [80]

$$\psi_{\mathbf{p}t}^{c,v}(\mathbf{r}, t) = u_{\mathbf{p}t}^{c,v}(\mathbf{r}) \exp \left\{ \frac{i}{\hbar} \left[\mathbf{p}t \cdot \mathbf{r} - \int_0^t \mathcal{E}_{c,v}(\mathbf{p}, \tau) d\tau \right] \right\}, \quad (2.5)$$

with a time-dependent quasi-momentum vector modified by the external field

$$\mathbf{p}t = \mathbf{p} - \frac{e\mathbf{E}_b}{\Omega} \sin \Omega t, \quad (2.6)$$

where the field depends on time as $\mathbf{E}t = \mathbf{E}_b \cos \Omega t$; c is the conduction band and v is the valence band, and $u_{\mathbf{p}t}^{c,v}(\mathbf{r})$ is a periodic Bloch function of the coordinates, with a period equal to the period of the crystal lattice.

Thus, the difference between *Keldysh* approach and the usual perturbation theory lies only in the fact that the probability calculation of transition is not to a stationary final state, but to the state (2.5) that already takes exact account of the main effect of the electric field — the acceleration of the electron. The matrix element (averaged over wave period) of the transition between the states (2.5) was taken into account only in the first order of perturbation theory and the corresponding expression follows as

$$L_{cv} \mathbf{p} = \frac{1}{2\pi} \int_C V_{cv} \mathbf{p} u \exp \left\{ \frac{i}{\hbar\Omega} \int_0^u \frac{\mathcal{E} \mathbf{p} v}{\sqrt{1-v^2}} dv \right\} du, \quad (2.7)$$

and the matrix element of the optical transition from the valence to the conduction band is determined in the following fashion

$$V_{cv} \mathbf{p} = i\hbar \int_{\Omega_0} u_{\mathbf{p}}^{c*} \mathbf{r} e\mathbf{E}_b \nabla_{\mathbf{p}} u_{\mathbf{p}}^v \mathbf{r} d^3\mathbf{r}, \quad (2.8)$$

where Ω_0 is the volume of elementary cell.

2.2.2 Photoionization rate

The PI rate can be presented as $W_{pi} = \sum_{n=l_{pi}}^{n_{max}} W_{pi,n}$. The term $n=l_{pi}$ corresponds to the process

occurring due to the transition of a valence band electron absorbing minimum necessary number of photons [to satisfy the energy law, $\varepsilon_v \mathbf{k} + n\hbar\Omega = \varepsilon_c \mathbf{k}$] to the conduction band. The terms with $n > l_{pi}$ correspond to the process where the valence band electron absorbs energy above the necessary one. However, the electron energy in final state is limited, because the process occurs in the first Brillouin zone. That is, the electron energy in final state cannot overcome the Brillouin band-edge energy, $\varepsilon_{pi,n_{max}} < \varepsilon_{BZ}$, which is a significant difference from the situation in gases, where the electrons can go to infinity and have energy significantly more a few eV. Thus, there is a limited number of additional absorbed photons, therefore n is limited by n_{max} , that is

$n \leq n_{max}$, where $n_{max} = \left\lceil \frac{2\varepsilon_{BZ} + \Delta}{\hbar\Omega} - l_{pi} \right\rceil$. If the photon energy, $\hbar\Omega$, is much smaller than the

Brillouin band-edge energy, ε_{BZ} , then n_{max} is a huge number, and we can approximate n_{max} by infinity as *Keldysh* proposed. However, in visible region the photon energy is about 1 eV, and ε_{BZ} is a few eV, therefore that is important to take into account the limitation of n .

The PI rate depends on band structure (BS). Therefore we compare two high-usage dispersion laws of band structure in semiconductors/dielectrics.

In case Kane BS corresponding PI rate per unit of volume is given by [41]

$$W_{pi,n} = s \frac{2\Omega}{9\pi} \left(\frac{m_r \Omega}{\hbar \gamma_2} \right)^{3/2} Q_n^K \gamma, x \times \exp \left(-\pi l_{pi} \frac{K \gamma_2 - E \gamma_2}{E \gamma_1} \right) \quad (2.9)$$

and the function $Q_n^K \gamma, x$, which varies slowly compared with an exponential function, is of the form

$$Q_n^K \gamma, x = \sqrt{\frac{\pi}{2K \gamma_1}} \times \exp \left[-\pi n - l_{pi} \frac{K \gamma_2 - E \gamma_2}{E \gamma_1} \right] \times \phi \left(\sqrt{\frac{\pi^2 (n-x)}{2K \gamma_1 E \gamma_1}} \right), \quad (2.10)$$

where $\gamma = \frac{\Omega \sqrt{m_r \Delta}}{e E_b}$ is the master parameter, $\gamma_1 = \frac{1}{\sqrt{1+\gamma^2}}$, $\gamma_2 = \frac{\gamma}{\sqrt{1+\gamma^2}}$, $\tilde{\Delta} = \frac{2\Delta}{\pi \gamma_2} E \gamma_1$ is the effective ionization potential, $x = \tilde{\Delta} / \hbar \Omega$, $l_{pi} = [x+1]$ (the symbol $[x]$ denoted the integer part of the number x); the functions K and E are the complete elliptical integrals of the first and second kind (Appendix A), ϕ is the Dowson's integral (Appendix A). In the *Keldysh's* equations there is a few misprints. I completely preformed calculations to eliminate defects (Appendix G). The same procedure was performed by *Gruzdev* [82].

In case of parabolic BS, the corresponding rate per unit of volume is given by [84]

$$W_{pi,n} = s \frac{\Omega}{8\pi} \left(\frac{m_r \Omega}{\hbar} \right)^{3/2} Q_n^P \gamma, x \times \exp \left\{ -2l_{pi} \left[\text{Arsh} \sqrt{2\gamma} - \Theta \right] - 2x \frac{2\Theta \gamma^2}{1+4\gamma^2} \right\} \quad (2.11)$$

and, as previously, the similar function $Q_n^P \gamma, x$ is of the form

$$Q_n^P \gamma, x = \sqrt{1/\Theta} \times \phi \sqrt{2\Theta (n-x)} \times \exp -2 n - l_{pi} \left[\text{Arsh} \sqrt{2\gamma} - \Theta \right],$$

where $\tilde{\Delta} = \Delta \left(1 + \frac{1}{4\gamma^2} \right)$ is the effective ionization potential, $\Theta = 1/\sqrt{1+1/2\gamma^2}$; Arsh is the arc-hyperbolic sine function (Appendix A). Upon some corrections of several misprints in Ref. *Gruzdev* [84]. The equations coincided accurately with the numeric multiplier (Appendix G).

2.2.3 Photoionization collision integral

The corresponding collision integral can be written as follows

$$\left. \frac{\partial f}{\partial t} \right|_{pi-rr} = \frac{2\pi}{\hbar} \sum_{\mathbf{k}'} \left[|M_{pi} \mathbf{k}, \mathbf{k}'|^2 f_{\nu} \mathbf{k}' (1 - f_{\mathbf{k}}) \delta(\varepsilon_{\nu} \mathbf{k}' + n\hbar\Omega - \varepsilon_{\mathbf{k}}) - |M_{rr} \mathbf{k}', \mathbf{k}|^2 f_{\mathbf{k}} (1 - f_{\nu} \mathbf{k}') \delta(\varepsilon_{\mathbf{k}} - \varepsilon_{\nu} \mathbf{k}' - \hbar\Omega') \right] \quad (2.12)$$

where $|M_{pi} \mathbf{k}, \mathbf{k}'| = |M_{pi} \mathbf{k}, \mathbf{k}| \delta_{\mathbf{k}, \mathbf{k}'}$ corresponds to the direct photo-ionization matrix element, and $|M_{rr} \mathbf{k}', \mathbf{k}| = |M_{rr} \mathbf{k}, \mathbf{k}| \delta_{\mathbf{k}', \mathbf{k}}$ corresponds to the radiative recombination matrix element.

Taking into account that $|M_{rr}|^2 \ll |M_{pi}|^2$ [22], and

$$|M_{pi} \mathbf{k}, \mathbf{k}|^2 = \sum_{n=l_{pi}}^{n_{max}} |M_{pi,n} \mathbf{k}, \mathbf{k}|^2, \quad (2.13)$$

the expression for the photo-ionization collision integrals is given by

$$\left. \frac{\partial f}{\partial t} \right|_{pi} = \frac{2\pi}{\hbar} \sum_{n=l_{pi}}^{n_{max}} |M_{pi,n} \mathbf{k}, \mathbf{k}|^2 f_v \mathbf{k} (1 - f \mathbf{k}) \delta(\varepsilon_v \mathbf{k} + n\hbar\Omega - \varepsilon_c \mathbf{k}). \quad (2.14)$$

By assuming that the electron occupation numbers in the conduction and valence bands are isotropic in momentum space, the final collision integral for photon-ionization can be written as follows

$$\left. \frac{\partial f}{\partial t} \right|_{pi} = \frac{2\pi}{\hbar} \sum_{n=l_{pi}}^{n_{max}} |M_{pi,n}|^2 f_v \varepsilon_v (1 - f \varepsilon) \delta(\varepsilon_v + n\hbar\Omega - \varepsilon), \quad \varepsilon = \varepsilon_c. \quad (2.15)$$

In the case of parabolic BS, the corresponding matrix element is given by (Appendix E)

$$|M_{pi,n}|^2 = \frac{\hbar}{2\pi} \frac{2\pi^2 \hbar^3 W_{pi,n}}{\sqrt{2m_{cb} m_r^2 \varepsilon_{pi,n}}} \delta_{\varepsilon, \varepsilon_{pi,n}}, \quad \text{where } \varepsilon_{pi,n} = \frac{m_r}{m_{cb}} (n\hbar\Omega - \Delta). \quad (2.16)$$

Using eq. (2.16), the eq. (2.15) can be written as follow

$$\left. \frac{\partial f}{\partial t} \right|_{pi} = \frac{2\pi}{\hbar} \sum_{n=l_{pi}}^{n_{max}} \frac{\pi \hbar^4 W_{pi,n}}{\sqrt{2m_{cb}^3 \varepsilon_{pi,n}}} f_v \varepsilon_v (1 - f \varepsilon) \delta(\varepsilon - \varepsilon_{pi,n}). \quad (2.17)$$

In the case of Kane BS, the corresponding matrix element is given by

$$|M_{pi,n}|^2 = \frac{\hbar}{2\pi} \frac{\pi^2 \hbar^3 W_{pi,n}}{\sqrt{m_r^3 \varepsilon_{pi,n}}} \delta_{\varepsilon, \varepsilon_{pi,n}}, \quad \text{where } \varepsilon_{pi,n} = \frac{1}{2} (n\hbar\Omega - \Delta). \quad (2.18)$$

Using eq. (2.18) the eq. (2.15) can be written as follows

$$\left. \frac{\partial f}{\partial t} \right|_{pi} = \frac{2\pi}{\hbar} \sum_{n=l_{pi}}^{n_{max}} \frac{\pi \hbar^4 W_{pi,n}}{4\sqrt{m_r^3 \varepsilon_{pi,n}}} f_v \varepsilon_v (1 - f \varepsilon) \delta(\varepsilon - \varepsilon_{pi,n}). \quad (2.19)$$

§2.3 Electron-electron scattering process

2.3.1 Fundamentals

The electron gas in an insulator can be regarded as a plasma with fixed positive charges. Therefore, two electrons at \mathbf{r} and \mathbf{r}' interact through the screened Coulomb interaction potential V_{e-e} [22,57,70,71]

$$V_{e-e} = \frac{e^2}{4\pi\epsilon_0|\mathbf{r}-\mathbf{r}'|} \exp -q_0|\mathbf{r}-\mathbf{r}'|, \quad (2.20)$$

where e is the elementary charge, ϵ_0 is the electric permittivity of vacuum constant. The parameter $q_0 = 1/\lambda_0$ is the screening parameter. In the first approximation, the Debye screening length can be used for the screening parameter/length [22,68,70]

$$q_0^2 = \frac{n_e e^2}{\epsilon_0 k_B T_e} = \frac{3n_e e^2}{2\epsilon_0 \langle \epsilon \rangle} \Rightarrow \lambda_0^2 = \frac{2\epsilon_0 \langle \epsilon \rangle}{3n_e e^2}, \quad (2.21)$$

where k_B is Boltzmann constant, n_e is the density of electrons in the conduction band. T_e is the electron temperature in the equilibrium. Because the electron distribution is non-equilibrium so that the temperature is not defined, it is better to use the original definition for this parameter as follows

$$q_0^2 = \frac{e^2 m_{cb}^{3/2}}{2\sqrt{2}\pi^2 \epsilon_0 \hbar^3} \int_0^\infty \frac{f \epsilon}{\epsilon} \sqrt{\epsilon} d\epsilon, \quad (2.22)$$

or use T_e as a fitting parameter.

The matrix element of an electron-electron collision per volume $V = N\Omega_0$ [22,57,70,71]

$$\begin{aligned} |M_{e-e} \mathbf{k}_2, \mathbf{k}; \mathbf{k}_1, \mathbf{k}_3|^2 &= \left| \langle c\mathbf{k}_2, c\mathbf{k} | V_{e-e} | c\mathbf{k}_1, c\mathbf{k}_3 \rangle \right|^2 = \\ &= \left(\frac{e^2}{\epsilon_0 N \Omega_0} \frac{1}{\mathbf{k}_1 - \mathbf{k}_2^2 + q_0^2} \right)^2 \delta_{\mathbf{k}_2 + \mathbf{k}, \mathbf{k}_1 + \mathbf{k}_3 + \mathbf{g}}, \end{aligned} \quad (2.23)$$

where \mathbf{k}_1 and \mathbf{k}_3 are the wave vectors of the two electrons before the collision; \mathbf{k}_2 and \mathbf{k} are the wave vectors after the collision, \mathbf{g} is a reciprocal lattice vector used for the Umklapp processes ($\mathbf{g} \neq 0$), which is neglected here. Here, only normal processes with $\mathbf{g} = 0$ are considered.

2.3.2 Electron-electron scattering rate

The electron-electron scattering rate is given by the following expression

$$V_{e-e}(\varepsilon, n_e) = \frac{1}{\hbar^4} \left(\frac{m_{cb}}{2\pi\hbar} \right)^3 \left(\frac{e^2}{\mathbf{d}_0} \right)^2 \frac{1}{k} \iint_{\varepsilon_1 + \varepsilon \geq \varepsilon_2} \left(\int_{D_{\kappa}^{e-e}} \frac{d\kappa}{\kappa^2 + q_0^2} \right) F_{e-e}(\varepsilon_1, \varepsilon_2) d\varepsilon_1 d\varepsilon_2, \quad (2.24)$$

with

$$F_{e-e}(\varepsilon_1, \varepsilon_2) = f(\varepsilon_1) [1 - f(\varepsilon_2)], \quad (2.25)$$

where $\varepsilon_3 = \varepsilon_1 + \varepsilon - \varepsilon_2$; $k = k(\varepsilon) = \sqrt{2m_{cb}\varepsilon/\hbar^2}$; $D_{\kappa}^{e-e} \in [|k_1 - k_3|, k_1 + k_3] \cap [|k_2 - k|, k + k_2]$ is the integration region.

2.3.3 Electron-electron collision integral

The first perturbation theory is applied for the calculation of the collision integral. In our model, the electron-electron collision integral (for normal processes with $\mathbf{g} = 0$) is expressed as follows

$$\left. \frac{\partial f}{\partial t} \right|_{e-e} = \frac{2\pi}{\hbar} \times \sum_{\mathbf{k}_1, \mathbf{k}_2, \mathbf{k}_3} |M_{e-e}(\mathbf{k}_1, \mathbf{k}; \mathbf{k}_2, \mathbf{k}_3)|^2 \Phi_{e-e}(\mathbf{k}_1, \mathbf{k}, \mathbf{k}_2, \mathbf{k}_3) \delta(\varepsilon(\mathbf{k}_3) + \varepsilon(\mathbf{k}_2) - \varepsilon(\mathbf{k}_1) - \varepsilon(\mathbf{k})) \quad (2.26)$$

with

$$\Phi_{e-e}(\mathbf{k}_1, \mathbf{k}, \mathbf{k}_2, \mathbf{k}_3) = f(\mathbf{k}_3) f(\mathbf{k}_2) [1 - f(\mathbf{k})] [1 - f(\mathbf{k}_1)] - [1 - f(\mathbf{k})] f(\mathbf{k}_1) [1 - f(\mathbf{k}_3)] [1 - f(\mathbf{k}_2)]. \quad (2.27)$$

In Eqs. (2.26-27) the calculations by \mathbf{k}_1 , \mathbf{k}_2 and \mathbf{k}_3 are required. Here, according to the procedure presented in Appendix H, only a two-dimensional integral is solved as follows

$$\left. \frac{\partial f}{\partial t} \right|_{e-e} = \frac{1}{\hbar^4} \left(\frac{m_{cb}}{2\pi\hbar} \right)^3 \left(\frac{e^2}{\mathbf{d}_0} \right)^2 \frac{1}{k} \iint_{\varepsilon_1 + \varepsilon \geq \varepsilon_2} \left(\int_{D_{\kappa}^{e-e}} \frac{d\kappa}{\kappa^2 + q_0^2} \right) \Phi_{e-e}(\varepsilon, \varepsilon_1, \varepsilon_2, \varepsilon_3) d\varepsilon_1 d\varepsilon_2 \quad (2.28)$$

with

$$\Phi_{e-e}(\varepsilon, \varepsilon_1, \varepsilon_2, \varepsilon_3) = f(\varepsilon_3) f(\varepsilon_2) [1 - f(\varepsilon)] [1 - f(\varepsilon_1)] - [1 - f(\varepsilon)] f(\varepsilon_1) [1 - f(\varepsilon_3)] [1 - f(\varepsilon_2)], \quad (2.29)$$

where $\varepsilon_3 = \varepsilon_1 + \varepsilon - \varepsilon_2$; $k(\varepsilon) = \sqrt{2m_{cb}\varepsilon/\hbar^2}$; $D_{\kappa}^{e-e} \in [|k_1 - k_3|, k_1 + k_3] \cap [|k_2 - k|, k + k_2]$ is the integration region.

§2.4 Impact ionization process

The impact ionization term describes collisions between two electrons, where one electron is initially in the conduction band and the second one is in the valence band. As a result of the collision, valence band electron passes to the conduction band (ionization). The conduction band electron transfers energy to the valence band electron and the valence band electron and should be energetic enough to overcome the ionization barrier.

2.4.1 Fundamentals

The impact ionization is reverse to the Auger recombination process [71,78]. This process is not considered in the collision integrals because the probability of Auger is much smaller than the probability of the impact ionization for dielectric materials [22,68]. The screened Coulomb potential V_{e-e} is used as the interaction potential (see Section 2.3). The effect of the band change of the collided electrons is taken into account in the matrix element of the electron-electron collision. This is done with the help of the overlap integral $I(\mathbf{k}_2, \mathbf{k}_3)$. Thus, the matrix element for impact ionization is given by a combination of the matrix element for screened electron-electron interaction and the probability for a band transition for Normal processes ($\mathbf{g} = 0$) and Umklapp processes ($\mathbf{g} \neq 0$) [14,71,76,77]

$$\begin{aligned} |M_{imp}(\mathbf{k}, \mathbf{k}_2; \mathbf{k}_1, \mathbf{k}_3)|^2 &= \left| \langle c\mathbf{k}, c\mathbf{k}_2 | V_{e-e} | c\mathbf{k}_1, v\mathbf{k}_3 \rangle \right|^2 = \\ &= \left(\frac{e^2}{\dot{\mathbf{d}}_0 N \Omega_0} \frac{I(\mathbf{k}_2, \mathbf{k}_3)}{|\mathbf{k}_2 - \mathbf{k}_3|^2 + q_0^2} \right)^2 \delta_{\mathbf{k}+\mathbf{k}_2, \mathbf{k}_1+\mathbf{k}_3+\mathbf{g}}, \end{aligned} \quad (2.30)$$

where the overlap integral is written as

$$|I(\mathbf{k}_2, \mathbf{k}_3)|^2 = \frac{\hbar^2}{2\tilde{\Delta}} \left(\frac{1}{m_0} + \frac{1}{m_{vb}} \right) |\mathbf{k}_2 - \mathbf{k}_3|^2. \quad (2.31)$$

It should be noted that the conduction electron has an additional energy due to the action of ponderomotive laser field. Therefore this effect was taken into account by replacing the energy gap Δ by the effective energy gap $\tilde{\Delta}$ [see eq. (2.8) and eq. (2.10)] in the overlap integral, eq. (2.31).

2.4.2 Impact ionization rate

The impact ionization rate in our model is given by the following expression

$$\begin{aligned}
 \nu_{imp}(\varepsilon, n_e, \tilde{\Delta}) &= \frac{1}{2\pi\hbar^3} \left(\frac{e^2}{\mathbf{\hat{d}}_0} \right)^2 \frac{\hbar^2}{2\tilde{\Delta}} \left(\frac{m_{vb}}{m_0} + 1 \right) \left(\frac{m_{cb}}{\hbar^2} \right)^2 \frac{1}{k} \times \\
 &\times \iint_{\varepsilon - \varepsilon_1 - \varepsilon_2 \geq \tilde{\Delta}} \left(\int_{K_{imp}} \frac{\kappa^2 d\kappa}{\kappa^2 + q_0^2} \right) F_{imp}(\varepsilon_1, \varepsilon_2) d\varepsilon_1 d\varepsilon_2
 \end{aligned} \tag{2.32}$$

with

$$F_{imp}(\varepsilon_1, \varepsilon_2) = f_v(\varepsilon_{3c}) [1 - f(\varepsilon_1)] [1 - f(\varepsilon_2)], \tag{2.33}$$

where $K_{imp} = |k_1 - k|, k_1 + k \cap |k_2 - k_3^c|, k_2 + k_3^c$ is the integration region.

2.4.3 Impact ionization collision integral

In our model, only so-called ‘‘normal’’ processes are considered (quasi-free electrons in two-band approximation). In this case, the impact ionization collision integral (for normal processes with $\mathbf{g} = 0$) is

$$\begin{aligned}
 \left. \frac{\partial f}{\partial t} \right|_{imp} &= \frac{2\pi}{\hbar} \times \\
 &\times \sum_{\mathbf{k}_1, \mathbf{k}_2, \mathbf{k}_3} \left| M_{imp}(\mathbf{k}_1, \mathbf{k}_3^a; \mathbf{k}, \mathbf{k}_2) \right|^2 \Phi_{imp}(\mathbf{k}_1, \mathbf{k}_3^a, \mathbf{k}, \mathbf{k}_2) \delta(\varepsilon(\mathbf{k}_1) + \varepsilon_v(\mathbf{k}_3^a) - \varepsilon(\mathbf{k}) - \varepsilon(\mathbf{k}_2)) + \\
 &+ \left| M_{imp}(\mathbf{k}_1, \mathbf{k}_3^a; \mathbf{k}_2, \mathbf{k}) \right|^2 \Phi_{imp}(\mathbf{k}_1, \mathbf{k}_3^a, \mathbf{k}_2, \mathbf{k}) \delta(\varepsilon(\mathbf{k}_1) + \varepsilon_v(\mathbf{k}_3^a) - \varepsilon(\mathbf{k}_2) - \varepsilon(\mathbf{k})) - \\
 &- \left| M_{imp}(\mathbf{k}, \mathbf{k}_3^c; \mathbf{k}_1, \mathbf{k}_2) \right|^2 \Phi_{imp}(\mathbf{k}, \mathbf{k}_3^c, \mathbf{k}_1, \mathbf{k}_2) \delta(\varepsilon(\mathbf{k}) + \varepsilon_v(\mathbf{k}_3^c) - \varepsilon(\mathbf{k}_1) - \varepsilon(\mathbf{k}_2))
 \end{aligned} \tag{2.34}$$

with

$$\begin{aligned}
 \Phi_{imp}(\mathbf{k}_1, \mathbf{k}_3^a, \mathbf{k}, \mathbf{k}_2) &= f(\mathbf{k}_1) f_v(\mathbf{k}_3^a) [1 - f(\mathbf{k})] [1 - f(\mathbf{k}_2)], \\
 \Phi_{imp}(\mathbf{k}_1, \mathbf{k}_3^a, \mathbf{k}_2, \mathbf{k}) &= f(\mathbf{k}_1) f_v(\mathbf{k}_3^a) [1 - f(\mathbf{k}_2)] [1 - f(\mathbf{k})], \\
 \Phi_{imp}(\mathbf{k}, \mathbf{k}_3^c, \mathbf{k}_1, \mathbf{k}_2) &= f(\mathbf{k}) f_v(\mathbf{k}_3^c) [1 - f(\mathbf{k}_1)] [1 - f(\mathbf{k}_2)].
 \end{aligned} \tag{2.35}$$

Similarly to the calculations of the electron-electron processes, the calculations by \mathbf{k}_1 , \mathbf{k}_2 and \mathbf{k}_3 in eq. (2.34) can be reduced to the two-dimensional integral

$$\begin{aligned} \frac{\partial f}{\partial t} \Big|_{imp} &= \frac{1}{2\pi\hbar^3} \left(\frac{e^2}{\mathbf{d}_0} \right)^2 \frac{\hbar^2}{2\tilde{\Delta}} \left(\frac{m_{vb}}{m_0} + 1 \right) \left(\frac{m_{cb}}{\hbar^2} \right)^2 \frac{1}{k} \times \\ &\times \left\{ \iint_{\varepsilon_1 - \varepsilon - \varepsilon_2 \geq \tilde{\Delta}} \left(\int_{K_a \cup K_b} \frac{\kappa^2 d\kappa}{\kappa^2 + q_0^2} \right) \left[f(\varepsilon_1) f_v(\varepsilon_{3a}) (1 - f(\varepsilon)) (1 - f(\varepsilon_2)) \right] d\varepsilon_1 d\varepsilon_2 - \right. \\ &\left. - \iint_{\varepsilon - \varepsilon_1 - \varepsilon_2 \geq \tilde{\Delta}} \left(\int_{K_c} \frac{\kappa^2 d\kappa}{\kappa^2 + q_0^2} \right) \left[f(\varepsilon) f_v(\varepsilon_{3c}) (1 - f(\varepsilon_1)) (1 - f(\varepsilon_2)) \right] d\varepsilon_1 d\varepsilon_2 \right\} \end{aligned} \quad (2.36)$$

where $k_i = k \left\langle \varepsilon_i \right\rangle = \sqrt{2m_{cb}\varepsilon_i/\hbar^2}$; $\varepsilon_{3a} = m_{vb}/m_{cb} \left\langle \varepsilon_1 - \varepsilon - \varepsilon_2 - \tilde{\Delta} \right\rangle$ and $\varepsilon_{3c} = m_{vb}/m_{cb} \left\langle -\varepsilon_1 - \varepsilon_2 - \tilde{\Delta} \right\rangle$ are the electron kinetic energies follow from energy conservation.

The integration regions of the impact ionization collision integral, eq. (2.36), are given by

$$\begin{aligned} K_a &= |k_1 - k|, k_1 + k \cap |k_2 - k_3^a|, k_2 + k_3^a ; \\ K_b &= |k_3^a - k|, k_3^a + k \cap |k_1 - k_2|, k_1 + k_2 ; \\ K_c &= |k_1 - k|, k_1 + k \cap |k_2 - k_3^c|, k_2 + k_3^c . \end{aligned} \quad (2.37)$$

§2.5 Electron-phonon scattering process (in present/absence of laser wave field)

Free electrons oscillate in the laser field and can absorb energy only when a collision with third body occurs in this oscillation. For instance, an oscillating electron collides with a phonon absorbing or emitting its momentum.

2.5.1 Fundamentals

Here we involve laser field directly in the collision integral. There are a few ways to obtain the corresponding expressions for the probability and for the matrix element [72,73,74]. In particular, in *Epshtein* [72], the kinetic equation for the electrons was first derived in a strong electromagnetic field. In addition, *Mel'nikov* [73] (brief discussion) and *Furuse et al.* [74] provided the corresponding values derived with the help of a systematic method suggested by *Keldysh* [41].

The electron-phonon interaction's type depends on the materials. Since the insulators are usually ionic (ionic-covalent) materials, the polar electron-phonon interaction is one of the dominant processes in the interaction of the electrons with the lattice. The interaction is due to the coupling between the electron and the dipole field associated with the Longitudinal Optical (LO) phonons of the crystal; the weaker field associated to the Transverse Optical (TO) phonons being of negligible importance.

The LO-phonons are coupled to the electrons. Fröhlich Hamiltonian [85,86,87] is used to describe the collision between free electrons and polar phonons. The corresponding matrix element follows as

$$\begin{aligned} \left| M_{\beta,\pm}^{e-ph LO}(\mathbf{k}_1, \mathbf{q}; \mathbf{k}) \right|^2 &= \left| \langle \mathbf{k}_1 | V_{\beta,\pm}^{e-ph LO}(\mathbf{q}) | \mathbf{k} \rangle \right|^2 = \\ &= \frac{e^2}{\partial_0} \frac{|G_{\beta}(\mathbf{k}; \mathbf{q}, \mathbf{k}_1)|^2}{2N\Omega_0} \frac{1}{q^2} \left(g_{\beta}(\mathbf{q}) + \frac{1}{2} \mp \frac{1}{2} \right) \delta_{\mathbf{k}, \mathbf{k}_1 \pm \mathbf{q} + \mathbf{g}} \end{aligned} \quad (2.38)$$

Previously it was shown that the non-polar electron-phonon interaction have to be considered too. The non-polar interaction is treated within the deformation potential approximation [86,87]. Electrons can interact with acoustic and optical phonons (in SiO₂, only the TO-phonons [88]). Therefore, the corresponding matrix elements are

$$\begin{aligned}
\left| M_{j,\pm}^{e-ph AC} \mathbf{k}_1, \mathbf{q}; \mathbf{k} \right|^2 &= \left| \left\langle \mathbf{k}_1 \left| V_{j,\pm}^{e-ph AC} \mathbf{q} \right| \mathbf{k} \right\rangle \right|^2 = \\
&= \frac{\hbar |S_j \mathbf{k}; \mathbf{q}, \mathbf{k}_1|^2}{2\tilde{M}N\omega_j AC \mathbf{q}} \left(g_j \mathbf{q} + \frac{1}{2} \mp \frac{1}{2} \right) \delta_{\mathbf{k}, \mathbf{k}_1 \pm \mathbf{q} + \mathbf{g}}, \quad (2.39)
\end{aligned}$$

$$\begin{aligned}
\left| M_{\pm}^{e-ph TO} \mathbf{k}_1, \mathbf{q}; \mathbf{k} \right|^2 &= \left| \left\langle \mathbf{k}_1 \left| V_{\pm}^{e-ph TO} \mathbf{q} \right| \mathbf{k} \right\rangle \right|^2 = \\
&= \frac{\hbar |\Xi_{TO} \mathbf{k}; \mathbf{q}, \mathbf{k}_1|^2}{2\tilde{M}N\omega_{TO} \mathbf{q}} \left(g_{TO} \mathbf{q} + \frac{1}{2} \mp \frac{1}{2} \right) \delta_{\mathbf{k}, \mathbf{k}_1 \pm \mathbf{q} + \mathbf{g}}. \quad (2.40)
\end{aligned}$$

Using a spherical-band model, the matrix elements, at which an electron of wave vector of magnitude k scatters with each phonon of type β [the average by polarization (index j) is taken into account for acoustic mode] is written as

$$\left| M_{\beta,\pm}^{e-ph} \mathbf{k}_1, \mathbf{q}; \mathbf{k} \right|^2 = \begin{cases} \frac{3\hbar |\bar{S} q|^2}{2\tilde{M}N\bar{\omega}_{AC} q} \left(g_{\beta} \mathbf{q} + \frac{1}{2} \mp \frac{1}{2} \right) \delta_{\mathbf{k}, \mathbf{k}_1 \pm \mathbf{q} + \mathbf{g}}, \beta = 0 \\ \frac{e^2 |G_{\beta}|^2}{\delta_0 N\Omega_0 q^2} \left(g_{\beta} \mathbf{q} + \frac{1}{2} \mp \frac{1}{2} \right) \delta_{\mathbf{k}, \mathbf{k}_1 \pm \mathbf{q} + \mathbf{g}}, \beta = 1, 2, \\ \frac{\hbar |\Xi_{TO}|^2}{2\tilde{M}N\omega_{TO}} \left(g_{\beta} \mathbf{q} + \frac{1}{2} \mp \frac{1}{2} \right) \delta_{\mathbf{k}, \mathbf{k}_1 \pm \mathbf{q} + \mathbf{g}}, \beta = 3 \end{cases}, \quad (2.41)$$

where $\bar{S} q$, G_{β} and Ξ_{TO} are acoustical and optical coupling constants, respectively.

$\bar{S} q = iC_{AC}q$, where C_{AC} is the acoustic deformation potential; $|G_{\beta}|^2 = \frac{\hbar\omega_{\beta}}{2} \left(\frac{1}{\varepsilon_{>}^{\beta}} - \frac{1}{\varepsilon_{<}^{\beta}} \right)$, $\varepsilon_{>}^{\beta}$ and $\varepsilon_{<}^{\beta}$ are the high frequency (optical) dielectric constant and low frequency (static) dielectric constant of β -th LO-mode, respectively; Ξ_{TO} is the optical deformation potential; acoustic frequency, $\bar{\omega}_{AC} q$, is given by

$$\bar{\omega}_{AC} q = \begin{cases} v_s q, 0 < q \leq q_{BZ} \\ v_s q_{BZ}, q \geq q_{BZ} \end{cases},$$

q_{BZ} is the Brillouin band-edge wave vector; v_s is the mean speed of sound, $\frac{3}{v_s} = \frac{2}{v_s^{LA}} + \frac{1}{v_s^{TA}}$;

$k = k \varepsilon = \sqrt{2m_{cb}\varepsilon/\hbar^2}$; ρ is density of target in $[\text{kg}\cdot\text{m}^{-3}]$; $\omega_{\beta} q = \omega_{\beta}$, if $\beta \neq 0$ (see Appendix F).

According to *Epshtein* [72], the corresponding *e-ph-ph* matrix element is expressed as

$$\left| M_{l,\beta,\pm}^{e-ph-ph}(\mathbf{k}_1, \mathbf{q}; \mathbf{k}) \right|^2 = J_l^2(\mathbf{A}\mathbf{q}) \times \left| M_{\beta,\pm}^{e-ph}(\mathbf{k}_1, \mathbf{q}; \mathbf{k}) \right|^2, \quad (2.42)$$

where $\mathbf{A} = \frac{e\mathbf{E}_b}{m_{cb}\Omega^2}$, J_l is the Bessel function of integer order, $l = 0, \pm 1, \pm 2, \dots$ (Appendix A).

The index l stands for the number of photons being absorbed ($l > 0$) or emitted ($l < 0$) in one collision process. A multiplier $J_l^2(\mathbf{A}\mathbf{q})$ is responsible for the probability of such a collision. The term with $l=0$ provides the part of the pure *electron-phonon* interactions, that is without absorption/emission, however, with account of laser field. When the laser field is absent, $J_0^2(\mathbf{E}_b) = 0 = 1$ and $J_{l \neq 0}^2(\mathbf{E}_b) = 0 = 0$, then the matrix element, eq. (2.42), reduces to the usual *electron-phonon* matrix element, eq. (2.41).

2.5.2 Electron-phonon-photon scattering rate

In our model, the electron-phonon-photon scattering rate is given by following expression

$$\nu_{l,\beta,\pm}^{e-ph-ph}(\varepsilon, A, T) = \frac{1}{2\pi\hbar^3} \frac{m_{cb}}{k} \int_{D_{l,\beta,\pm}^{e-ph-ph}} \langle J_l^2(\mathbf{A}\mathbf{q}) \rangle |K_\beta(\mathbf{q})|^2 \left(g_\beta(\mathbf{q}) + \frac{1}{2} \mp \frac{1}{2} \right) q dq \quad (2.43)$$

with

$$|K_\beta(\mathbf{q})|^2 = \begin{cases} \frac{3\hbar |\bar{S}(\mathbf{q})|^2}{2\rho\bar{\omega}_{AC} q}, \beta = 0 \\ \frac{e^2 |G_\beta|^2}{\dot{\theta}_0 q^2}, \beta = 1, 2 \\ \frac{\hbar |\Xi_{TO}|^2}{2\rho\omega_{TO}}, \beta = 3 \end{cases}, \quad (2.44)$$

where $\langle J_l^2(\mathbf{A}\mathbf{q}) \rangle = \int_0^1 J_l^2(Aq\mu) d\mu$ is the average over polarization and the integration region

$D_{l,\beta,\pm}^{e-ph-ph}$ is given by

$$\begin{cases} \varepsilon k \geq -l\hbar\Omega \pm \hbar\omega_\beta q \\ \left[\frac{1}{2kq} \left[q^2 - \frac{2m_{cb}}{\hbar^2} l\hbar\Omega \pm \hbar\omega_\beta q \right] \right] < 1 \end{cases}. \quad (2.45)$$

The corresponding expression of the pure electron-phonon interactions follows as

$$\nu_{\beta,\pm}^{e-ph} \varepsilon, T = \frac{1}{2\pi\hbar^3} \frac{m_{cb}}{k} \int_{D_{\beta,\pm}^{e-ph}} |K_{\beta} \mathbf{q}|^2 \left(g_{\beta} \mathbf{q} + \frac{1}{2} \mp \frac{1}{2} \right) q dq, \quad (2.46)$$

where the integration region $D_{\beta,\pm}^{e-ph}$ is given by

$$\left\{ \begin{array}{l} \varepsilon k \geq \mp \hbar \omega_{\beta} \mathbf{q} \\ \left| \frac{1}{2kq} \left(q^2 \mp \frac{2m_{cb}}{\hbar^2} \hbar \omega_{\beta} \mathbf{q} \right) \right| < 1 \end{array} \right. \quad (2.47)$$

2.5.3 Electron-phonon collision integral

In the developed model, the electron-phonon collision integral is

$$\begin{aligned} \left. \frac{\partial f}{\partial t} \right|_{e-ph-ph} &= \frac{2\pi}{\hbar} \sum_{\beta} \sum_l \sum_{\mathbf{q}} J_l^2 \mathbf{Aq} |K_{\beta} \mathbf{q}|^2 \times \\ &\times \left[f_{\mathbf{k}+\mathbf{q}} g_{\beta} \mathbf{q} + 1 - f_{\mathbf{k}} g_{\beta} \mathbf{q} \right] \delta \varepsilon_{\mathbf{k}+\mathbf{q}} - \varepsilon_{\mathbf{k}} - \hbar \omega_{\beta} \mathbf{q} - l\hbar\Omega + \\ &+ \left[f_{\mathbf{k}-\mathbf{q}} g_{\beta} \mathbf{q} - f_{\mathbf{k}} g_{\beta} \mathbf{q} + 1 \right] \delta \varepsilon_{\mathbf{k}-\mathbf{q}} - \varepsilon_{\mathbf{k}} + \hbar \omega_{\beta} \mathbf{q} - l\hbar\Omega \end{aligned} \quad (2.48)$$

For homogenous and isotropic crystal, and, since we do not consider a definite polarization of laser light, averaging over all directions of the electric laser field by defining

$\langle J_l^2 \mathbf{Aq} \rangle = \int_0^1 J_l^2 Aq \mu d\mu$, the three-dimensional collision integral which represents light absorption by free electrons can be reduced to one-dimension, given by the following expression [14,76]

$$\begin{aligned} \left. \frac{\partial f}{\partial t} \right|_{e-ph-ph} &= \frac{1}{2\pi\hbar^3} \frac{m_{cb}}{k} \times \\ &\times \sum_{\beta} \sum_l \left\{ \int_{D_{l,\beta,+}^{e-ph-ph}} \langle J_l^2 \mathbf{Aq} \rangle |K_{\beta} \mathbf{q}|^2 \Phi_{\beta,+}^{e-ph} \varepsilon, q q dq + \right. \\ &\left. + \int_{D_{l,\beta,-}^{e-ph-ph}} \langle J_l^2 \mathbf{Aq} \rangle |K_{\beta} \mathbf{q}|^2 \Phi_{\beta,-}^{e-ph} \varepsilon, q q dq \right\} \end{aligned} \quad (2.49)$$

with

$$\Phi_{\beta,\pm}^{e-ph} \varepsilon, q = f_{\varepsilon_{\pm}} - f_{\varepsilon} \left(g_{\beta} \mathbf{q} + \frac{1}{2} \pm \frac{1}{2} \right) - f_{\varepsilon} - f_{\varepsilon_{\pm}} \left(g_{\beta} \mathbf{q} + \frac{1}{2} \mp \frac{1}{2} \right), \quad (2.50)$$

where $\varepsilon_{\pm} = \varepsilon \pm \hbar\omega_{\beta} \mp l\hbar\Omega$.

The integration regions $D_{l,\beta,\pm}^{e-ph-ph}$ of the electron-phonon-photon collision integral, eq. (2.49), is given by

$$\left\{ \begin{array}{l} \varepsilon \geq -l\hbar\Omega \pm \hbar\omega_{\beta} - q \\ \left| \frac{1}{2kq} \left[\frac{2m_{cb}}{\hbar^2} l\hbar\Omega \pm \hbar\omega_{\beta} - q - q^2 \right] \right| \leq 1 \end{array} \right. , \quad (2.51)$$

where $l = 0, \pm 1, \pm 2, \dots$; $\beta = 0, 1, 2, 3$; $k = k_{\varepsilon} = \sqrt{2m_{cb}\varepsilon/\hbar^2}$, $\varepsilon > 0$.

Note: $\hbar\Omega > \hbar\omega_{\beta} - q$, $\forall \beta$.

Phonons do not absorb laser energy. They are, however, indirectly affected by laser irradiation through their interaction with photon-absorbing electrons. Accounting for this fact, an analogous equation is obtained for the phonon-electron interactions

$$\left. \frac{\partial g_{\beta}}{\partial t} \right|_{ph-e-ph} = \frac{2\pi}{\hbar} \sum_l \sum_{\mathbf{k}} J_l^2 \mathbf{A}\mathbf{q} |K_{\beta}(\mathbf{q})|^2 \times \quad (2.52)$$

$$\times \Phi_{\beta}^{ph-e}(\mathbf{k}, \mathbf{q}) \delta(\varepsilon_{\mathbf{k}+\mathbf{q}} - \varepsilon_{\mathbf{k}} - \hbar\omega_{\beta} - q - l\hbar\Omega)$$

with

$$\Phi_{\beta}^{ph-e}(\mathbf{k}, \mathbf{q}) = f_{\mathbf{k}+\mathbf{q}} (1 - f_{\mathbf{k}}) g_{\beta}(\mathbf{q}) + (1 - f_{\mathbf{k}}) (1 - f_{\mathbf{k}+\mathbf{q}}) g_{\beta}(\mathbf{q}) . \quad (2.53)$$

As previously, the three-dimensional *phonon-electron* collision integral can be presented as one-dimensional one as follows

$$\left. \frac{\partial g_{\beta}}{\partial t} \right|_{ph-e-ph} = \frac{1}{2\pi\hbar^5} \frac{m_{cb}^2}{q} |K_{\beta}(q)|^2 \sum_l \langle J_l^2 \mathbf{A}\mathbf{q} \rangle \int_{D_{l,\beta}^e} \Phi_{\beta}^{ph-e}(\varepsilon, q) d\varepsilon \quad (2.54)$$

with

$$\Phi_{\beta}^{ph-e}(\varepsilon, q) = f_{\varepsilon_+} (1 - f_{\varepsilon}) g_{\beta}(q) + (1 - f_{\varepsilon}) (1 - f_{\varepsilon_+}) g_{\beta}(q) , \quad (2.55)$$

where $\varepsilon_{\pm} = \varepsilon + l\hbar\Omega + \hbar\omega_{\beta} \mp q$, and the integration region, $D_{l,\beta}^e$ of the *phonon-electron-photon* collision integral eq. (2.54) is given by

$$\left\{ \begin{array}{l} |q - k_{\varepsilon_+}| \leq k_{\varepsilon} \leq q + k_{\varepsilon_+} \\ \varepsilon \geq l\hbar\Omega + \hbar\omega_{\beta} - q \end{array} \right. . \quad (2.56)$$

The solution to the system eq. (2.56) is given by

$$\begin{cases} \varepsilon \geq l\hbar\Omega + \hbar\omega_\beta \\ \varepsilon \geq \frac{1}{4} \left[\frac{\hbar q}{\sqrt{2m_{cb}}} - \frac{\sqrt{2m_{cb}}}{\hbar q} (\hbar\Omega + \hbar\omega_\beta) \right]^2 \\ \varepsilon \geq -(\hbar\Omega + \hbar\omega_\beta) \end{cases} . \quad (2.57)$$

§2.6 Electron-ion scattering process (in presence/absence of laser field)

With increasing the density of free electrons, the number of the ionized atoms (ion centers) is raised too. The created free electrons can thus absorb laser energy due to collision with the ions in addition to other collisional processes.

2.6.1 Fundamentals

Having identified the perturbing potential for ionized impurity scattering (the screened Coulomb potential V_{e-e} in Section 2.3) and taking into account that momentum of ion centers is much larger than electron momentum, we evaluated the matrix element of an electron-ion collisions [22,77]

$$|M_{e-i}(\mathbf{k}'; \mathbf{k})|^2 = \left| \langle c\mathbf{k}' | V_{e-i} | c\mathbf{k} \rangle \right|^2 = \left(\frac{e^2}{\mathbf{d}_0 N \Omega_0} \frac{G}{\Delta k^2 + q_0^2} \right)^2, \quad (2.58)$$

where $\mathbf{k}' - \mathbf{k} = \Delta \mathbf{k}$, $G = 1$.

Similarly to *electron-phonon-photon* collision, the corresponding *e-ion-pht* matrix element can be expressed as

$$|M_l^{e-ion-pht}(\mathbf{k}'; \mathbf{k})|^2 = J_l^2 \mathbf{A} \Delta \mathbf{k} \times |M_{e-i}(\mathbf{k}'; \mathbf{k})|^2. \quad (2.59)$$

2.6.2 Electron-ion scattering rate

In our model, the corresponding rate of electron-ion-photon interactions is

$$v_l^{e-ion-pht}(\varepsilon, k, n_e, A) = \frac{1}{2\pi\hbar^3} \frac{m_{cb} n_i}{k} \int_{D_l^{\Delta k}} \langle J_l^2 \mathbf{A} \Delta \mathbf{k} \rangle |M_{e-i}(\Delta k)|^2 \Delta k d\Delta k, \quad (2.60)$$

where $n_i = \frac{N_i}{V} = n_e$ is the density of ions; $|M_{e-i}(\Delta k)|^2 = \left(\frac{e^2}{\mathbf{d}_0} \frac{1}{\Delta k^2 + q_0^2} \right)^2$ is the matrix element of transition, and the integration region is given by

$$D_l^{\Delta k} = \left\{ -1 < \frac{m_{cb}}{\hbar^2 k \Delta k} \left(l\hbar\Omega - \frac{\hbar^2 \Delta k^2}{2m_{cb}} \right) < 1 \right\}. \quad (2.61)$$

2.6.3 Electron-ion collision integral

The electron-ion collision integral is given in the form by

$$\left. \frac{\partial f}{\partial t} \right|_{e-ion-ph} = \frac{2\pi}{\hbar} \sum_l \sum_{\Delta \mathbf{k}} N_l J_l^2 A \Delta \mathbf{k} |M_{e-i}(\mathbf{k}, \mathbf{k}')|^2 \Phi_{e-i}(\mathbf{k}, \mathbf{k}') \delta(\varepsilon(\mathbf{k}') - \varepsilon(\mathbf{k}) - l\hbar\Omega) \quad (2.62)$$

with

$$\Phi_{e-i}(\mathbf{k}, \mathbf{k}') = f(\mathbf{k}') [1 - f(\mathbf{k})] - f(\mathbf{k}) [1 - f(\mathbf{k}')] \quad , \quad (2.63)$$

where $\mathbf{k}' = \mathbf{k} + \Delta \mathbf{k}$.

Using the assumption of a homogenous and isotropic crystal, and, because we do not consider laser polarization, an averaging over all directions of the electric laser field can be performed, so that the three-dimensional electron-ion collision integral can be presented as one-dimensional one as follows

$$\left. \frac{\partial f}{\partial t} \right|_{e-ion-ph} = \frac{1}{2\pi\hbar^4} \frac{m_{cb}^2 n_i}{\sqrt{2m_{cb}\varepsilon}} \sum_{l=-\infty}^{+\infty} \Phi_{e-i}(\varepsilon, \varepsilon'_0) \int_{D_l^{\varepsilon\Delta}} \langle J_l^2 A(\varepsilon, \varepsilon_\Delta) \rangle |M'_{e-i}(\varepsilon, \varepsilon_\Delta)|^2 d\varepsilon_\Delta \quad (2.64)$$

with

$$\Phi_{e-i}(\varepsilon, \varepsilon'_0) = f(\varepsilon'_0) [1 - f(\varepsilon)] - f(\varepsilon) [1 - f(\varepsilon'_0)] \quad , \quad (2.65)$$

where $\varepsilon'_0 = \varepsilon + l\hbar\Omega$, $\varepsilon_\Delta = \frac{\hbar^2 \Delta k^2}{2m_{cb}}$, and the integration region is given by

$$D_l^{\varepsilon\Delta} = \left\{ -1 \leq \frac{1}{2\sqrt{\varepsilon\varepsilon_\Delta}} (l\hbar\Omega - \varepsilon_\Delta) \leq 1, \varepsilon'_0 > 0 \right\}. \quad (2.66)$$

If $l=0$, then $\varepsilon'_0 = \varepsilon$ and $\Phi_{e-i}(\varepsilon, \varepsilon) \equiv 0$, that is pure electron-ion collisions do not contribute anything.

Chapter 3

Results and discussions

In this chapter, I have analyzed the mechanisms and physical processes involved in the ultra-short laser interactions with dielectric materials. The main objectives of this study are to demonstrate the role of laser parameters (laser pulse duration, wavelength, intensity) and material properties (band gap, effective mass, speed of sound, etc) in the process of laser damage. To check the validity of our model, it is also very important to compare our calculation results with both previous models and with experiments.

Here, the effects of model parameters on the final calculation results will be investigated. This study will provide a better inside in the considered physical processes as well as will allow fixing the correct parameters for the following comparison with experimental findings. Based on this study, we will be able to propose directly or indirectly material properties that can be measured in experiments. The attention is first focused on the electron kinetics. Therefore, first of all, we will consider parameters of the electronic subsystem and the influence of laser parameters (fluence, wavelength, pulse duration) on them. Then, the processes are analyzed, which are responsible for the changing of the number of conduction band electrons in our system. In particular, photo- and impact ionization processes are examined. The dependency of these processes on the corresponding parameters of laser pulse and material properties are investigated.

§3.1 Photoionization process

The primary free electrons appear in the system due to the photoionization process. First, we are interested by a value, which characterizes the intensity of this process, that is the photoionization rate in a unit volume. We perform an analysis of this value and its dependency on material and laser pulse parameters.

3.1.1 Role of laser field amplitude

First, all material parameters are fixed and photoionization rates is considered as a functions of laser field amplitude (that can be easily transferred to the peak intensity).

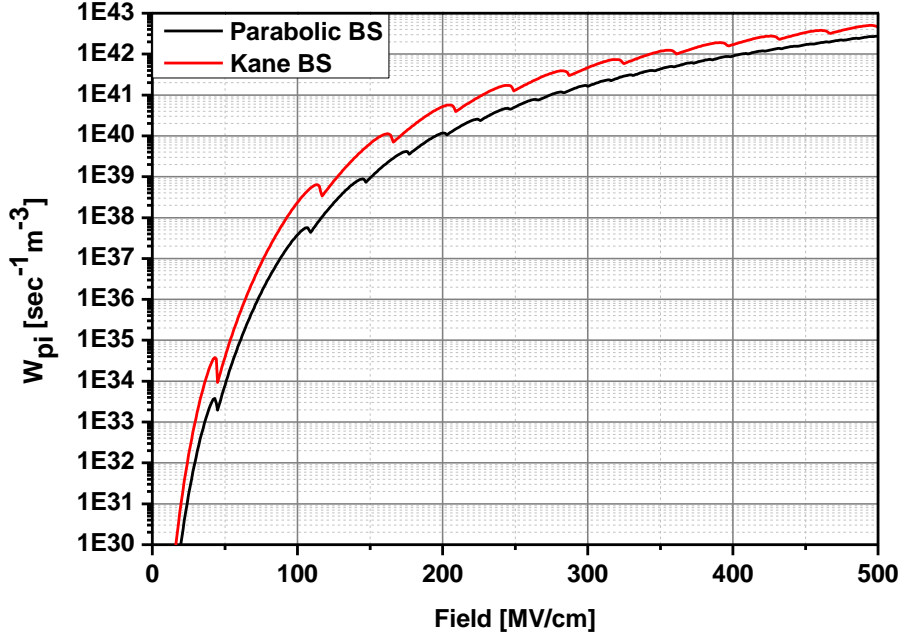


Fig. 3.1. Photoionization rate as a function of laser field amplitude for different dispersion laws of the band structure. Red curve is the Kane BS [see eq. (2.9)]; black curve is parabolic BS [see eq. (2.11)]. The results are obtained for the following parameters: reduced mass, $m_r = 0.5 m_0$; laser wavelength, $\lambda = 800$ nm; energy gap, $\Delta = 9$ eV.

Fig. 3.1 reveals that the behavior of the photoionization rate is similar for both BS laws. The rates grow with the increase in laser field amplitude. The oscillations in photoionization rate take place in both cases. They are caused by the deficit of energy, which means that with increasing laser field amplitude the electron energy in the field of laser wave increases and this process leads to the decrease in the probability of the photoionization process. When the energy conservation law cannot be satisfied [see eq. (2.12)], the minimum number of photons [see definition, eq. (2.10)] jumps up. Figure 3.1 clearly shows that in cases of Kane BS and parabolic BS the oscillations take place for different values of laser field. This difference is the main deviation in comparison of Kane BS and parabolic BS. One should mention that in *Keldysh* approach, the oscillation may not be observed because the electron-hole attraction was neglected. Therefore, for calculation it is better to apply the ranges of laser field where the photoionization rate behaves monotonically.

Now we choose one of the parameters of the electronic structure, the reduced mass to analyze the behavior of the photoionization rate. We fix all the parameters of the laser field, (wavelength, laser field amplitude, pulse width), as well as the energy gap, to present the reduced mass dependency on the photoionization rate.

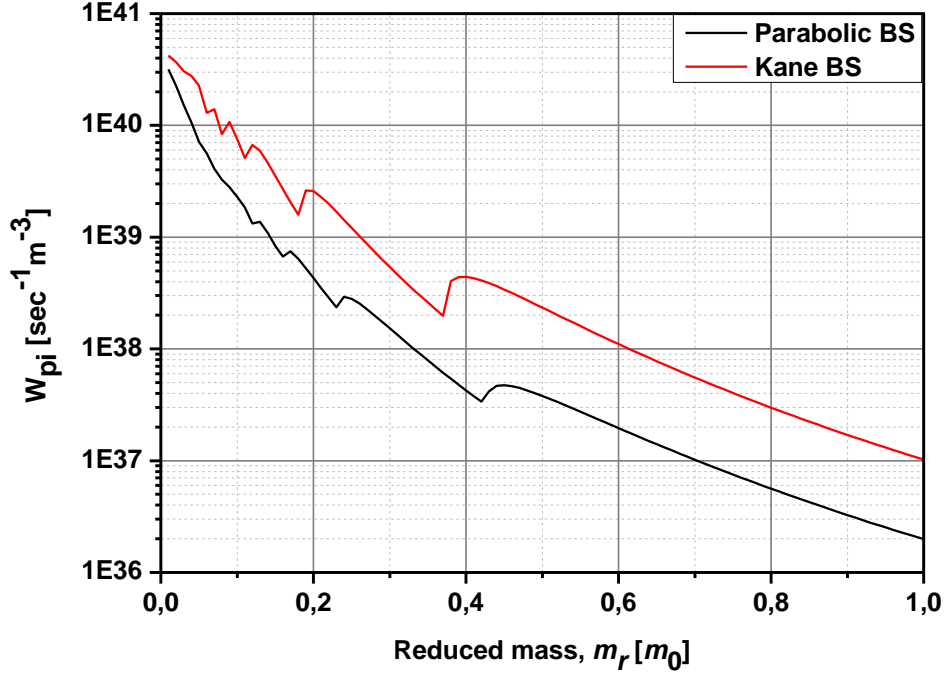


Fig. 3.2. Photoionization rate as a function of reduced mass for different dispersion laws of the band structure. Red curve is the Kane BS [see eq. (2.9)]; black curve is parabolic BS [see eq. (2.11)]. The results are obtained for the following parameters: laser field amplitude, $E_b = 100$ MV/cm; laser wavelength, $\lambda = 800$ nm; energy gap, $\Delta = 9$ eV.

Fig. 3.2 demonstrates that a variation in reduced mass leads to a significant change in the photoionization rate. As in the previous case (Fig. 3.1), the behavior of the photoionization rate is similar for both BS laws. For both dispersion laws we can see rate reduction with the increase in the value of the reduced mass. It is well known that more massive body is more inertial. By using this physical analogy it is easy to understand the reason of the observed dependency. The probability of photoionization process grows exponentially with the energy of the final state, that is $\propto \exp \tilde{\Delta}/\hbar\Omega$. With increasing reduced mass, the energy of the final state decreases [see Eqs. (2.10,11)], because lighter carriers in the laser field have larger energy than more massive ones at the same amplitude of the laser field. Thus the reduced mass is responsible for the “inertia” of the photoionization process.

3.1.2 Role of laser wavelength

To analyze laser wavelength dependency of the photoionization rate one should fix material parameters and vary laser wavelength.

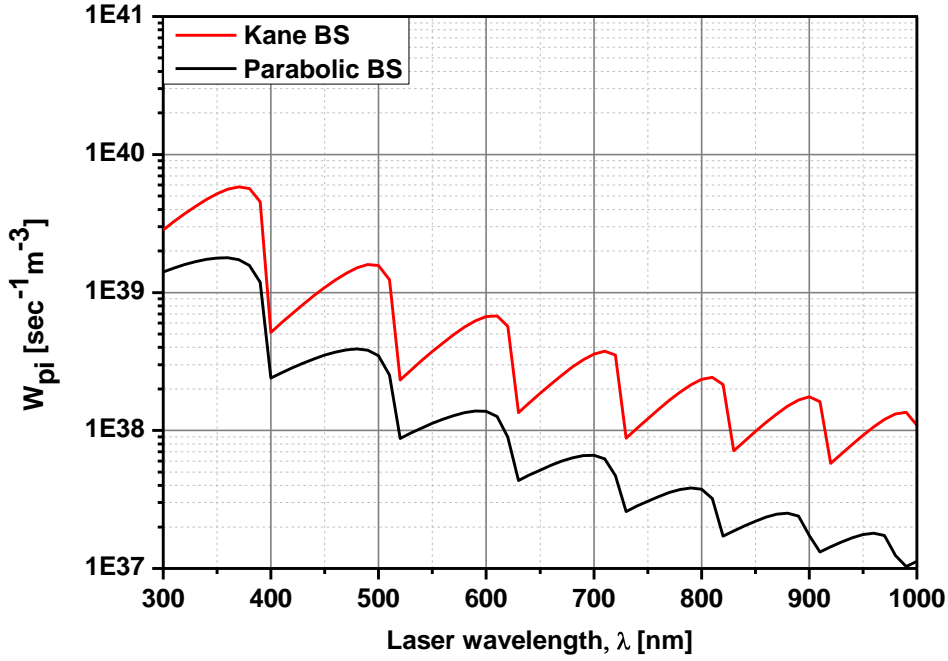


Fig. 3.3.1. Photoionization rate as a function of laser wavelength for different dispersion laws of the band structure. Red curve is the Kane BS [see eq. (2.9)]; black curve is parabolic BS [see eq. (2.11)]. The results are obtained for the following parameters: laser field amplitude, $E_b = 100$ MV/cm; reduced mass, $m_r = 0.5 m_0$; energy gap, $\Delta = 9$ eV.

Figure 3.3.1 shows that with increasing laser wavelength, the photoionization rate decreases for both dispersion laws. The decay in the rate takes place by, in fact, the same reason and has no monotone behavior due to the oscillation as in the previous case. Furthermore such behavior can be expected due to the following fact. As one well knows, longer wavelength corresponds to smaller photon energy. With decreasing photon energy the minimum number of photons [see Eqs. (2.10,11)] rises up. Therefore, to transfer an electron from the valence band to the conduction band one needs to absorb more photons in case of larger wavelength, whereas this effect decreases the probability of the photoionization process.

Note in the Figures 3.1, 3.2, 3.3.1 that the photoionization probability for Kane BS is higher than for parabolic BS case. This effect can be explained by the fact that the electron energy of the final state in the parabolic BS case is always larger than the energy in Kane BS case. Therefore, the absorbed energy and effective ionization potential are larger in parabolic case. However, greater ionization potential corresponds to a lower probability.

For better understanding of the role of laser wavelength in photoionization process, we perform a comparison of field-dependence of photoionization rate for two different values of laser wavelength. Here, Kane band structure model is chosen in calculations.

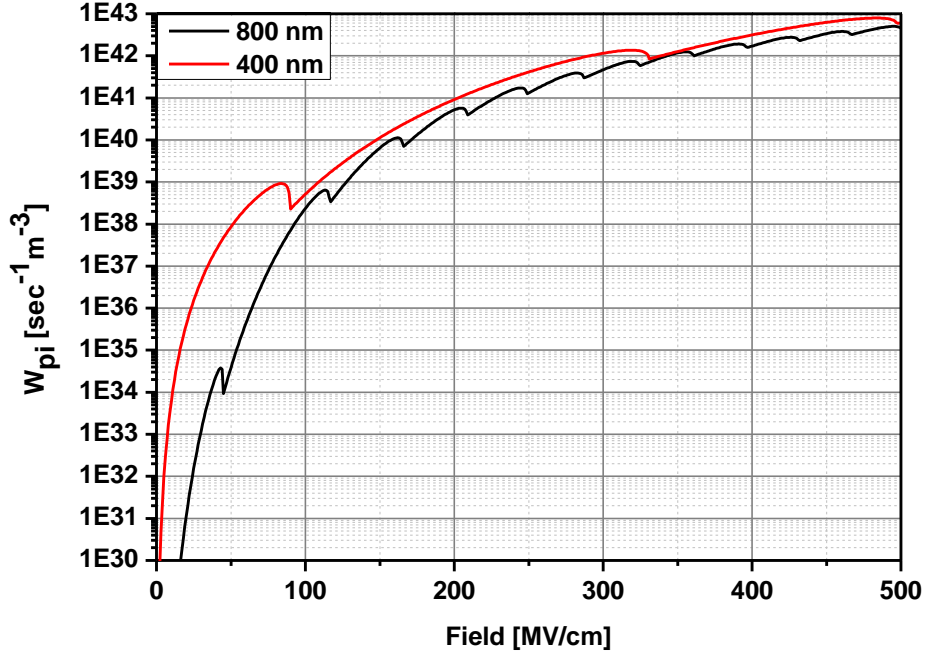


Fig. 3.3.2. Photoionization rate (Kane BS) [see eq. (2.9)] as a function of laser field amplitude for different values of laser wavelength. Red curve is $\lambda = 400$ nm; black curve is $\lambda = 800$ nm. The results are obtained for the following parameters: reduced mass, $m_r = 0.5 m_0$; energy gap, $\Delta = 9$ eV.

Figure 3.3.2 clearly shows that the oscillations of the photoionization rate are less regular for smaller laser wavelength. This fact can be explained by energy conservation law. That is, for smaller laser wavelength, in a wide range of laser field amplitude, the conservation law can be satisfied without changing the minimum number of photons, l_{pi} . In other words, the energy equivalent of one photon is enough for smaller values of laser wavelength to balance the energy of electron gained due to the ponderomotive force of laser field. This effect occurs in a wide range of laser field amplitudes because of the energy conservation law.

3.1.3 Structure of above-threshold ionization

Thus, the photoionization rate behaves non-monotonically, so that the oscillations take place. Now, we analyze the dependency of each n -th term of series of general equation for the photoionization rate, Eqs. (2.9-10), to demonstrate another aspects and the nature of oscillations. N -th term of the series corresponds to the transitional process of an electron from the valence band to the conduction band with the absorption of $l_{pi}+n$ photons of laser pulse, where l_{pi} is

minimum number of photons, which a bound electron has to absorb to be transferred to the conduction band.

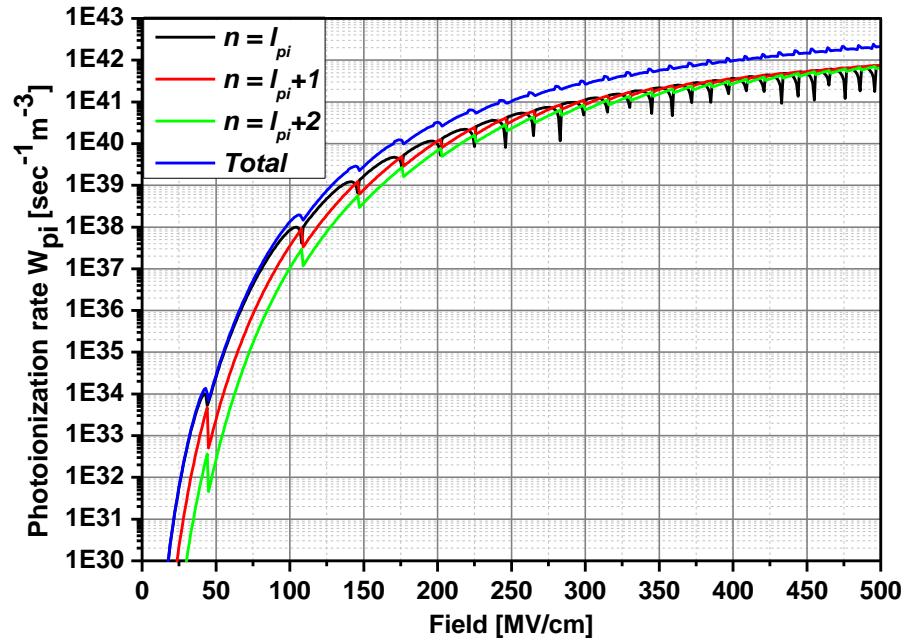


Fig. 3.4.1. N-th term of photoionization rate as a function of laser field amplitude for Kane band [see eq. (2.9)]structure model. The results are obtained for the following parameters: laser wavelength, $\lambda = 800$ nm; reduced mass, $m_r = 0.5 m_0$; energy gap, $\Delta = 9$ eV.

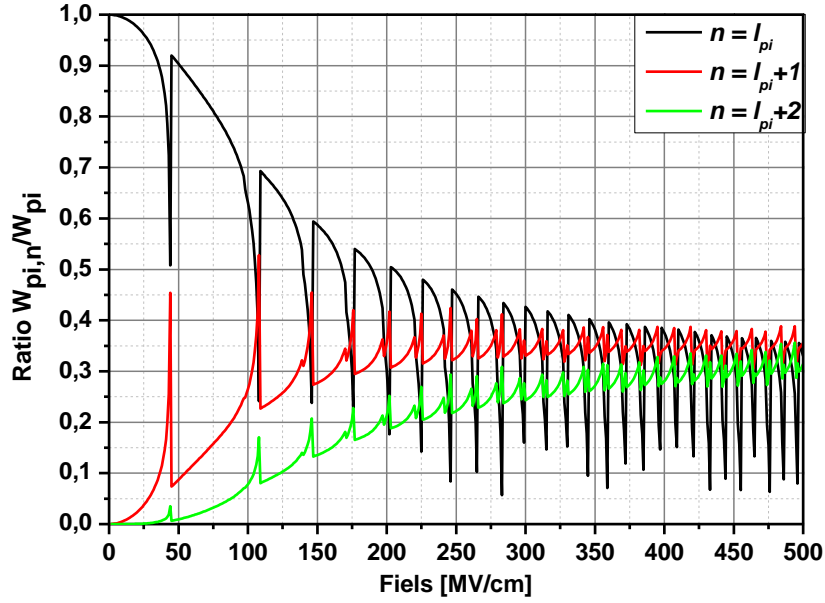


Fig. 3.4.2. Ratio of n -th term to total photoionization rate as a function of laser field amplitude for Kane BS [see eq. (2.9)]. The results are obtained for the following parameters: laser wavelength, $\lambda = 800$ nm; reduced mass, $m_r = 0.5 m_0$; energy gap, $\Delta = 9$ eV.

Figures 3.4.1-2 clearly demonstrate that the term, which corresponds to the process with $n = 0$ (that is the process where a bound electron absorbs minimum number of photons, l_{pi}) makes a major contribution to the total photoionization rate. Whereas the terms corresponding to processes with $n > 0$ begin to play a valuable role for larger laser fields. In addition, one can mention in the figures that when the term with $n = 0$ tend to decrease because of the energy conservation law that cannot be satisfied for certain l_{pi} , in contrast, the terms with $n > 0$ tend to growth. The growth of the terms with $n > 0$, however, does not balance the reduction of the main term, $n = 0$. Therefore, the behavior of total rate is non-monotonic and we can see oscillations. It should underline that this statement is true only in the scope of Keldysh approach, where the electron-hole attraction was neglected.

It should be noted that with the increase in laser field amplitude the oscillation amplitude decreases. This happens because the contributions for all the terms become comparable with each other (Fig. 3.4.2) in the tunnel regime at high laser field amplitude, $\gamma \ll 1$. Thus, when the main term tends to drop down, other terms compensate this reduction by their growth. As a result, oscillations become more negligible. Figure 3.1 clearly shows this fact in case of parabolic band structure model.

3.1.4 Extreme cases (regimes) of photoionization process

The *Keldysh* parameter, γ [see eq. (2.10)] determines either multi-photon ionization or tunneling takes place. It is important to study the photoionization regimes corresponding to

different ranges of this parameter. In previous chapter we briefly discussed the multiphoton and tunneling regimes. Previously, asymptotic expressions were used in the calculations, for simplicity. However, the application of these expression requires a more detail consideration. That is why, here we will present the calculated, photoionization rates based on the total expression [see Eqs. (G.7,9)] and compare the results with that obtained for two asymptotic cases, multiphoton [see eq. (G.12)] and tunnel [see eq. (40) [41]] regime, respectively.

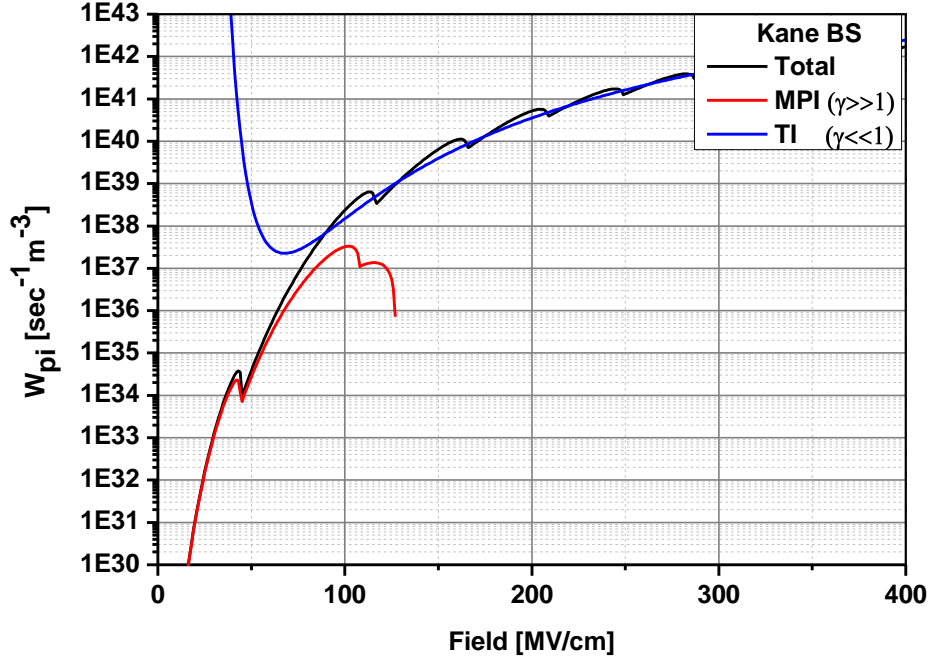


Fig. 3.5. Photoionization rate as a function of laser field amplitude for Kane band structure model. Red curve is asymptotic equation for multiphoton regime [eq. (G.12), App. G]; blue curve is asymptotic equation for tunnel regime [see eq.(40) [41]]; black curve is total photoionization rate. The results are obtained for the following parameters: laser wavelength, $\lambda = 800$ nm; reduced mass, $m_r = 0.5 m_0$; energy gap, $\Delta = 9$ eV.

Figure 3.5 reveals a difference between the two regimes. One can see that for the range of laser field corresponding to $\gamma \sim 1$, asymptotic expressions do not provide correct results. We will first discuss the applicability of the multiphoton regime. For this, we will present the ratio of asymptotic expression obtained for multiphoton regime to the total rate expression.

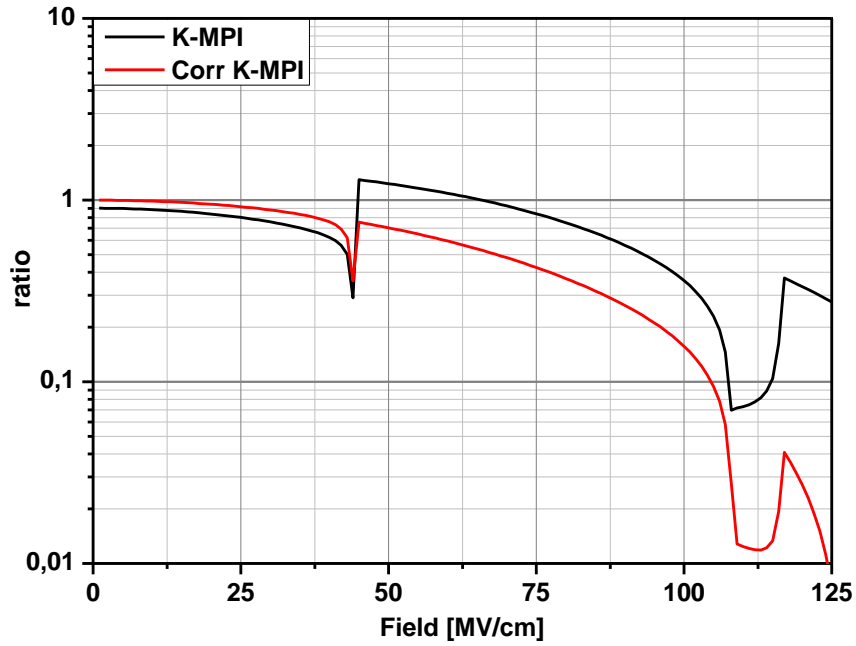


Fig. 3.6.1. Ratio of the asymptotic expression for the multiphoton regime to the total rate expression as a function of laser field amplitude for Kane BS model. Black curve is *Keldysh* asymptotic expression [eq. (G.11), App. G], red curve is correct *Keldysh* asymptotic expression [eq. (G.12), App. G]. The results are obtained for the following parameters: laser wavelength, $\lambda = 800$ nm; reduced mass, $m_r = 0.5 m_0$; energy gap, $\Delta = 9$ eV.

One can see in Figure 3.6.1 that the asymptotic expression corresponding to the original paper [41] and the correct asymptotic expression are different. For small laser field amplitude where $\gamma \gg 1$ black curve corresponded to the original paper starting from the value smaller than unity and the black curve overestimates photoionization rate in the range of the first oscillation. This result is due to the misprints in original paper (this fact also was mentioned by *Gruzdev* [82]). One can see in Figure 3.6.1 only a small range where asymptotic expression gives correct result namely between 0 and 60 MV/cm. The maximum deviation of the asymptotic expression from the total rate expression can be observed when the jump of minimum number of photons, l_{pi} occurs. Also this result is in agreement with the previously mentioned reasons. In particular, the asymptotic expression for the multiphoton regime corresponds to the contribution of zero-th term ($n = 0$), whereas in the vicinity of the jump other terms of series, with $n > 0$, begin to play an important role (Figures 3.4.1-2).

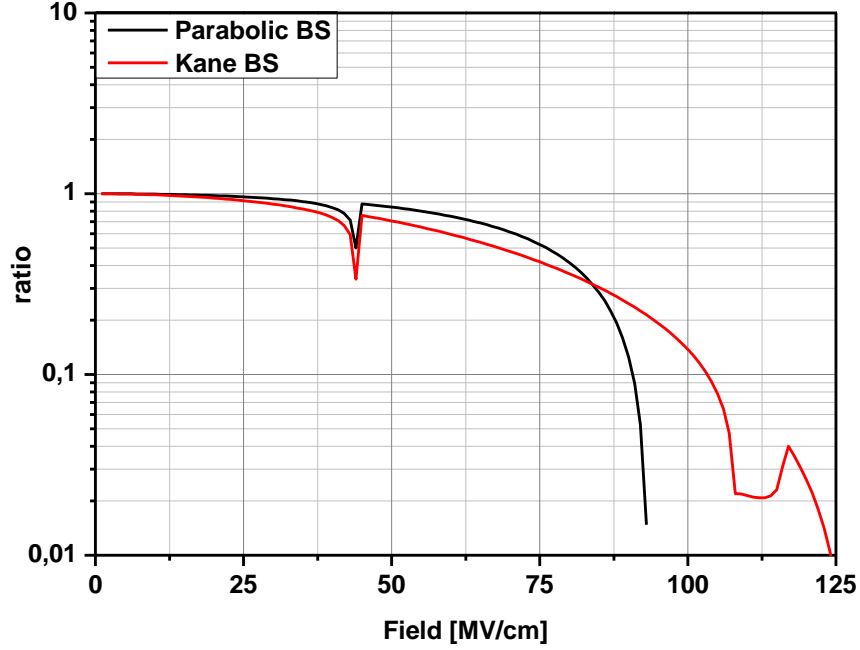


Fig. 3.6.2. Ratio of asymptotic expression for multiphoton regime to total rate expression as a function of laser field amplitude for different dispersion laws of the band structure. Red curve is the Kane BS model [correct expression, eq. (G.12), App. G]; black curve is parabolic BS model. The results are obtained for the following parameters: laser wavelength, $\lambda = 800$ nm; reduced mass, $m_r = 0.5 m_0$; energy gap, $\Delta = 9$ eV.

From the performed analysis of the figure 3.6.2, we note that the ratio is similar for different dispersion laws of band structure. Because the effect of ponderomotive force is negligible at small laser field amplitude, one cannot see any inherent difference. This result means that the energy conservation law is satisfied for the same value of the electron momentum. With increasing laser field amplitude, the shape of the band structure begins to play a more important role. The effect of a ponderomotive force is considerable at high laser field. As a result, the values of mean electron-hole energy will differ strongly at higher laser field amplitude for different dispersion law of band structure. In addition, the applicability of photoionization rate for both dispersion laws has similar range of laser field. This result is confirmed by the agreement between the applicability ranges of the mathematical expansions of special functions, which were applied to derive asymptotic expressions. It should be noted that using asymptotic expression outside of the range of applicability leads to significant deviation from total rate expression for both dispersion laws of band structure.

In the original paper [41], it was assumed that the energy of a single photon energy is much less than the depth of the conduction band, i.e., $\varepsilon_{BZ}/\hbar\Omega \ll 1 \Rightarrow n_{\max} \ll 1$. Therefore, the asymptotic expression for the tunneling regime was obtained by replacing the sum by an integral. However, the energy of the photon in the visible range ~ 1 eV, whereas the typical depth of the

conduction band < 5 eV, that is, $n_{\max} \sim 1$. Thus, we have no right to replace the sum by an integral, and use the asymptotic expression obtained by Keldysh for the tunneling regime in the visible range, because it can lead to incorrect results. Some authors use in the parameter $\gamma \sim 1$ cross-link the two asymptotic expressions, this should also be treated with caution. Moreover, in tunnel regime, the effective ionization potential is not described by the asymptotic for the multiphoton regime and should be applied following the correct expansion for this case: $\gamma \ll 1$,

$$\tilde{\Delta} \square \frac{2\Delta}{\pi\gamma} = \frac{2}{\pi} \frac{eE_b \sqrt{\Delta/m_r}}{\Omega} \text{ (Kane BS case).}$$

§3.2 Impact ionization process

The impact ionization process depends on many physical parameters, characterizing both the matter and the laser pulse, which are discussed below.

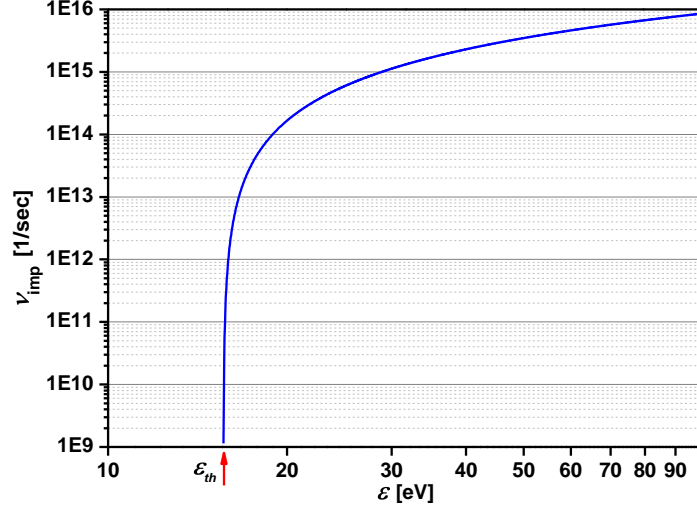


Fig. 3.7. The impact ionization rate [see eq. (2.32)] as a function of electron energy. The results are obtained for the following parameters: reduced mass, $m_r = 0.5 m_0$; energy gap, $\Delta = 9$ eV; electron density, $n_e = 2.5 \times 10^{27} \text{ m}^{-3}$.

Here, we demonstrate a general behavior of the impact ionization rate as a function of electron energy for the certain electron density in the absence of laser field. The figure clearly shows that impact ionization process take place only for the electrons with energy above the threshold energy, and rapidly grows with further energy increase. The threshold energy is determined by momentum and energy conservation laws, and given by follow expression

$$\varepsilon_{th} = \tilde{\Delta} \left(\frac{1 + 2\mu}{1 + \mu} \right), \text{ where } \mu = m_{cb}/m_{vb}: \text{ (i) } m_{cb} \ll m_{vb}, \varepsilon_{th} \approx \tilde{\Delta}; \text{ (ii) } m_{cb} = m_{vb}, \varepsilon_{th} = 1.5\tilde{\Delta}; \text{ (iii) } m_{vb} \ll m_{cb}, \varepsilon_{th} \approx 2\tilde{\Delta}.$$

3.2.1 Role of laser field amplitude and wavelength

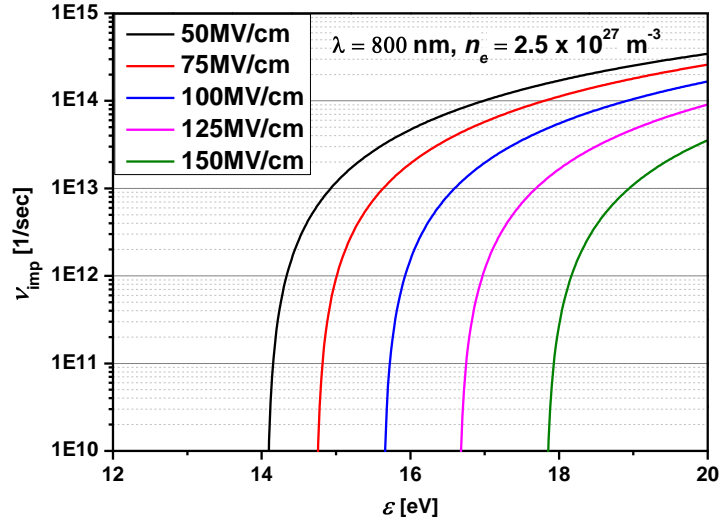


Fig. 3.8. Impact ionization scattering rate [see eq. (2.32)] as a function of electron energy for different values of laser field amplitude. The results are obtained for the following parameters: laser wavelength, $\lambda = 800$ nm; reduced mass, $m_r = 0.5 m_0$; energy gap, $\Delta = 9$ eV; electron density, $n_e = 2.5 \times 10^{27} \text{ m}^{-3}$.

Figure 3.8 shows that the probability of impact ionization decreases with increasing amplitude of the field, due to the fact that the probability is inversely proportional to the effective ionization potential, $\nu_{imp} \propto 1/\tilde{\Delta}$ [see Eq. (2.32)], while its value increases with the increase of the field amplitude. The threshold energy also increases, therefore moves to the region of higher energy. The increase of wavelength leads to the same situation in behavior of the rate due to the same reason: (i) $\gamma \gg 1$, $\tilde{\Delta} \approx \Delta + \frac{e^2 E_b^2}{4m_r \Omega^2}$; (ii) $\gamma \ll 1$, $\tilde{\Delta} \approx \frac{2}{\pi} \frac{e E_b \sqrt{\Delta/m_r}}{\Omega}$ (Kane BS).

We have considered the case where electrons have energy above the threshold. However, it is possible to decrease the threshold due to a participation of the photons in the process, that is photon-assisted impact-ionization process. This issue was analyzed by Strelakov [89], Mednis and Fain [90]. To estimate the contribution of impact-ionization with photon participation we calculated the ratio of the ionization probability with two-photon absorption to the probability without absorption (in this case, the expression is the simplest form) [89]. For the range of laser field 50-150 MV/cm and wavelength 800 nm, the calculation is $\frac{W_{if} \ n=0, l=1}{W_{if} \ n=0, l=0} = J_{l=1}^2 \left(\frac{e^2 E_b^2}{8m_r \hbar \Omega^3} \right) \approx 10^{-14} - 10^{-15}$. Thus, we obtained that the photon-assisted probability is significantly smaller than usual process, therefore it can be neglected.

Recently, the hypothesis of "cold avalanche" was proposed [91,92]. Dominating of the photon-assisted impact-ionization process above the photo-ionization process was concluded. However, in fact, the previous results were totally ignored, furthermore, the comparison with another theories was not discussed. Therefore, we just mentioned these results without accounting of the conclusion.

3.2.2 Screening and free electrons

During the laser pulse, the density of free electrons increases significantly with time, and this effect causes a change in the properties of electron interactions. First, with increasing in the electron density, the impact-ionization rate increases too, and $\nu_{imp} \propto \sqrt{n_e}$. However, the further increase in the electron density leads to the decay in the screening parameter, λ_0 [see definition, eq. (2.21)]. The smaller is this value, the smaller is the number of electrons that can interact with a given electron. As a result, this effect decreases the probability of the impact ionization process, and $\nu_{imp} \propto 1/n_e$. We demonstrate this effect below, in Figure 3.9.

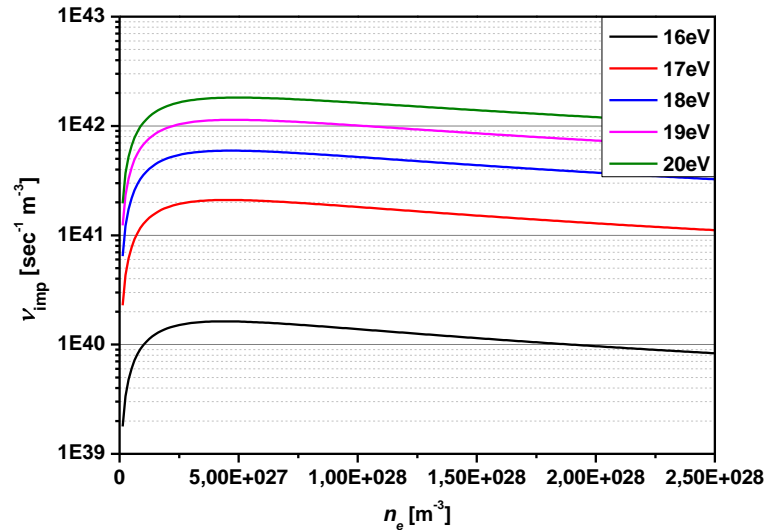


Fig. 3.9. Impact ionization scattering rate [see eq. (2.32)] per unit volume as a function of electron density for different values of mean electron energy. The results are obtained for the following parameters: laser wavelength, $\lambda = 800$ nm; laser field, $E_b = 100$ MV/cm; reduced mass, $m_r = 0.5 m_0$; energy gap, $\Delta = 9$ eV (SiO_2); SiO_2 elementary cell volume, $\Omega_0 \approx 100 \text{ \AA}^3$.

A comparison of the photo- and impact-ionization rates per unit volume (Figures 3.1 and 3.9, respectively) shows that probabilities are comparable, however, the impact-ionization occurs when the electrons have enough energy. Therefore, we discuss the electron heating process in the next section.

§3.3 Electron heating

The energy transfer from the laser pulse to the target takes place with the participation of the electronic subsystem. There is a number of channels to transfer laser energy. It was established that seed electrons appear through photoionization. As a result, electrons are injected in the conduction band with the energy of about 1 eV. A further increase in electron energy in the conduction band occurs due to the absorption of photons through collision with a third-body. These electron transitions are called intraband transitions. In fact, it is impossible to change electron energy without changing the momentum. Therefore, to absorb energy, electron should collide with a third-body. Thus, we evaluate the roles of various laser parameters and channels (electron-phonon/ion) in the electron heating.

3.3.1 Heating through the photoionization process

The energy conservation law, $\varepsilon_v + n\hbar\Omega = \varepsilon_c$, is justified due to the direct electron transition from the valence band to conduction band. Using the Kane BS and that $\varepsilon_v = -\varepsilon_c - \Delta$, the electron energy in conduction band is $\varepsilon_{pi,n} = \frac{1}{2} n\hbar\Omega - \Delta$, where $l_{pi} \leq n \leq n_{max}$. Previously we have established that the term corresponded $n = l_{pi}$ gives the major contribution. Then, the energy of photo-electron is $\varepsilon_{pi} = \frac{1}{2} l_{pi}\hbar\Omega - \Delta$. Let us analyze the spectrum of photo-electrons as a function of laser parameters.

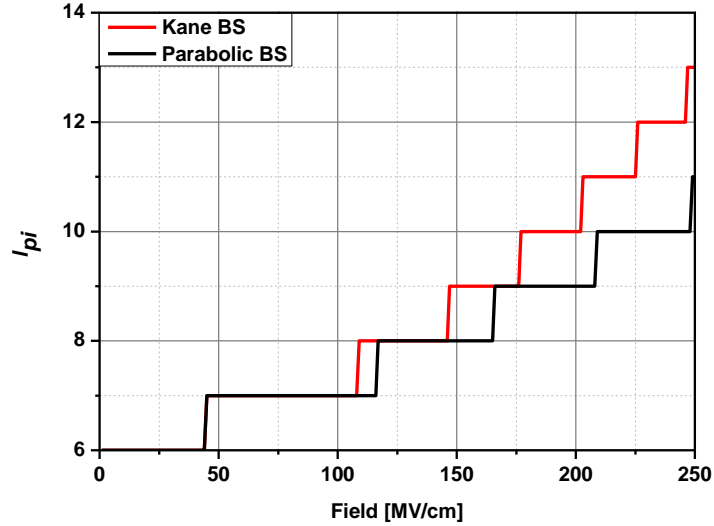


Fig. 3.10. l_{pi} (see section 2.1) as a function of laser field amplitude. Black curve is the Kane band structure model; red curve is parabolic band structure model. The results are obtained for the following parameters: laser wavelength, $\lambda = 800$ nm; reduced mass, $m_r = 0.5 m_0$; energy gap, $\Delta = 9$ eV.

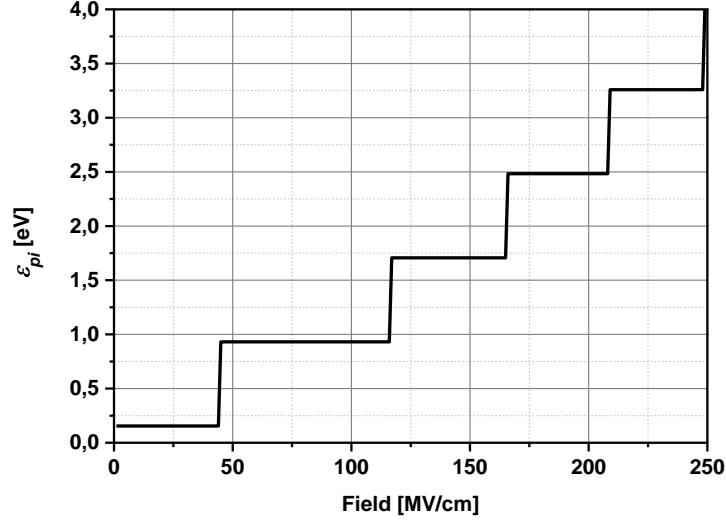


Fig. 3.11. ϵ_{pi} (see section 2.2) as a function of laser field amplitude for the Kane band structure model. The results are obtained for the following parameters: laser wavelength, $\lambda = 800$ nm; reduced mass, $m_r = 0.5 m_0$; energy gap, $\Delta = 9$ eV.

Figure 3.10 demonstrates the step-like behavior of l_{pi} , which results from the definition of l_{pi} . There is a difference between the curves because the BS affects ponderomotive effect of the laser field. However, this happens only for high field. In addition, these steps are too wide, so that the energy of photoelectron keeps the same value between the steps, and the energy changes only when l_{pi} changes (see Fig. 3.11). Thus, the spectrum of photoelectrons is delta-function and disposition of energy has stick-slip nature. In the same time the photoionization rate changes significantly with increasing of laser field.

Figure 3.11 clearly shows the range of photoelectron energy. In addition, the range of the required values of laser field is located within the scope of the Keldysh's equation applicability ($\epsilon_{pi} < \epsilon_{BZ}$). The energy of electrons is 0.5-1.0 eV for such fields. A comparison of the photoelectron energy with the energy required for the impact ionization, $\tilde{\Delta} < \epsilon_{th} < 2\tilde{\Delta}$, where $\tilde{\Delta} > \Delta$, yields that the energy of the photoelectrons is too small for impact ionization. In fact, this contribution of the ponderomotive effect of laser to the energy of photoelectrons was underestimated in previous paper [14,34,76,77].

3.3.2 Heating through electron-phonon/ion process

A series of calculations is performed for quartz with laser wavelengths 400 nm (see Figures 3.12-13, 15) and 800 nm (see Figure 3.14).

First, we consider laser energy absorption taking into account only the $e-ph-ph$ with *Normal*-processes. Figure 3.12 demonstrates the mean electron kinetic energy as a function of laser field amplitude for different laser pulse durations. One can see, that the value of mean energy in field-dependency is larger for longer laser pulses. For pulses up to 35 fs, a very weak dependency on the field can be observed. During such short times laser field cannot significantly influence the process of energy absorption by free electrons. The free electron absorption rate is smaller in collisions with phonons than the electron generation rate due to photoionization process. Therefore, many conduction band electrons can be created, but only a small part of them absorbs enough energy at short pulse durations. With the increase of pulse duration, a significant part of the generated electrons absorbs laser energy. This result leads to a much stronger dependency of the mean electron kinetic energy on the field amplitude. Particularly, for longer pulses with temporal width > 35 fs, the dependency on the field is stronger. Also, at each pulse duration a maximum of the dependency can be revealed. The presence of this maximum will be discussed below. In addition, it should be noted that for dielectric targets with approximately the same energy gap, the excess energy density will be higher for the material that has higher electron-phonon collisions rate.

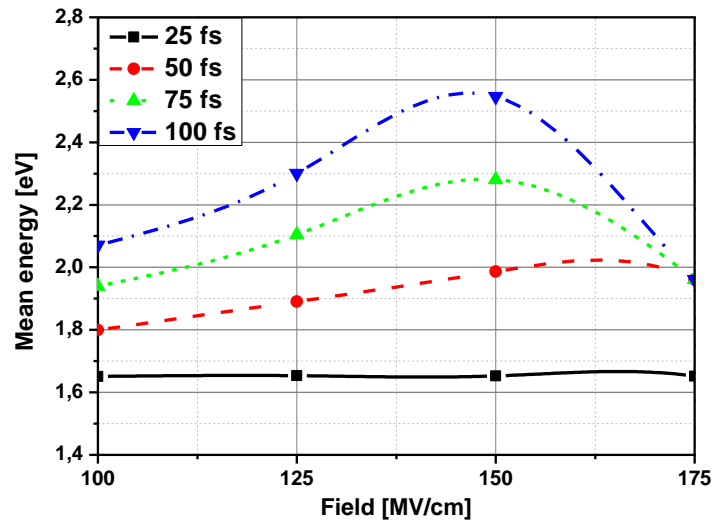


Fig. 3.12. Mean electron kinetic energy as a function of laser field amplitude for different laser pulse durations [$e-ph$ (*Normal*-processes)]. The calculation parameters are laser wavelength, $\lambda = 400$ nm, energy gap, $\Delta = 9$ eV (SiO_2).

Thus, we take into account the absorption through electron-phonon collisions (*N*-processes) in addition to the absorption due to photoionization process. Figure 3.12 clearly shows that the value of the mean energy is still too small to for the impact-ionization process. In laser energy absorption by conduction band electrons through the collisions with phonon, the *Umklapp* processes take place along with *normal* processes. Furthermore, with the increase in material ionization, the ion centers appear. Therefore, we involve these process in our calculations (section 2.6).

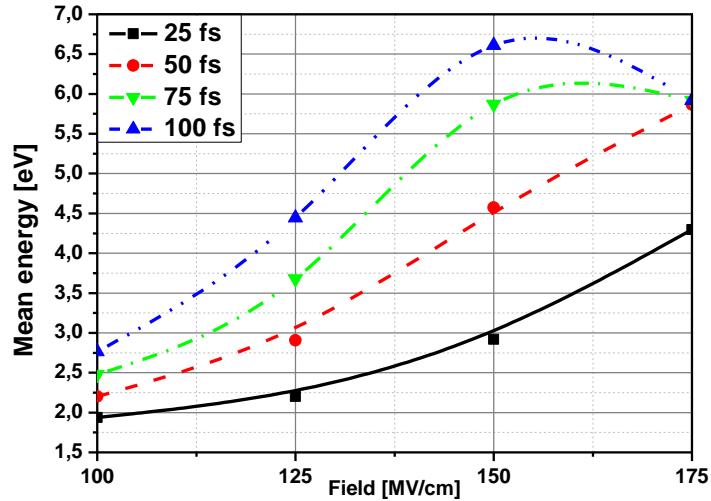


Fig. 3.13. Mean electron kinetic energy as a function of laser field amplitude for different laser pulse durations [e - ph ($Normal+Umklapp$) and e - ion processes]. The calculation parameters are laser wavelength, $\lambda = 400$ nm, energy gap, $\Delta = 9$ eV (SiO_2).

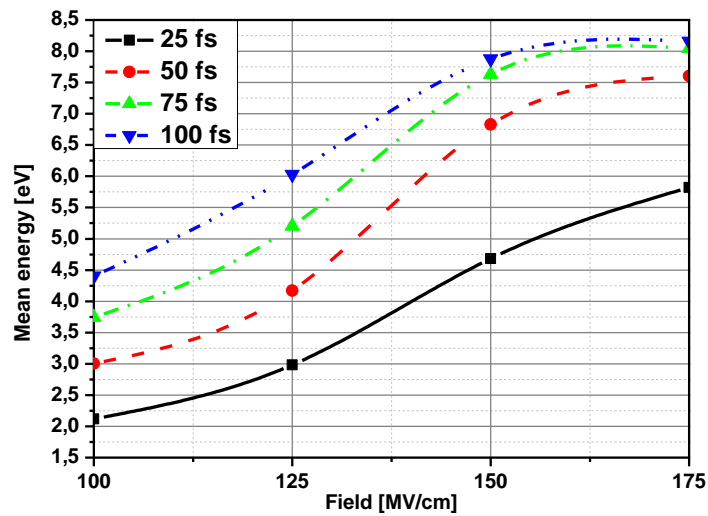


Fig. 3.14. Mean electron kinetic energy as a function of laser field amplitude for different laser pulse durations [e - ph ($Normal+Umklapp$) and e - ion processes]. The calculation parameters are laser wavelength, $\lambda = 800$ nm, energy gap, $\Delta = 9$ eV (SiO_2).

The calculations results obtained by including these processes are presented in Figures 3.13-14 (400 nm and 800 nm, respectively). These results indicate that electron-phonon *Umklapp*- and electron-ion processes contributions are ~15-25 % and ~90-110 %, respectively. Despite considerable contributions, the mean energy is still not high enough for the impact-ionization process. Consequently, this energy is insufficient to trigger the avalanche through the electron impact ionization, that confirms recent double pump-probe experimental

results by Guizard *et al.* [93]. The previous experimental results [40,49,94] are also in contradiction with the avalanche models that have been deduced from OBT (optical breakdown threshold) measurements as a function of the laser pulse duration [9,23,26,95].

Moreover, the long-wave (low energy) photons are more easily absorbed by conduction band electrons than short-wave (high energy) photons, as we observe from the comparison of results for the different wavelengths. This result can be explained by the fact that during the absorption of more energetic photon by free electron, the momentum change of the electron is larger than in the case of low-energy photon absorption, while the probability of the process is lower.

The field-dependent ratio of the absorbed to the incident energy is presented in Figure 3.15. We see that the amount of the absorbed energy grows faster with the field and slower with pulse duration. This effect is due to the fact that the energy lost to promote valence electrons to the conduction band is much larger than the energy absorbed by free electrons because the photoionization rate is higher than the absorption rate due to *e-ion-ph*t and *e-ph-ph*t collisions. Interestingly, the Figure 3.15 shows that the most efficient energy absorption takes place at pulse durations of 100 fs and field amplitude of 150 MV/cm (corresponding to pulse peak intensity $6.25 \times 10^{13} \text{ W/cm}^2$). At this laser pulse duration and field amplitude, the density of conduction electrons reaches the certain value [close to critical density, n_{cr} , and determined from the definition of the screening parameter in *electron-electron/ion* interaction potential, see Eqs. (2.21-22)], only at the end of the pulse, and, thus, the free electrons can absorb effectively laser energy during practically all the pulse. Further field increase leads to decay of the ratio, because the laser energy absorption by free electrons decreases due to laser field effect in *e-ion-ph*t [see eq. (2.59)] and *e-ph-ph*t [see eq. (2.43)] collisions (see Figure 3.24), and screening effect in *e-ion-ph*t collisions. One can see, the same behavior was demonstrated in the Figures 3.12-13.

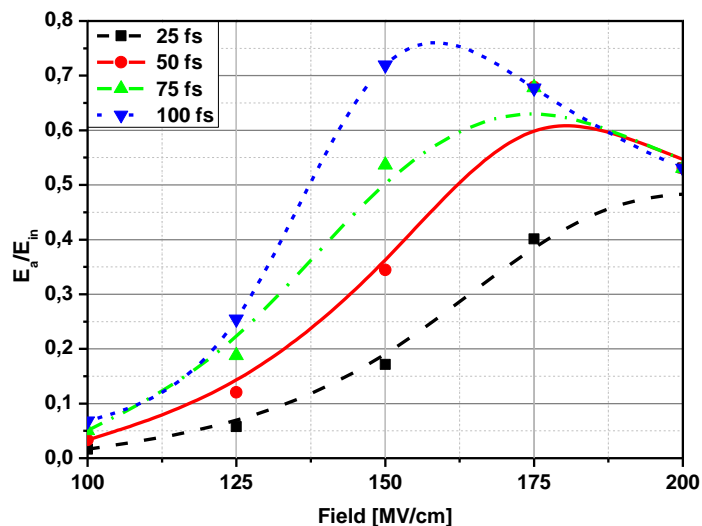


Fig. 3.15. Field-dependent ratio of the absorbed to the incident energy. The calculations are performed for laser wavelength; $\lambda = 400 \text{ nm}$; energy gap, $\Delta = 9 \text{ eV}$ (SiO_2).

§3.4 Heating process and optical properties: QM versus Classical (Drude)

When laser radiation passes through a medium, some part of it is always absorbed. This effect is described by a complex refractive index [96]

$$\hat{n} = \eta + i\kappa, \quad (3.1)$$

where $\eta = \Re \hat{n}$ is the real part, and $\kappa = \Im \hat{n}$ is the imaginary part of the refractive index, respectively.

The complex wave number $\tilde{k} = 2\pi\hat{n}/\lambda$ and complex refractive index \hat{n} can be substituted into the plane monochromatic wave expression as follows

$$\begin{aligned} \mathbf{E}_b(z, t) &= \Re[\mathbf{E}_b e^{i\tilde{k}z - \Omega t}] = \Re[\mathbf{E}_b e^{i2\pi\hat{n}z/\lambda - \Omega t}] = \\ &= \Re[\mathbf{E}_b e^{i2\pi(\eta + i\kappa)z/\lambda - \Omega t}] = e^{-2\pi\kappa z/\lambda} \Re[\mathbf{E}_b e^{i2\pi\eta z/\lambda - \Omega t}]. \end{aligned} \quad (3.2)$$

Here, we see that the exponential decay is proportional $\sim \kappa$, as expected from the Beer–Lambert law [97]. Because intensity is proportional to the square of the electric field, the absorption coefficient is

$$\alpha_{abs} = \frac{2\Omega}{c} \kappa, \quad (3.3)$$

and the Beer–Lambert law in the bulk is

$$\frac{dI_{bulk}}{dz} = -\alpha_{abs} I_{bulk} \quad (3.4)$$

with

$$I_{bulk} = c\epsilon_0 \eta \langle |\mathbf{E}_b(z, t)|^2 \rangle. \quad (3.5)$$

On the other side, the complex refractive index can be defined through the dielectric function as

$$\hat{n} = \sqrt{\hat{\epsilon}}, \quad (3.6)$$

and the dielectric function can be presented as follows

$$\hat{\epsilon} = \epsilon_r + i\epsilon_i, \quad (3.7)$$

where $\epsilon_r = \Re \hat{\epsilon}$ is the real part and $\epsilon_i = \Im \hat{\epsilon}$ is the imaginary part, respectively.

A conversion between the complex refractive index and the dielectric function is done by

$$2\eta^2 = \dot{\sigma}_r + \sqrt{\dot{\sigma}_r^2 + \dot{\sigma}_i^2} \Rightarrow \eta = \sqrt{\frac{\dot{\sigma}_r + \sqrt{\dot{\sigma}_r^2 + \dot{\sigma}_i^2}}{2}},$$

$$2\kappa^2 = -\dot{\sigma}_r + \sqrt{\dot{\sigma}_r^2 + \dot{\sigma}_i^2} \Rightarrow \kappa = \sqrt{\frac{-\dot{\sigma}_r + \sqrt{\dot{\sigma}_r^2 + \dot{\sigma}_i^2}}{2}}, \quad (3.8)$$

$$2\kappa\eta = \dot{\sigma}_i.$$

Reflectivity can be calculated from the refractive index and the incidence angle by using Fresnel equations, which for normal incidence are reduced to [98]

$$R = \frac{|\hat{n} - 1|^2}{|\hat{n} + 1|^2} \Rightarrow R = \frac{\eta - 1^2 + \kappa^2}{\eta + 1^2 + \kappa^2}. \quad (3.9)$$

In the case of normal incidence the relation between I_{vac} and I_{bulk} is $I_{bulk} = 1 - R I_{vac}$, where $I_{vac} = \sqrt{\dot{\sigma}_0/\mu_0} \langle |\mathbf{E}_0|^2 \rangle = c\dot{\sigma}_0 \langle |\mathbf{E}_0|^2 \rangle$. Then using eq. (3.5) we obtain the relation for the field amplitudes in the bulk and vacuum

$$\langle |\mathbf{E}_b|^2 \rangle = \frac{1 - R}{\eta} \langle |\mathbf{E}_0|^2 \rangle. \quad (3.10)$$

With the help of the Beer–Lambert law and using the relation, $\frac{dQ_e}{dt} = -\frac{dI_{bulk}}{dz}$, we obtain the rate of energy absorption per unit volume

$$\frac{dQ_e}{dt} = \alpha_{abs} I_{bulk}. \quad (3.11)$$

We assume a monochromatic wave, $\mathbf{E}_b = \mathbf{E}_b \cos \Omega t$, therefore the squared field amplitude averaged over wave period is $\langle |\mathbf{E}_b|^2 \rangle = \frac{E_b^2}{2}$. Then, from Eqs. (3.3), (3.5), (3.8), and (3.11), the absorbed energy rate per unit volume through the dielectric function is

$$\frac{dQ_e}{dt} = \frac{2\Omega\kappa}{c} \frac{c\dot{\sigma}_0\eta E_b^2}{2} = \frac{\dot{\sigma}_0\Omega E_b^2}{2} 2\kappa\eta \Rightarrow \frac{dQ_e}{dt} = \frac{\dot{\sigma}_0\Omega E_b^2}{2} \dot{\sigma}_i. \quad (3.12)$$

The spatial dispersion can be neglected due to the that fact characteristic parameter is too small, $k\lambda_0 \ll 1$ ("cold plasma" [99]), therefore the dielectric function only is as a function of frequency, that is, $\dot{\sigma}(\mathbf{k}) \rightarrow \dot{\sigma}(\Omega)$.

Previously, Drude model was often applied to describe the heating process and optical properties during the laser pulse. According to this model [99,100], the acceleration of electron is considered classically, and the electron velocity in alternating field is

$$\dot{\mathbf{r}}_t = \frac{e\mathbf{E}_b t}{m_{cb} v_{eff} + i\Omega}, \text{ here } \mathbf{E}_b t = \mathbf{E}_b e^{i\Omega t}, \quad (3.13)$$

where v_{eff} is the effective collision rate. According to the Matthiessen's rule [57], this rate is

$$\text{often set as an adjustable parameter, } v_{eff} = \frac{1}{\tau_{eff}} = \frac{1}{\tau_{e-ph}} + \frac{1}{\tau_{e-ion}} + \dots$$

Then the mean electron energy rate can be simply written as

$$\frac{d\langle \varepsilon \rangle}{dt} = \langle e\dot{\mathbf{r}}_t \cdot \mathbf{E}_b t \rangle = \frac{e^2 E_b^2 v_{eff}}{2m_{cb} (\Omega^2 + v_{eff}^2)}. \quad (3.14)$$

Thus, using eq. (3.14), and taking into account that energy density of free electrons is $Q_e = n_e \langle \varepsilon \rangle$, the absorbed energy rate per unit volume can be expressed as

$$\frac{dQ_{Dr}}{dt} = \frac{\dot{\partial}_0 \Omega E_b^2 n_e}{2 n_{cr} (\Omega^2 + v_{eff}^2)}, \text{ where } n_{cr} = \frac{\dot{\partial}_0 m_{cb} \Omega^2}{e^2}. \quad (3.15)$$

To obtain the expression for the imaginary part of the dielectric function we should substitute Eq. (3.15) in Eq. (3.12), then we calculate the real part using of the Kramers-Kronig relations [98]

$$\dot{\partial}_r(\Omega) - \dot{\partial}'_g = \frac{1}{\pi} v.p. \int_{-\infty}^{+\infty} \frac{\dot{\partial}_i(\Omega')}{\Omega' - \Omega} d\Omega'. \quad (3.16)$$

$$\dot{\partial}_i(\Omega) = -\frac{1}{\pi} v.p. \int_{-\infty}^{+\infty} \frac{\dot{\partial}_r(\Omega') - \dot{\partial}'_g}{\Omega' - \Omega} d\Omega'. \quad (3.17)$$

Here, $\dot{\partial}'_g = 1 + \dot{\partial}_g - 1 - n_e/n_v$ is the static dielectric constant of excited matter [33], and $v.p.$ denotes the Cauchy principal value.

As a result, the corresponding expressions are given by

$$\dot{\partial}_r^{Dr} = \dot{\partial}'_g - \frac{n_e}{n_{cr}} \frac{\Omega^2}{\Omega^2 + v_{eff}^2}, \quad (3.18)$$

$$\dot{\partial}_i^{Dr} = \frac{n_e}{n_{cr}} \frac{\Omega v_{eff}}{\Omega^2 + v_{eff}^2}. \quad (3.19)$$

By using Eqs. (3.18-19), we obtain the well-known expression for the Drude dielectric function

$$\dot{\sigma}_{Dr} = \dot{\sigma}'_g - \frac{n_e}{n_{cr}} \left(\frac{\Omega}{\Omega + i\nu_{eff}} \right). \quad (3.20)$$

We note that often electrons cannot be considered classically [see Eqs. (3.25-26)]. The Drude model, furthermore does not take into account the absorption due to photo-ionization. Therefore, we perform a comparison of the Drude model with the quantum mechanical approach as follows.

According to our model, the absorbed energy rate per unit volume is

$$\dot{Q}_e = \dot{Q}_{pi} + \dot{Q}_{e-ph-ph} + \dot{Q}_{e-ion-ph}, \text{ where, } \dot{Q} = \frac{dQ}{dt}, \quad (3.21)$$

where corresponding contributions are given by

$$\begin{aligned} \dot{Q}_{pi} &= n_e \times l_{pi} \hbar \Omega \times \nu_{pi}, \quad \nu_{pi} = W_{pi} / n_e, \\ \dot{Q}_{e-ion-ph} &= n_e \times \sum_l l \hbar \Omega \times \nu_l^{e-ion-ph}, \end{aligned} \quad (3.22)$$

$$\dot{Q}_{e-ph-ph} = n_e \times \sum_l l \hbar \Omega \times \nu_l^{e-ph-ph}, \quad \nu_l^{e-ph-ph} = \sum_{\beta, \pm} \nu_{l, \beta, \pm}^{e-ph-ph}.$$

By using Eqs. (3.12), (3.21-3.22), we obtain the imaginary part of the dielectric function

$$\dot{\sigma}_i^{QM} = \Delta \dot{\sigma}_i^{pi} + \Delta \dot{\sigma}_i^{e-ion-ph} + \Delta \dot{\sigma}_i^{e-ph-ph}, \quad (3.23)$$

where the corresponding contributions are given by the following expressions

$$\begin{aligned} \Delta \dot{\sigma}_i^{pi} &= \frac{2n_e}{\dot{\sigma}_0 \Omega E_b^2} l_{pi} \hbar \Omega \times \nu_{pi}(\Omega, E_b), \quad \nu_{pi}(\Omega, E_b) = W_{pi}(\Omega, E_b) / n_e, \\ \Delta \dot{\sigma}_i^{e-ion-ph} &= \frac{2n_e}{\dot{\sigma}_0 \Omega E_b^2} \sum_l l \hbar \Omega \times \nu_l^{e-ion-ph}(\Omega, E_b, \langle \varepsilon \rangle), \\ \Delta \dot{\sigma}_i^{e-ph-ph} &= \frac{2n_e}{\dot{\sigma}_0 \Omega E_b^2} \sum_l l \hbar \Omega \times \nu_l^{e-ph-ph}(\Omega, E_b, \langle \varepsilon \rangle, T). \end{aligned} \quad (3.24)$$

By using Kramers-Kronig relations and the definitions of the scattering rates [Eqs. (G.7,9), (2.60), (2.43)] we calculate the real and imaginary parts of dielectric function and corresponding optical properties according quantum mechanical approach. Then, these values are compared with the results of Drude model.

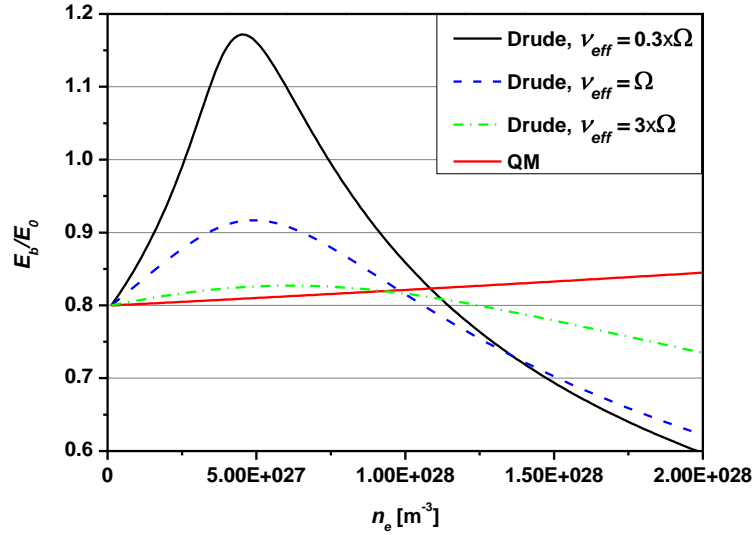


Fig. 3.16. Ratio of the laser field amplitude in the bulk to the laser field amplitude in the vacuum [eq. (3.10)] as a function of electron density. The calculation parameters are laser wavelength, $\lambda = 800$ nm; field amplitude, $E_0 = 180$ MV/cm; mean electron energy, $\langle \varepsilon \rangle = 5$ eV; energy gap, $\Delta = 9$ eV (SiO_2), and lattice temperature, $T = 300$ K.

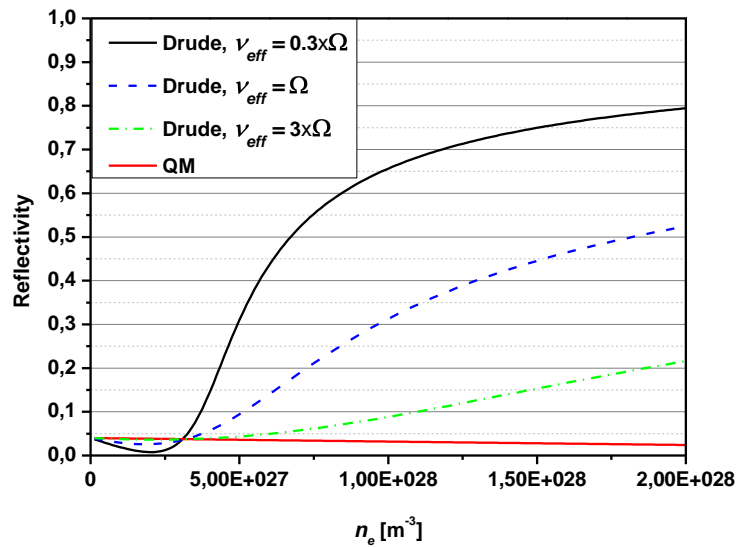


Fig. 3.17. Reflectivity [see eq. (3.9)] as a function of electron density. The calculation parameters are laser wavelength, $\lambda = 800$ nm; field amplitude, $E_0 = 180$ MV/cm; mean electron energy, $\langle \varepsilon \rangle = 5$ eV; energy gap, $\Delta = 9$ eV (SiO_2), and lattice temperature, $T = 300$ K.

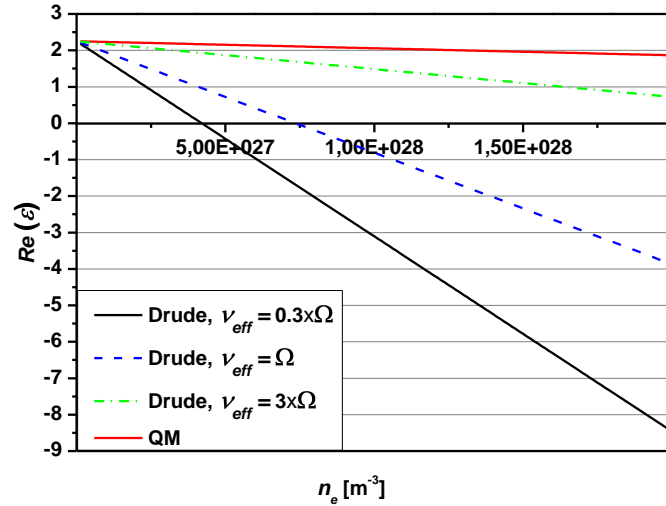


Fig. 3.18. The real part of the dielectric function as a function of electron density. The calculation parameters are laser wavelength, $\lambda = 800$ nm; field amplitude, $E_0 = 180$ MV/cm; mean electron energy, $\langle \varepsilon \rangle = 5$ eV; energy gap, $\Delta = 9$ eV (SiO_2), and lattice temperature, $T = 300$ K.

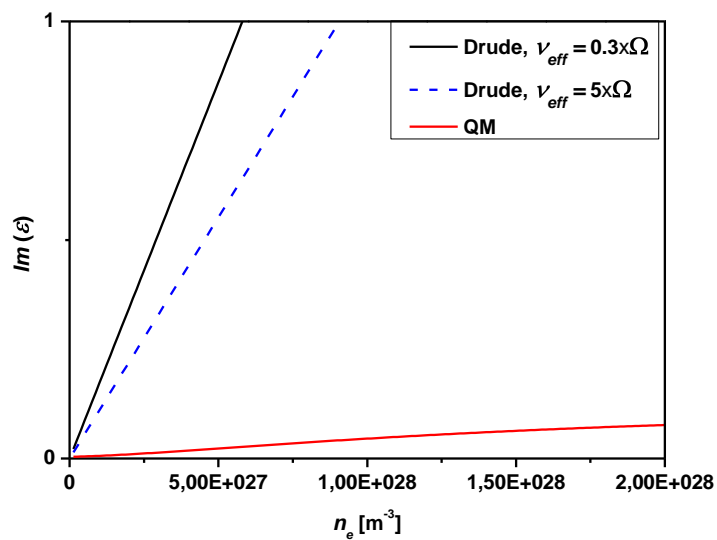


Fig. 3.19. The imaginary part of the dielectric function as a function of electron density. The calculation parameters are laser wavelength, $\lambda = 800$ nm; field amplitude, $E_0 = 180$ MV/cm; mean electron energy, $\langle \varepsilon \rangle = 5$ eV; energy gap, $\Delta = 9$ eV (SiO_2), and lattice temperature, $T = 300$ K.

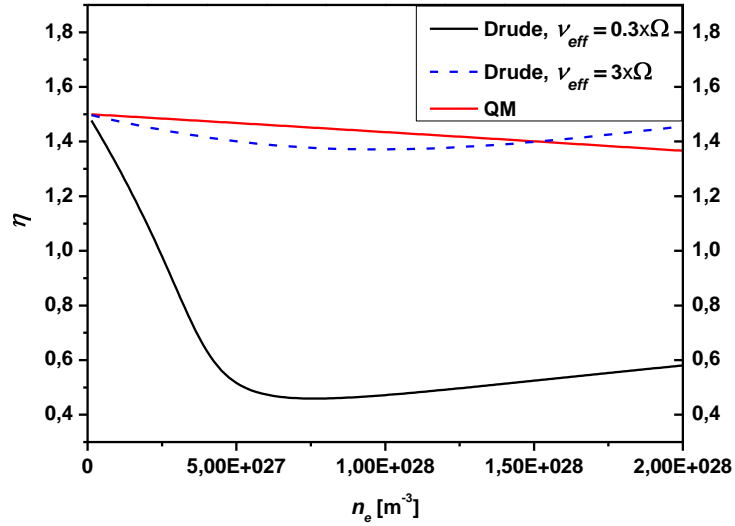


Fig. 3.20. The real part of the refractive index [see eq. (3.8)] as a function of electron density. The calculation parameters are laser wavelength, $\lambda = 800$ nm; field amplitude, $E_0 = 180$ MV/cm; mean electron energy, $\langle \varepsilon \rangle = 5$ eV; energy gap, $\Delta = 9$ eV (SiO_2), and lattice temperature, $T = 300$ K.

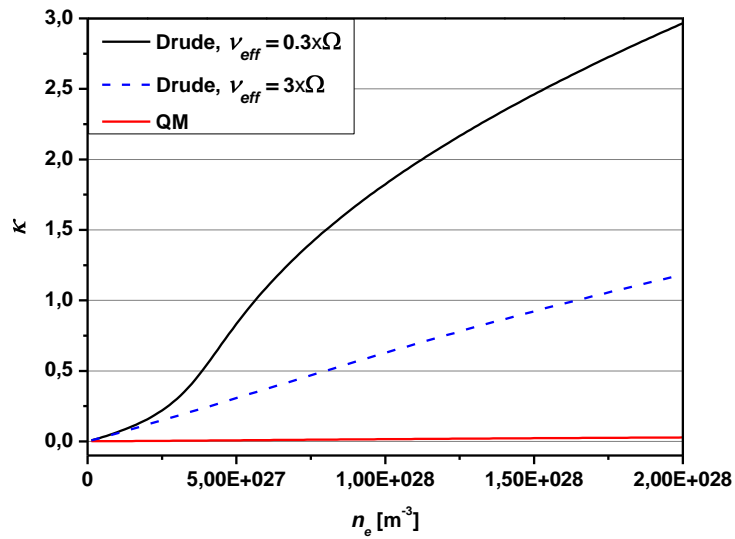


Fig. 3.21. The imaginary part of the refractive index [see eq. (3.8)] as a function of electron density. The calculation parameters are laser wavelength, $\lambda = 800$ nm; field amplitude, $E_0 = 180$ MV/cm; mean electron energy, $\langle \varepsilon \rangle = 5$ eV; energy gap, $\Delta = 9$ eV (SiO_2), and lattice temperature, $T = 300$ K.

We thus observe a significant deviation between the *classical* (Drude) and *Quantum Mechanical* approaches when collision frequency is smaller than laser frequency. However, we obtain similar results when the adjustable rate is larger than laser frequency, that is, is located in the non-physical region.

According to the classical model, the electron energy changes in a single scattering event under the action of a field. This change is, by order of magnitude, equal to $\pm eE_b p / m_{cb} \Omega$. It was shown, that Drude's formula turns out to be valid when any of the following conditions is satisfied [101,102]. The absorbed energy should be much higher than the photon energy

$$\frac{eE_b p}{m_{cb} \Omega} \gg \hbar \Omega. \quad (3.25)$$

The momentum change due to absorption should be much smaller the momentum

$$\frac{eE_b}{\Omega} \ll p. \quad (3.26)$$

If one of these conditions is justified, then the system can be described classically.

In the considered case, both conditions are not justified. Therefore, Drude model predicts incorrect results unless unphysical values of collision frequency are used. To understand why for the non-physical value of adjustable parameter the result is more satisfied we should consider the Drude expression for the energy rate in detail. This rate can be expressed as

$$\langle \dot{\varepsilon} \rangle = \frac{e^2 E_b^2}{2m_{cb} \Omega^2} \frac{\Omega^2}{\Omega^2 + \nu_{eff}^2} \nu_{eff} \Rightarrow \langle \dot{\varepsilon} \rangle = \varepsilon_L \mathbf{P}_L \times \nu_{eff}, \quad (3.27)$$

where the factor $\mathbf{P}_L = \frac{\Omega^2}{\Omega^2 + \nu_{eff}^2}$ determines the relative part of the absorbed ponderomotive energy, $\varepsilon_L = \frac{e^2 E_b^2}{2m_{cb} \Omega^2}$.

Accounting the photoionization energy in the Drude model, the energy rate is

$$\langle \dot{\varepsilon} \rangle = \varepsilon_{pi} \delta(t - \tau_{pi}) + \varepsilon_L \mathbf{P}_L \times \nu_{eff}. \quad (3.28)$$

Then, the energy as a function of pulse duration follows as

$$\langle \varepsilon \rangle_{\tau} = \langle \varepsilon \rangle_0 + \varepsilon_L \int_0^{\tau} \mathbf{P}_L \nu_{eff} \nu_{eff} dt, \text{ where } \langle \varepsilon \rangle_0 = \varepsilon_{pi} \delta_{\tau, \tau_{pi}}. \quad (3.29)$$

In the quantum mechanical case, the corresponding values are given by

$$\langle \dot{\varepsilon} \rangle = \varepsilon_{pi} \delta(t - \tau_{pi}) + \sum_l l \hbar \Omega \times \nu_l^{e-ion-ph} + \nu_l^{e-ph-ph} , \text{ where } \tau_{pi} = 1/\nu_{pi} . \quad (3.30)$$

and the energy as a function of pulse duration

$$\langle \varepsilon \rangle|_{\tau} = \langle \varepsilon \rangle_0 + \sum_l l \hbar \Omega \times \int_0^{\tau} \nu_l^{e-ion-ph} + \nu_l^{e-ph-ph} dt , \text{ where } \langle \varepsilon \rangle_0 = \varepsilon_{pi} \delta_{\tau, \tau_{pi}} . \quad (3.31)$$

Figure 3.22 clearly shows that the Drude model overestimates the absorbed energy. Essentially, it happens by two reasons. First, the ponderomotive energy is higher than photon energy for the typical experimental intensity value, see figure 3.23 (our case, $\varepsilon_L \sim 3$ eV, and $\hbar\Omega = 1.5$ eV). Second is connected with the fact that the probability of absorption is taken into account classically. When the collision rate is much smaller than the laser frequency, $\nu_{eff}^2 \ll \Omega^2$, then the energy ε_L is totally absorbed in result of each collision, that is, $P_L \rightarrow 1$. For the simplicity, the collision rate in quantum case can be expressed as $\nu_l^{e-ph/ion-ph} = P_l^{QM} \times \nu_{e-ph/ion}$, where P_l^{QM} [see Eqs. (2.42-43), (2.59-60)] is the field factor (an analog of P_L). In Figure 3.24, one can see that probability of processes with participation of photons (absorption) is less than the clear processes. Furthermore, the probability of clear processes decreases with the increase of laser field, whereas the factor P_L equals unity in the classical case as pointed above.

If the collision rate is higher than the laser frequency, $\nu_{eff} > \Omega$, then the absorbed energy is smaller than ε_L , because of the factor $P_L < 1$. Since, the value ε_L is defined by average over the wave period therefore, naturally, if collision time less than wave period, the energy ε_L cannot be totally absorbed by CB electron, only the part, $\varepsilon_L P_L < \varepsilon_L$ is absorbed by an electron in single scattering event. Thus, the increase of the effective collision rate decreases the absorbed energy, as our calculated results show based on Drude model for the effective collision rate $\nu_{eff} > \Omega$.

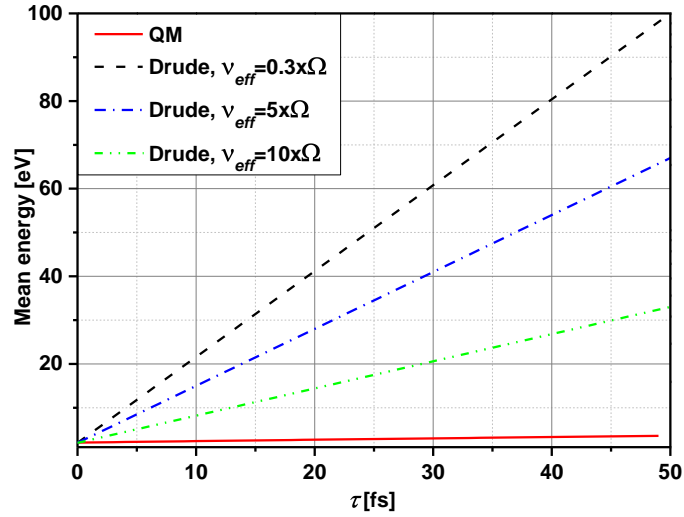


Fig. 3.22. The mean electron kinetic energy [see Eqs. (3.29, 31)] as a function of the pulse duration. The calculation parameters are laser wavelength, $\lambda = 800$ nm; field amplitude, $E_0 = 180$ MV/cm; energy gap, $\Delta = 9$ eV (SiO_2); lattice temperature, $T = 300$ K.

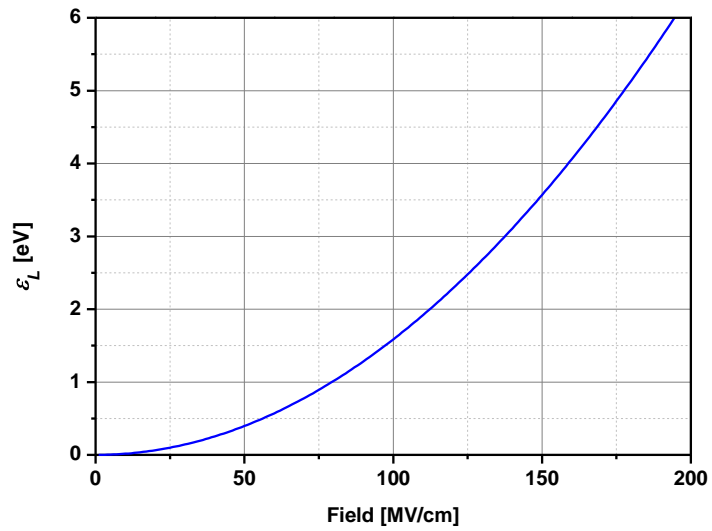


Fig. 3.23. The ponderomotive energy [see eq. (3.27)] as a function of laser field amplitude for the laser wavelength, $\lambda = 800$ nm.

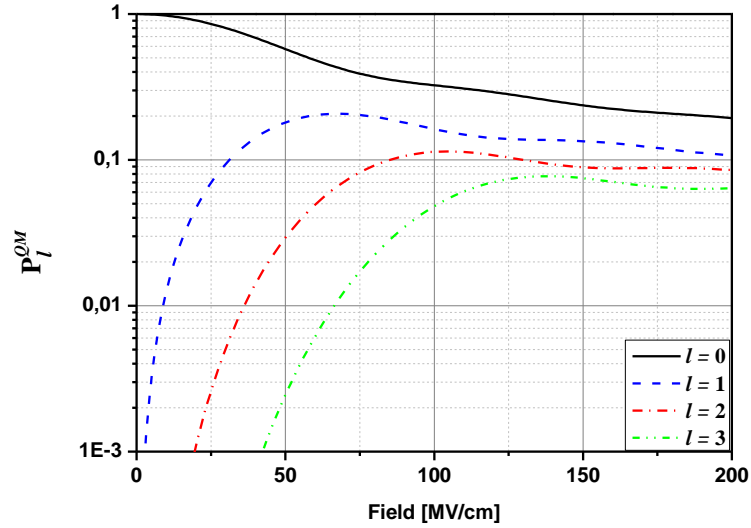


Fig. 3.24. The field factor [see eq. (2.44)] as a function of laser field. The calculation parameters are laser wavelength, $\lambda = 800$ nm; wave number in the e - ph /ion- ph t collisions, $q/\Delta k = q_{BZ}/\Delta k_{BZ}$.

Note that for metals, the energy of electron is near the Fermi level, that is, the electron momentum is large. At the same time, the field is significantly smaller than that in an insulator, and, consequently, the momentum change due to absorption is too small. Therefore, the second condition is justified, and the Drude's model agrees with the experimental results for simple metals, where other factors, such as a complicated band structure takes no place, the "cold plasma" approximation can be applied.

In many experiments, pump-probe set-ups are used for the investigation of the fast electronic processes. It should be noted, that Drude model is valid for the probe pulse due to the second condition, whereas it is invalid for the pump pulse. In fact, when Drude model is used for pump pulses, this leads to a strong electron overheating, that significantly influences the optical properties (propagation of the pump pulse) during the laser pump pulse. Consequently, incorrect laser energy deposition is obtained.

§3.5 Nonequilibrium state of electronic and phonon subsystems

We investigated the electron energy distribution (electron distribution function, or DF). The calculated DFs are shown in the Figure 3.25. One can see that right after the photoionization (first pick at the left in the Figure) and absorption (oscillations are caused by absorption of photons by free electrons scattering with phonons), the distribution is far from the equilibrium Fermi function. It takes from around 30 to 50 fs to reach equilibrium at laser pulse duration of 100 fs and laser intensity of $6.25 \times 10^{13} \text{ W/cm}^2$.

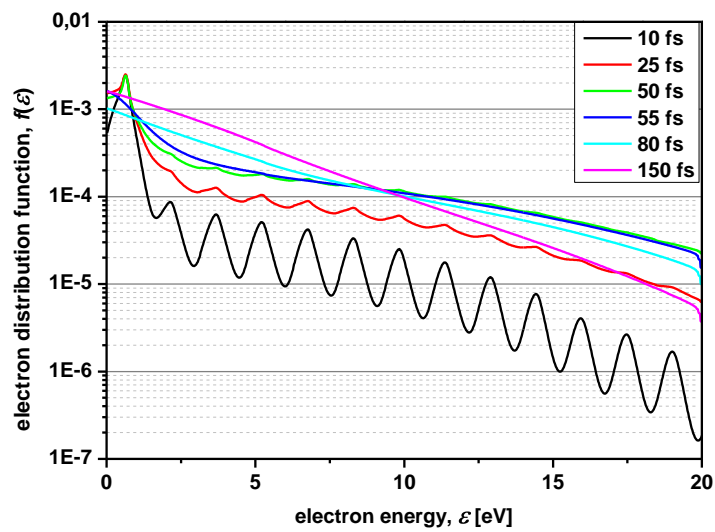


Fig. 3.25. Calculated electron energy distributions at different instants of time. The calculation parameters are laser wavelength, $\lambda = 400 \text{ nm}$, energy gap $\Delta = 9 \text{ eV}$ (SiO_2), and laser intensity $I_0 = 6.25 \times 10^{13} \text{ W/cm}^2$.

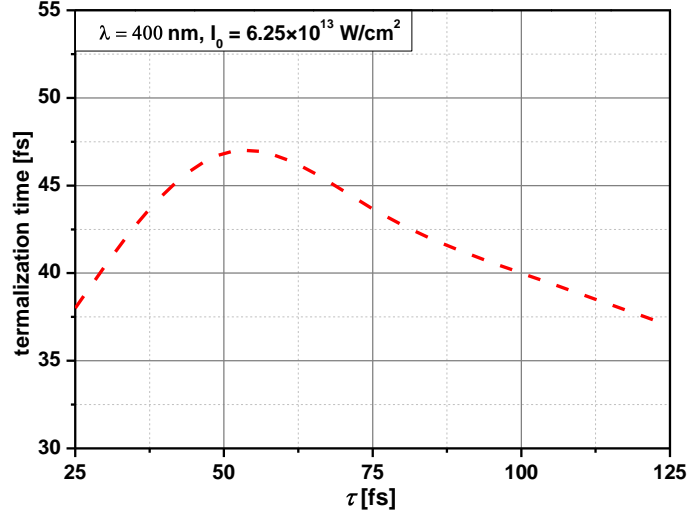


Fig. 3.26. Thermalization time as a function of pulse duration. The calculation parameters are laser wavelength, $\lambda = 400$ nm; energy gap, $\Delta = 9$ eV, and laser intensity $I_0 = 6.25 \times 10^{13}$ W/cm².

Previously, the non-equilibrium of the electrons state was shown. To characterize the electron thermalization process (energy relaxation process) we investigated the dependency of the thermalization time on laser pulse duration. To calculate the thermalization time we analyzed the entropy behavior of electrons after the end of the pulse. Thermalization occurs when the value of entropy reaches the maximum. The dependency of the thermalization time on the pulse duration is presented in the figure 3.26. One can see that a maximum of the thermalization time can be observed when the pulse duration, τ , equals 55 fs. This behavior can be explained as follows. When the density of free electrons is small, the collision rates of absorption and photoionization, which are responsible for the disordering, is larger than the rate of the *electron-electron* (*e-e*) collisions, which are responsible for the thermalization. With increasing laser pulse duration (keeping the same laser field, or intensity), the electron density increases, and the *e-e* collisions become more frequent. Furthermore, partial thermalization occurs during the laser pulse. As a result, electrons reach more rapidly the equilibrium state when laser pulses are longer.

The frequency of the *e-e* collisions that is responsible for thermalization as shown in Figure 3.27. Both electron energy and the number density of conduction band electrons affect these collisions. Interestingly, with the rise in the mean electron energy, the frequency of the *e-e* collisions decreases. This effect can be attributed to the local screening effect, as one can see from the expression for q_0 , Eq. (2.21). When the mean electron energy is small and the number density of the created conduction electrons, n_e , increases, the *e-e* collision density decays. On the contrary, at larger mean electron energy, the frequency of the *e-e* collisions rises with n_e .

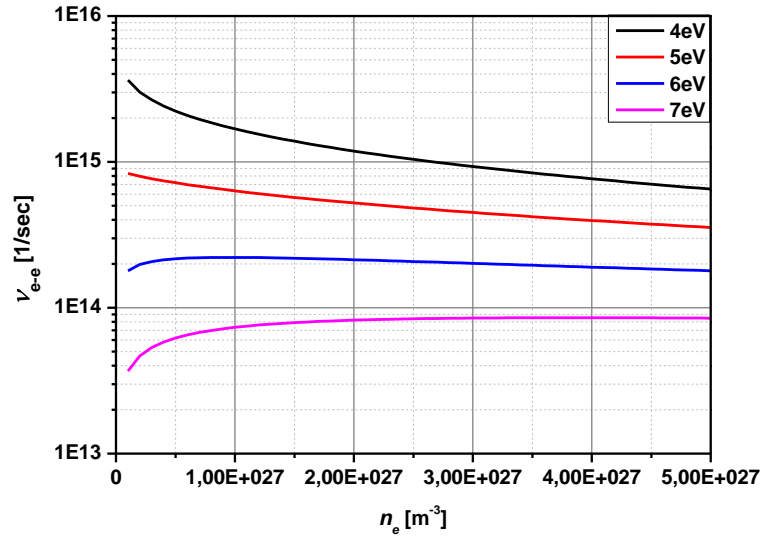


Fig. 3.27. Electron-electron collision rate [see eq. (2.24)] as a function of the conduction band electron's number density for several different values of the mean electron energy.

§3.6 Time-resolved study of the ultrafast electron excitation/relaxation

Previously, pump-probe techniques were successfully used to study the dynamics of conduction electrons in dielectrics [49,103,104]. Here, we compare our results with the results obtained by this technique.

One of the first results was obtained by Audebert *et al.* [103]. The principle of this experiment is based on interferences in the frequency domain. The target is probed with two collinear femtosecond pulses separated by a fixed time delay Δt . The high intensity pump pulse excites the solid between the first pulse (reference) and the second one (probe). It results in a change $\Delta\eta = \eta - \eta_1$ in the refractive index of the dielectric material (η_1 refractive index of the non-excited solid), which leads to a change $\Delta\Phi$ ($\Delta\Phi \propto \Delta\eta$) in the relative phase of the reference and the probe. Thus, a measurable shift of the spectral fringes is obtained. The phase shift can be measured as a function of time by changing the delay between the pump pulse and the probe pulses; the absorption of the probe pulse is obtained simultaneously by measuring the fringe contrast directly on the interference pattern. The experimental setup is shown in Fig. 3.28.

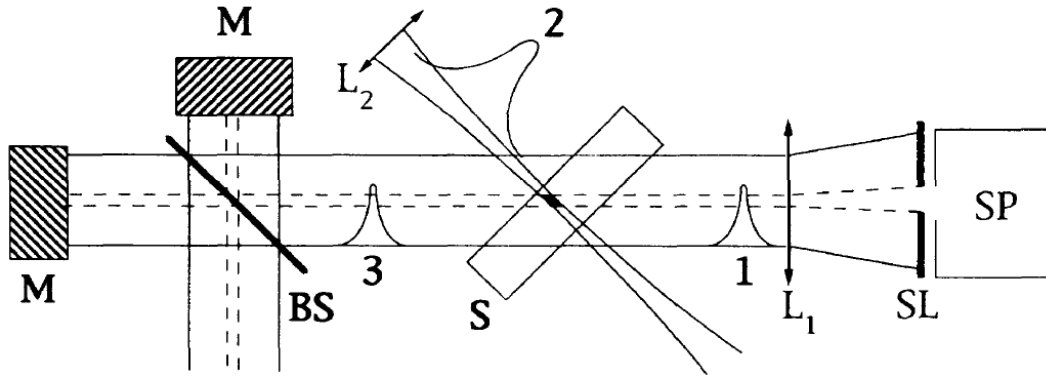


Fig. 3.28. Principle of the experiment. **M**: mirror; **BS**: beam splitter; **S**: sample; **SL**: slit; **SP**: spectrometer; **1,3**: probe pulses; **2**: pump pulse; **L₁**: imaging lens, **L₂**: focusing lens. The black area represents the interaction region imaged on the slit **SL** by **L₁**. The corresponding light rays are symbolized by the dashed lines.

Because the probe pulse is of small intensity, therefore $\dot{\sigma}_r \ll \dot{\sigma}_i$ then $\eta \approx \sqrt{\dot{\sigma}_r} \left(1 + \dot{\sigma}_i^2 / 8\dot{\sigma}_r^2 \right)$ and $\Delta\eta \propto \Delta \dot{\sigma}_i^2$. However, the energy absorption rate is $\dot{Q}_e \propto \dot{\sigma}_i$ [eq. (3.12)], and, according to the Drude model, the imaginary part of the dielectric function is $\dot{\sigma}_i^{Dr} \propto n_e v_{eff}$ [eq. (3.15)], then phase shift is $\Delta\Phi \propto \Delta \left[n_e v_{eff}^2 \right]$. That is, the change, $\Delta\Phi$ occurs due to the change of electron density and the collision frequency. The collision frequency is a function of the electron mean energy, electron density and lattice temperature, $v_{eff} = n_e \langle \varepsilon \rangle, T = v_{e-ph} \langle \varepsilon \rangle, T + v_{e-ion} n_e \langle \varepsilon \rangle$. The decrease of electron density occurs due to Auger processes and STE (Self-Trapped Exciton) mechanism (when electron has low energy, less 1 eV),

$\dot{n}_e n_e, \langle \varepsilon \rangle = \Delta \dot{n}_{Auger} n_e, \langle \varepsilon \rangle + \Delta \dot{n}_{STE} n_e, \langle \varepsilon \rangle$. To identify the mechanism which is responsible for the behavior of phase shift and probe-free carrier absorption we should explore their behavior with time.

According to our calculation (Fig. 3.14), the mean energy is in the range between 5 and 10 eV. In Figure 3.31, we can see that the Auger scattering rate is too small, $< 10^{12}-10^{13} \text{ sec}^{-1}$, in this energy range for the interesting electron density domain, $10^{21}-10^{22} \text{ cm}^{-3}$. Therefore, the Auger rate cannot significantly influence electron density unless the electron energy is above 5 eV. Furthermore, this process is negligible if the electron density is than smaller 10^{21} cm^{-3} . Thus we have two possibilities to describe the results of Figures 3.29 and 3.30: (a) decreasing electron density due to STE; (b) decreasing the effective collision frequency. In fact, the STE formation takes place only if the electron energy is lower than 1 eV, because high energy electrons cannot be localized. These electrons need to decrease their energy before an STE can be formed.

To analyze the behavior of the $e-ph$ scattering rate as function of electron energy (Fig. 3.32), the rate decreases with the decrease in the electron energy. Thus, because of the energy transfer from the CB electrons to lattice, the absorption decreases too. Moreover, according to our calculations, the time required to reach energy of $\sim 1 \text{ eV}$ is about 0.8 ps. Also, it can be estimated as follows, $\Delta \varepsilon \approx \hbar \omega_{ph} \times v_{eff} \times \Delta t$, where $\hbar \omega_{ph} = 0.1-0.2 \text{ eV}$ (Appendix F), $v_{eff} \approx 10^{14} \text{ sec}^{-1}$ (Fig. 3.32), and $\Delta \varepsilon = 5-10 \text{ eV}$ (Fig. 3.14). This time defines the delay when the trapping processes are playing an important role.

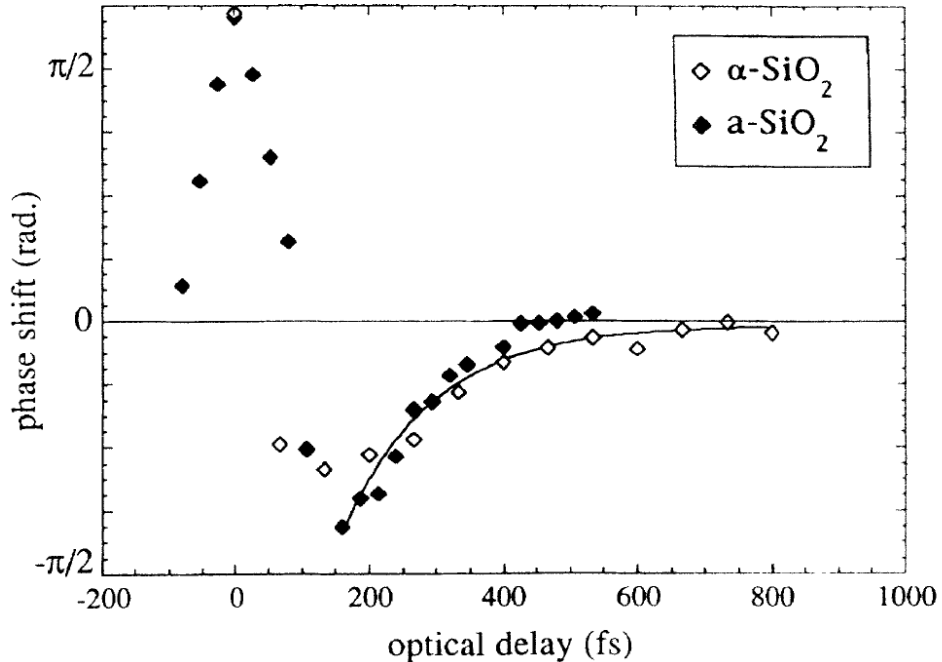


Fig. 3.29. Phase shift as a function of time for $\alpha\text{-SiO}_2$ and a-SiO_2 . Solid line: exponential fit, with a time decay of 150 fs. Pump intensity of $2.7 \times 10^{13} \text{ W/cm}^2$ (90 fs).

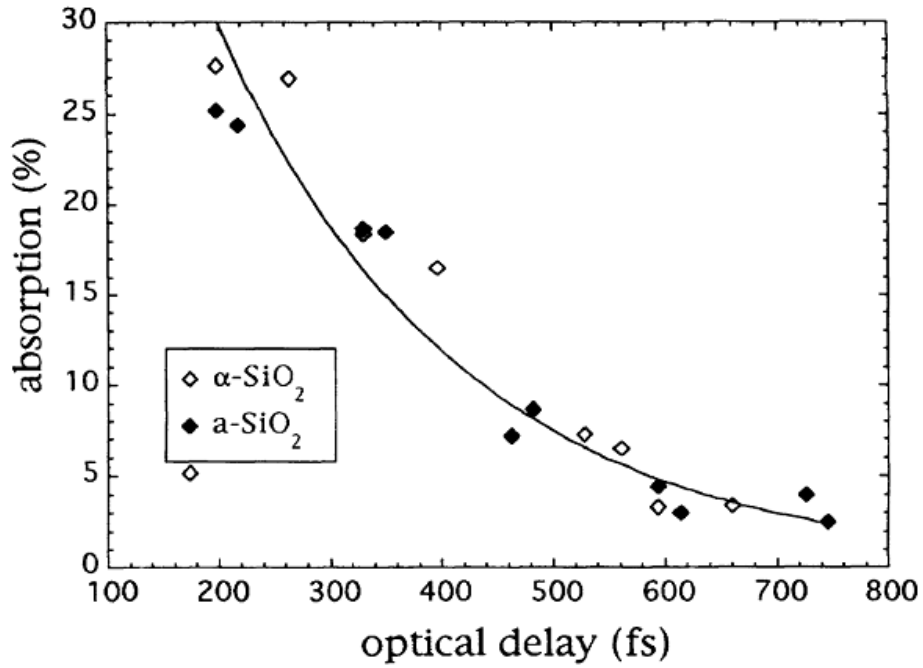


Fig. 3.30. Probe-free carrier absorption as a function of time for α -SiO₂ and a-SiO₂. Solid line: exponential fit with a time decay of 200 fs. Pump intensity of 2.7×10^{13} W/cm² (90 fs).

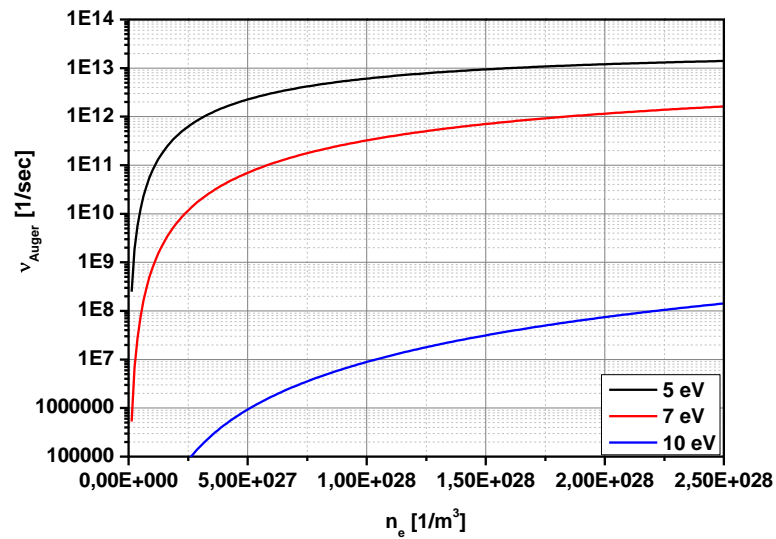


Fig. 3.31. Auger scattering rate (Appendix I) as a function of electron density for different values of mean electron energy. The results are obtained for the following parameters: reduced mass, $m_r = 0.5 m_0$; energy gap, $\Delta = 9$ eV.

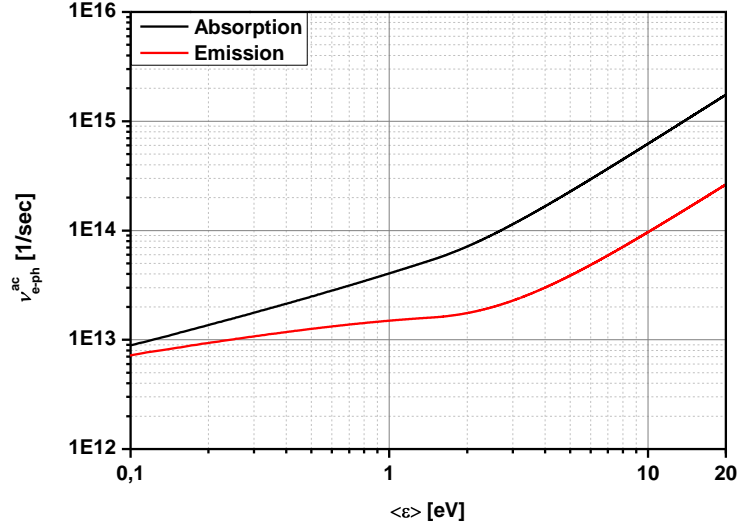


Fig. 3.32. Electron-phonon (acoustic) collision frequency [see eq. (2.46)] as a function of the electron mean energy (lattice temperature, $T = 300$ K).

Furthermore, Quéré *et al.* [49] presented a femtosecond time-resolved study of the evolution of the laser-excited carrier density with the laser intensity. In Figure 3.33, the evolution of $\Delta\Phi_{\infty}$ with the incident peak intensity is displayed, where $\Delta\Phi_{\infty}$ is the phase shift, $\Delta\Phi(t)$ for large enough delays after the pump pulse (see the inset in the fig. 3.33). Authors show, that at higher intensities, a saturation of $\Delta\Phi_{\infty}(I)$ is observed compared to the power law I^{ρ} ($n = 6$ corresponds to the MPI for the SiO_2). The OBT (optical breakdown threshold) falls within this saturation range. On the contrary, if the optical breakdown is associated with an electronic avalanche, a strong increase in the electronic density compared to this power law should be expected upon the OBT. This fact indicates that no electronic avalanche occurs, in agreement with our conclusion in the section 3.3.2.

To identify the electronic excitation mechanisms, it is necessary to understand why the saturation of $\Delta\Phi_{\infty}(I)$ occurs. It was proposed [49], that at high laser intensity, the attenuation of the pump beam can be very strong at the probed length, for two reasons. First, each creation of an electron-hole pair by multiphoton absorption annihilates n photons. Second, once sufficient number of the electrons are injected in the CB, the solid acquires a metallic character. It can absorb pump photons through free-carrier absorption (Joule heating). These absorption processes both depend strongly and non-linearly on laser intensity. In the case of free-carrier absorption, this dependency is due to the proportionality to the density of excited carriers. As a consequence, as the intensity increases, they prevent more and more efficiently the penetration of the pump beam in the solid, which is thus more and more inhomogeneously excited. However, this is not a single reason. In previous section we demonstrated (Fig. 3.13-15, 3.24) the saturation due to the field and electron density effects, that completes the explanation of Quéré *et al.*[49].

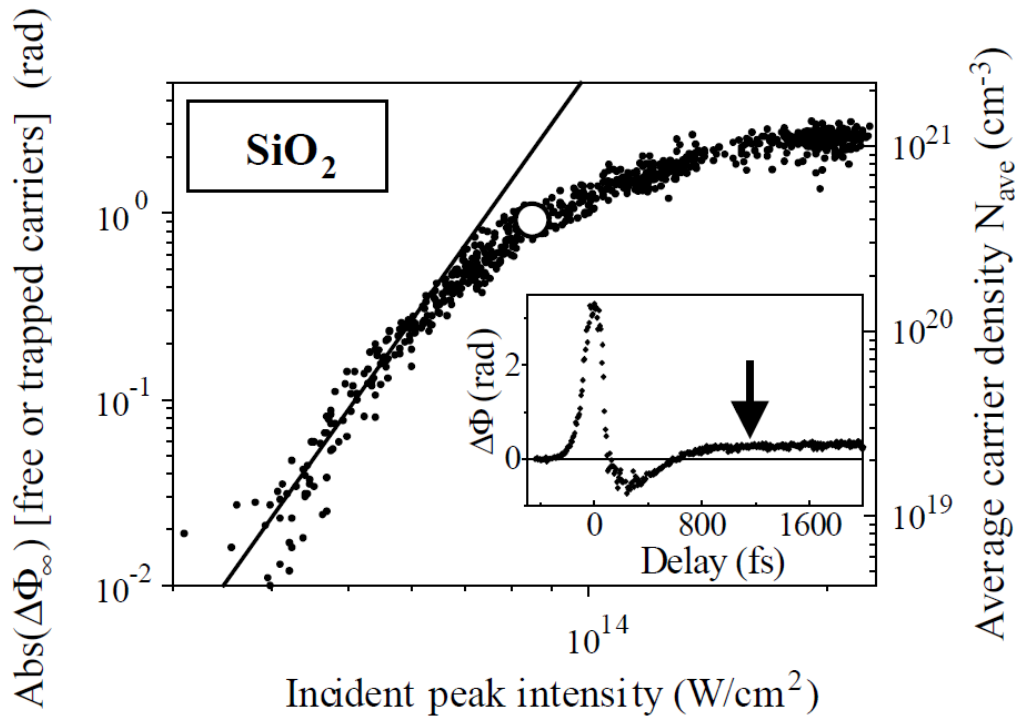


Fig. 3.33. Circles: evolution of $\Delta\Phi_\infty$ with the incident peak intensity of a 790 nm, 60 fs pump pulse. Open circle: OBT at 60 fs. Full line: I^6 law. Insets: temporal evolution of $\Delta\Phi$. The arrow indicates the typical delays at which $\Delta\Phi_\infty$ was measured.

Chapter 4

On the damage criterion

A correct definition of laser damage criterion is a challenging task. Previously, the criterion of optical breakdown (OB) was used based for the definition of the so-called “critical electron density” as follows from $n_e \geq n_{cr}^{o.b.}$, $n_{cr}^{o.b.} = \sqrt{\epsilon_0 m_{cb} \Omega^2 / e^2}$ [32,105]. This simple criterion is borrowed from the DC damage investigations and was used for the AC damage later. Firstly, it was applied to the process of gas breakdown [106], because if the plasma frequency equals the laser frequency, then total screening is observed. To connect these measurements with the electronic excitation mechanisms, it is postulated that breakdown occurs when the excitation density reaches a critical value $n_{cr}^{o.b.}$ independent of the pulse duration τ . The measurements in solids show that this assumption is not valid [40,49,94]. The exact law for damage as a function of n_e and τ must be determined based on a mechanism, through which the excitation leads to the solid damage.

In solids, both electron energy and material properties are completely disregarded in this definition. Moreover, a situation is possible when the critical density is reached at the end of the pulse but the density of free electrons with enough energy to ionize other neutral atoms/molecules is not high enough to support avalanche and thus further grow of electron density does not practically happen. It should be noted that only extensive bond breaking could guarantee laser damage, rather than OB itself.

Therefore, based on our calculations, we can propose a more relevant definition of the electron density required for damage. For this, we propose to compare the total energy of free electrons per unit volume (electron energy density, $Q_e t$) in the end of the laser pulse, $t = \tau$, with kinetic energy of lattice at melting temperature, $Q_{ph} T_m$

$$Q_e \tau / 2 > Q_{ph} T_m, \quad (4.1)$$

where $Q_e t = \frac{1}{2\pi^3} \int \epsilon_{tot} k f t, k d^3k$ is the total energy density of free electrons in J/m^3 ;

$\epsilon_{tot} k = \epsilon k + \Delta$, $Q_{ph} T = \sum_{\beta} \frac{1}{2\pi^3} \int \hbar \omega_{\beta} q g_{\beta} q, T d^3q$ is the energy density of lattice in

J/m^3 . Also, to calculate the energy density of lattice at melting temperature, we just suppose that the phonon system is at equilibrium and use the Bose-Einstein distribution for the phonon subsystem.

Therefore, the electron energy density can be presented as $Q_e = n_e \epsilon_{tot}$, where $\epsilon_{tot} = \langle \epsilon \rangle + \Delta$. Then we obtain the following condition of thermal criterion

$$n_e > n_{cr}^{th}, n_{cr}^{th} = \frac{2Q_{ph} T_m}{\epsilon_{tot}}. \quad (4.2)$$

Note, that material properties are taken into account in this criterion.

For wide-gap dielectrics and for short pulses when photo-ionized electrons have no time to absorb additional energy, i.e. $\epsilon_{tot} \approx l_{pi} \hbar \Omega$, and by using simple expression for the $Q_{ph} T_m \approx 3k_B T_m / 2V_{at}$, we can rewrite our condition as following

$$n_e > n_{cr}^{th}, n_{cr}^{th} \approx \frac{3k_B T_m}{V_{at} l_{pi} \hbar \Omega}, \quad (4.3)$$

where V_{at} is the mean volume of atom.

Since, we revealed that the role of the impact ionization process is negligible, that is $n_e t \ll W_{pi} \Omega, E_b \cdot t$, to calculate roughly the energy density per unit volume for long pulses can be applied the equations from (3.22), and then the energy density in quasi-equilibrium terms (due to long pulses) is

$$Q_e t = \int_0^t \dot{Q}_{pi} t' + \dot{Q}_{e-ion-ph} t' + \dot{Q}_{e-ph-ph} t' dt'. \quad (4.4)$$

To check the validity of this criterion we perform a comparison with the previous experiment findings (Figure 4.1) [62]. It should underline that in the calculations we compared the energy density for electron and phonon sub-systems.

The results show a good agreement with the experimental data of Sanner *et al.* [62] for the pulse duration region longer than from 50 to 70 fs. Also, the figure clearly shows that using parabolic model for the photoionization rate agrees better with experiments than Kane band structure model.

However, for shorter laser pulses, the presented theoretical description of laser excitation and absorption processes is incomplete, which explains the observed discrepancy. In the range < 50 fs of laser pulse duration, the laser field amplitude is so high that the *Keldysh* approach cannot be applied to consider correctly the photo-ionization. This pulse duration is too short that, in fact, the intraband processes (electron-phonon/ion-photon) cannot significantly contribute to absorption, despite that the taking into account of the multiphoton electron heating with respect

to one-photon of Kaiser *et al.* [14] decreases the threshold field in this range. Evidently, it is not possible to make up for the lacking order of magnitude considering only electron—phonon/ion scattering. Thus a necessity arises to search for other electron heating channels that would provide a higher rate of energy accumulation, and improve the theory of photo-ionization, or for a non-electronic damage mechanism, or for another damage criteria. Probably, the role of interband processes [107] in conduction band is underestimated in this case.

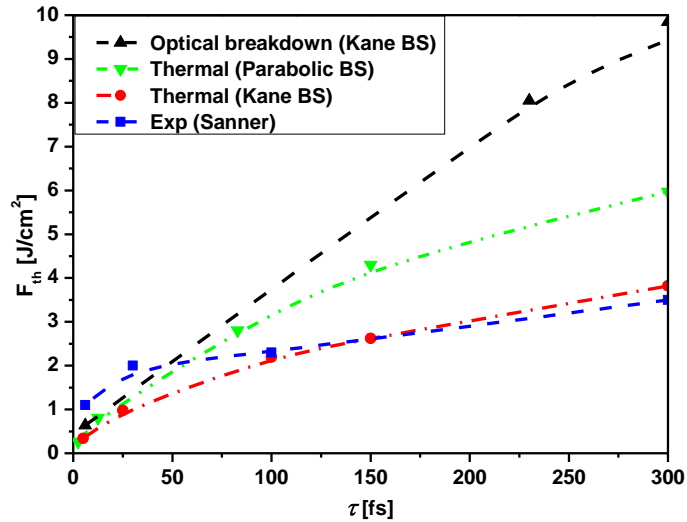


Fig. 4.1. Calculated and measured damage thresholds are shown. The black dash and red dash-dot curves correspond to the optical breakdown criterion and thermal criterion for Kane BS, respectively. The green dash-dot-dot curve corresponds to the thermal criterion for Parabolic BS. The blue dash curve shows the results of experiments by Sanner *et al.* [62]. Here, laser wavelength, $\lambda = 800$ nm; energy gap, $\Delta = 9$ eV (SiO_2).

Chapter 5

General conclusions

In this manuscript I have presented the results of my work at Hubert Curien Laboratory that I have performed during 2009-2013. In particular, I have investigated ultra-short laser interactions with dielectric materials. For this, I have developed a complete model of femtosecond-laser interaction with dielectric materials. The main objective of this work has been a better understanding of the mechanisms involved in laser interaction and a definition of damage threshold for optical components used in ultra-powerful laser systems. Further development of laser applications should benefit from this study.

I have presented a numerical analysis of the physical mechanisms involved in ultra-short laser interactions with dielectric materials. The developed model accounts for the absence of equilibrium in electron and phonon subsystems. All collisional processes involved in both electronic excitation and relaxation processes are taken into account.

The calculations are performed for quartz. The obtained results demonstrate that the electron thermalization time depends on laser parameters, such as pulse duration and laser fluence. These results have been attributed to the difference in free electron densities that are reached. The frequency of electron-electron collisions are presented as a function of the electron number density and mean energy.

Then, I have investigated the rates of photo- and electron impact- ionization processes. The calculation results are compared for two different band structures: (i) Kane's model and (ii) parabolic band structure. In both cases oscillations are observed when laser field increases. The rates calculated based on Kane's model are found to be higher than that calculated for parabolic BS.

For typical laser fields used in experiments, comparable frequencies have been obtained for both photo- and impact ionization processes. However, the role of impact- and field-assisted impact- ionization is negligible for pulse duration < 100 fs and laser intensity $< 10^{14}$ W/cm², that confirms the experimental results [40,49,93,94].

In addition, free electron absorption is examined. For higher laser fields, the limits of the validity of Keldysh model have been demonstrated because of the transitions beyond the first Brillouin zone.

Furthermore, I have compared laser energy absorption calculated by our model with that obtained from a classical Drude model. It has been demonstrated that Drude model overestimates this absorption. With the decrease in the effective collision frequency, the deviation between the results rises. This deviation is attributed to the role of laser field inside the dielectric material that affects the involved collisions. In addition, the role of the local screening effect depending on the free electron density and laser field are shown to be affected on the electron mean energy. This effect is demonstrated in the investigation of laser absorption efficiency as a function of laser parameters.

The calculated time-scales of the electronic excitation/relaxation process agree with the experimental results [49]. In addition, our model confirms the conclusion [103] about the phase shift saturation with intensity.

Finally, laser damage criteria have been examined. The criterion based on the optical breakdown (OB) yields the critical density of about one percent from the total amount of valence-band electrons. This criterion, however, contains no information about electron energy nor about the bond breaking process. Therefore, a more precise criterion is proposed that provides more correct values for the damage threshold [62].

Perspectives

The presented study has many perspectives, both theoretical and practical. First of all, a more detailed analysis can be performed for a more realistic band structure. Thus, from theoretical point of view, the performed studies can be extended by including the multiple band structure to describe correctly the electron-phonon/electron collisions. Then, for the multiple BS, I propose to consider the direct transition of the electrons between different conduction bands (interband transitions).

The photoionization process also needs more analysis. Based on the analytical calculations, it is possible to further improve the calculation of the PI rate. Furthermore, the accuracy of the PI rate calculations will be improved by including the electron-hole interaction (excitonic effect).

In addition, it will be important to compare the results obtained for different laser polarizations (for instance, linear and circular). There are several experiments (e.g. the time-resolved and double pump-probe technique by Guizard *et al.* [93]) that demonstrate the role of self-trapped excitons. It is therefore imperative to consider the photoionization through the self-trapped exciton level and the photoionization from the self-trapped exciton level to the conduction band.

The practical perspectives are also numerous. In particular, the developed model can be used for further development of ultra-powerful laser system based on a better evaluation of the material damage thresholds. Then, the precision of laser micromachining can be improved. The development of optical components, such as polarizers, gratings, mirrors, etc can also benefit from the presented study. In particular, the developed model can be used to study optical properties as non *ab initio* methods, therefore it does not require the high-performance calculation. This is particularly important for the description of pump-probe technique experiments.

Finally, such processes as electron diffusion, lattice structural modifications and propagation should be included to evaluate the size of the damaged area.

Appendix A. Validity

In what follows we define the validity limits of the Boltzmann equation. First of all, this equation describes correctly the system of particles if the smallest scattering time, τ_{\min} is larger or comparable with the time step, Δt (0.1-0.5 fs) used in the calculations. The largest collision frequency that determines the shortest collision time is the electron-electron collision time.

The first condition is therefore

$$\Delta t \leq \tau_{\min}. \quad (\text{A.1})$$

The second condition is connected with the largest collision time. In fact, the total calculation time (laser pulse duration, τ_p) should be much longer than the effective collision time

$$\tau_p \gg \tau_{\text{eff}}. \quad (\text{A.2})$$

Now, we define the values of $\tau_{\min} \approx 1$ fs and $\tau_{\text{eff}} \approx 5-10$ fs; $\tau_{\min/\text{eff}} = \min/\text{eff} \tau_{e-e}, \tau_{e-ph}, \tau_{e-ion}$. We use the typical pulse durations 50-300 fs to justify this condition.

In addition, all scattering times should be larger than the uncertainty time of the “mean” electron. Hence, we can rewrite the third condition as following

$$\tau_{sc} > \Delta \tau, \quad (\text{A.3})$$

where $\Delta \tau \geq \hbar/\langle \varepsilon \rangle$ is the time uncertainty, and $\tau_{sc} = \forall \tau_{e-e}, \tau_{e-ph}, \tau_{e-ion}$ is a scattering time.

The initial electron energy is above 1 eV due to photoionization process. Therefore, $\tau_{sc} \geq 0.6$ fs. This condition is satisfied in the case of quartz.

The absorption or emission of a phonon by free electrons is the result of one e-ph/ion collision. To absorb or emit one phonon, an electron should spend time larger or comparable with phonon period. In other words, the electron is in the phonon field, and the electron needs to spend more phonon period time to absorb a phonon. Therefore, the e-ph collision scattering rate should be smaller than the phonon frequency. That is the 4th condition

$$\omega_{ph} > \nu_{e-ph}. \quad (\text{A.4})$$

This condition also is satisfied.

In the case of laser energy absorption, the e-ion-ph, and e-ph-ph collisions should satisfy the following 5th condition

$$\tau_{LF} < \forall \tau_{e-ion-ph}, \tau_{e-ph-ph}, \quad (\text{A.5})$$

where τ_{LF} is the wave period of the applied laser field. The wavelength of 800 nm corresponds to $\tau_{LF} \approx 0.4$ fs. This condition also is satisfied.

Appendix B. Special functions

To calculate the matrix element in the electron-electron collision integral we use the following expression

$$\int \frac{dk}{k^2 + q_0^2} = \frac{1}{2q_0^3} \left[\arctan\left(\frac{k}{q_0}\right) + \frac{kq_0}{k^2 + q_0^2} \right] + Const. \quad (\text{B.1})$$

To calculate the matrix element in the impact ionization collision integral we use the following expression

$$\int \frac{k^2 dk}{k^2 + q_0^2} = \frac{1}{2} \left[\frac{1}{q_0} \arctan\left(\frac{k}{q_0}\right) - \frac{k}{k^2 + q_0^2} \right] + Const. \quad (\text{B.2})$$

The complete elliptic integral of the first kind is

$$K(k) = \int_0^{\pi/2} \frac{d\phi}{\sqrt{1 - k^2 \sin^2 \phi}} = \int_0^1 \frac{dx}{\sqrt{(1-x^2)(1-k^2x^2)}}. \quad (\text{B.3})$$

The complete elliptic integral of the second kind is

$$E(k) = \int_0^{\pi/2} \sqrt{1 - k^2 \sin^2 \phi} d\phi = \int_0^1 \frac{\sqrt{1 - k^2 x^2}}{\sqrt{1 - x^2}} dx. \quad (\text{B.4})$$

The Dowson's integral is expressed as

$$\phi(z) = \int_0^z \exp(y^2 - z^2) dy. \quad (\text{B.5})$$

The Bessel function of integer order can be calculated as

$$J_n(x) = \frac{1}{\pi} \int_0^\pi \cos(n\tau - x \sin \tau) d\tau. \quad (\text{B.6})$$

The relation of the Bessel functions for the positive and negative order is

$$J_{-n}(x) = (-1)^n J_n(x). \quad (\text{B.7})$$

The arc-hyperbolic sine function is

$$\text{Arsh } x = \ln(x + \sqrt{1 + x^2}). \quad (\text{B.8})$$

Appendix C. Delta-function approximation

To calculate the photoionization collision integral we use the following approximation of Delta-function

$$\delta(x) \stackrel{def}{=} \lim_{\alpha \rightarrow 0} \frac{1}{\alpha\sqrt{\pi}} \exp\left[-\left(\frac{x}{\alpha}\right)^2\right] \Rightarrow \delta(x-x_0) = \lim_{\alpha \rightarrow 0} \frac{1}{\alpha\sqrt{\pi}} \exp\left[-\left(\frac{x-x_0}{\alpha}\right)^2\right], \quad (\text{C.1})$$

where the parameter α is responsible for the height and width of the Delta-function. This parameter is the order of the integration step h .

Appendix D. Integration and derivation schemes

To calculate the collision integrals we use the Trapezium method

$$\int_a^b f(x) dx = \frac{h}{2} \left(f(a) + 2 \sum_{i=1}^{n-1} f(x_i) + f(b) \right), \quad (\text{D.1})$$

where $x_i = a + ih$ and $h = \frac{b-a}{n}$.

The integration step h is chosen according to the scales of the observed physical processes in the system eq. (2.5).

For $n \gg 1$, two-dimension integral can be calculated as

$$\int_a^b \int_a^b f(x, y) dx dy \cong h^2 \sum_{i=0}^n \sum_{k=0}^n f(x_i, y_k). \quad (\text{D.2})$$

To solve the differential equation we applied the Euler scheme

$$\frac{f(x, t_{i+1}) - f(x, t_i)}{\Delta t} = \Phi(x, t_i), \quad (\text{D.3})$$

where $t_{i+1} = t_i + \Delta t$.

Appendix E. Photo-ionization matrix element derivation

The density rate equals the photoionization rate per unit volume, that is

$$\dot{n}_{pi} = W_{pi} = \frac{1}{2\pi^3} \int \left. \frac{\partial f}{\partial t} \right|_{pi} d^3k = \frac{1}{2\pi^3} \int_0^\infty \left. \frac{\partial f}{\partial t} \right|_{pi} 4\pi k^2 dk. \quad (\text{E.1})$$

Momentum integration is replaced by energy integration as

$$W_{pi} = \frac{1}{4\pi^2} \left(\frac{\sqrt{2m_{cb}}}{\hbar} \right)^3 \int_0^\infty \left. \frac{\partial f}{\partial t} \right|_{pi} \sqrt{\varepsilon} d\varepsilon. \quad (\text{E.2})$$

Substitution of the collision integral (Parabolic band-structure) eq. (2.15) in eq. (E.2) leads to the following expression

$$W_{pi} = \frac{1}{4\pi^2} \left(\frac{\sqrt{2m_{cb}}}{\hbar} \right)^3 \int_0^\infty \frac{2\pi}{\hbar} \sum_n |M_{pi,n}|^2 f_v \varepsilon_v (1 - f_\varepsilon) \frac{m_r}{m_{cb}} \delta(\varepsilon - \varepsilon_{pi,n}) \sqrt{\varepsilon} d\varepsilon \quad (\text{E.3})$$

In the initial time $f_v \varepsilon_v \rightarrow 1$ and $f_\varepsilon \rightarrow 0$, respectively. Then eq. (E.3) can be calculated as

$$W_{pi} = \frac{2\pi}{\hbar} \frac{1}{4\pi^2} \left(\frac{\sqrt{2m_{cb}}}{\hbar} \right)^3 \sum_n |M_{pi,n}|^2 \frac{m_r}{m_{cb}} \sqrt{\varepsilon_{pi,n}} \quad (\text{E.4})$$

and with help of $W_{pi} = \sum_n W_{pi,n}$

$$|M_{pi,n}|^2 = \frac{\hbar}{2\pi} \frac{2\pi^2 \hbar^3 W_{pi,n}}{\sqrt{2m_{cb} m_r^2 \varepsilon_{pi,n}}} \delta_{\varepsilon, \varepsilon_{pi,n}}. \quad (\text{E.5})$$

Appendix F. Reference data of target properties (SiO₂)

Calculation parameters, where LO stands for longitudinal optical phonons, TO represents transversal optical phonon mode, and $\Xi_{\beta} = \left(\frac{1}{\varepsilon_{>}^{\beta}} - \frac{1}{\varepsilon_{<}^{\beta}} \right)$, $\beta \neq 0$; $\varepsilon_{>}^{\beta}$ is the high frequency (optical) and $\varepsilon_{<}^{\beta}$ is low frequency (static) dielectric constant of β -th LO mode, respectively.

Notation		Value	Unit	Ref.
c	light speed	2.998×10^8	m·sec ⁻¹	[108,109]
e	elementary charge	1.602×10^{-19}	Q	[108,109]
m_0	free electron mass	0.911×10^{-30}	kg	[108,109]
\hbar	Planck constant	1.055×10^{-34}	J·sec	[108,109]
k_B	Boltzmann constant	1.380×10^{-23}	J·K ⁻¹	[108,109]
ϵ_0	electric permittivity of vacuum	8.854×10^{-12}	F·m ⁻¹	[108,109]
Δ	energy gap (SiO ₂)	9.0	eV	[108,109]
C_{AC}	acoustic deformation potential (SiO ₂)	3.5	eV	[110]
m_{cb}	conduction band electron mass (SiO ₂)	0.911×10^{-30}	kg	-
m_{vb}	valence band electron mass (SiO ₂)	0.911×10^{-30}	kg	-
Ξ_{TO}	optic deformation potential (SiO ₂)	2.0×10^9	eV·cm ⁻¹	[110]
Ξ_1	- // - (SiO ₂)	0.063	-	[110]
Ξ_2	- // - (SiO ₂)	0.143	-	[110]
v_s	speed of sound (SiO ₂)	4500	m·sec ⁻¹	[108,109]
k_{BZ}	Brillouin zone edge vector (SiO ₂)	1.239×10^{10}	m ⁻¹	[110]
ρ	target density (SiO ₂)	2650	kg·m ⁻³	[108,109]
n_0	initial electron density (SiO ₂)	10^{14}	m ⁻³	[110]
ω_1	LO ₁ frequency (SiO ₂)	95.706×10^{12}	sec ⁻¹	[110]
ω_2	LO ₂ frequency (SiO ₂)	232.429×10^{12}	sec ⁻¹	[110]
ω_{TO}	TO frequency corresponded LO ₁ mode (SiO ₂)	269.406×10^{12}	sec ⁻¹	[110]
T_0	initial temperature of electron/phonon gas	300	K	-

Appendix G. Photo-ionization rate expressions

Parabolic band structure

The expression of photo-ionization rate for parabolic band structure is [84]

$$W_{pi}^G = s \frac{2\Omega}{9\pi} \left(\frac{m_r \Omega}{\hbar} \right)^{3/2} Q^G \gamma, x \times \exp \left[-2l_{pi} \operatorname{Arsh} \sqrt{2\gamma} - \Theta - 2x \frac{2\Theta\gamma^2}{1+4\gamma^2} \right]. \quad (\text{G.1})$$

The factor 1/9 is connected with the saddle-point contribution and corresponds to the Kane BS whereas in the parabolic BS the saddle-point contribution is 1/16, therefore the correct expression is given by

$$W_{pi}^G = s \frac{\Omega}{8\pi} \left(\frac{m_r \Omega}{\hbar} \right)^{3/2} Q^G \gamma, x \times \exp \left[-2l_{pi} \operatorname{Arsh} \sqrt{2\gamma} - \Theta - 2x \frac{2\Theta\gamma^2}{1+4\gamma^2} \right] \quad (\text{G.2})$$

with

$$Q^G \gamma, x = \sqrt{1/\Theta} \sum_{n=0}^{n_{\max}} \exp \left[-2n \operatorname{Arsh} \sqrt{2\gamma} - \Theta \right] \times \phi \sqrt{2\Theta l_{pi} - x + n}, \quad (\text{G.3})$$

where

$$\gamma = \frac{\Omega \sqrt{m_r \Delta}}{eE_b}; \quad \tilde{\Delta} = \Delta \left(1 + \frac{1}{4\gamma^2} \right); \quad x = \tilde{\Delta} / \hbar \Omega; \quad l_{pi} = x + 1; \quad \Theta = 1 / \sqrt{1 + 1/2\gamma^2}. \quad (\text{G.4})$$

The asymptotic expression of the PI rate (MPI regime) is given by [82]

$$W_{mpi}^G = s \frac{2\Omega}{9\pi} \left(\frac{m_r \Omega}{\hbar} \right)^{3/2} \phi \sqrt{2 l_{pi} - x} \times \exp \left[2l_{pi} \left(1 - \frac{1}{4\gamma^2} \right) - x \right] \left(\frac{1}{8\gamma^2} \right)^{l_{pi}}. \quad (\text{G.5})$$

More accurate calculation gives the similar expression but with insignificant distinctions

$$W_{mpi}^G = s \frac{\Omega}{8\pi} \left(\frac{m_r \Omega}{\hbar} \right)^{3/2} \left(1 - \frac{2l_{pi} - 1}{8\gamma^2} \right) \phi \left[\left(1 - \frac{1}{8\gamma^2} \right) \sqrt{2 l_{pi} - x} \right] \times \exp \left[2l_{pi} \left(1 - \frac{1}{4\gamma^2} \right) - x \left(1 - \frac{1}{2\gamma^2} \right) \right] \left(\frac{1}{8\gamma^2} \right)^{l_{pi}}. \quad (\text{G.6})$$

Kane band structure

The expression of photo-ionization rate for Kane band structure is [41]

$$W_{pi}^K = s \frac{2\Omega}{9\pi} \left(\frac{m_r \Omega}{\hbar \gamma_2} \right)^{3/2} Q^K \gamma, x \times \exp \left(-\pi l_{pi} \frac{K \gamma_2 - E \gamma_2}{E \gamma_1} \right) \quad (G.7)$$

with

$$Q^K \gamma, x = \sqrt{\frac{\pi}{2K \gamma_1}} \sum_{n=0}^{+\infty} \exp \left(-\pi n \frac{K \gamma_2 - E \gamma_2}{E \gamma_1} \right) \times \phi \left(\sqrt{\pi^2 \frac{2l_{pi} - 2x + n}{2K \gamma_1 E \gamma_1}} \right). \quad (G.8)$$

However, the argument of the Dowson's integral consists misprint, but the argument of the Dowson's integral is correct in the corresponding MPI asymptotic expression. Also, it was independently from us mentioned by Gruzdev [82]. Then, taking into account this fact and the upper limitation to n (discussed in the section 2), we have the following correct expression

$$Q^K \gamma, x = \sqrt{\frac{\pi}{2K \gamma_1}} \sum_{n=0}^{n_{max}} \exp \left(-\pi n \frac{K \gamma_2 - E \gamma_2}{E \gamma_1} \right) \times \phi \left(\sqrt{\pi^2 \frac{l_{pi} - x + n}{2K \gamma_1 E \gamma_1}} \right), \quad (G.9)$$

where

$$\gamma = \frac{\Omega \sqrt{m_r \Delta}}{e E_b}; \quad \tilde{\Delta} = \frac{2\Delta}{\pi \gamma_2} E \gamma_1; \quad x = \tilde{\Delta} / \hbar \Omega; \quad l_{pi} = x + 1; \quad \gamma_1 = \frac{1}{\sqrt{1 + \gamma^2}}; \quad \gamma_2 = \frac{\gamma}{\sqrt{1 + \gamma^2}}. \quad (G.10)$$

The corresponding asymptotic expression (MPI regime) is [41]

$$W_{mpi}^K = s \frac{2\Omega}{9\pi} \left(\frac{m_r \Omega}{\hbar} \right)^{3/2} \phi \sqrt{2 l_{pi} - x} \times \exp \left[2l_{pi} \left(1 - \frac{1}{4\gamma^2} \right) \right] \left(\frac{1}{16\gamma^2} \right)^{l_{pi}}. \quad (G.11)$$

More accurate calculation gives the similar expression but with insignificant distinctions in pre-exponential factor

$$W_{mpi}^K = s \frac{2\Omega}{9\pi} \left(\frac{m_r \Omega}{\hbar} \right)^{3/2} \left(1 - \frac{7}{8\gamma^2} \right) \phi \sqrt{2 l_{pi} - x} \times \exp \left[2l_{pi} \left(1 - \frac{1}{4\gamma^2} \right) \right] \left(\frac{1}{16\gamma^2} \right)^{l_{pi}}. \quad (G.12)$$

And the effective ionization potential is

$$\tilde{\Delta} \square \Delta + \frac{e^2 E_b^2}{4m_r \Omega^2}. \quad (G.13)$$

Appendix H. Electron-electron collision integral

The sum by \mathbf{k}_3 is simply performed through the conservation momentum law (see Eq. 2.23) and then Eq. (2.26) is given by

$$\left. \frac{\partial f}{\partial t} \right|_{e-e} = \frac{2\pi}{\hbar} \sum_{\mathbf{k}_1, \mathbf{k}_2} |M_{e-e}(\mathbf{k}, \mathbf{k}_2)|^2 \Phi(\mathbf{k}_1, \mathbf{k}, \mathbf{k}_2, \mathbf{k}_3) \delta(\varepsilon_{\mathbf{k}_3} + \varepsilon_{\mathbf{k}_2} - \varepsilon_{\mathbf{k}_1} - \varepsilon_{\mathbf{k}}), \quad (\text{H.1})$$

where $\mathbf{k}_3 = \mathbf{k}_1 + \mathbf{k} - \mathbf{k}_2$.

We use the following expression to replace the sum by integral

$$\sum_{\mathbf{k}} \rightarrow \frac{V}{2\pi^3} \int_{\mathbf{k}} d\mathbf{k}. \quad (\text{H.2})$$

Then the collision integral eq. (H.2) is

$$\left. \frac{\partial f}{\partial t} \right|_{e-e} = \frac{2\pi}{\hbar} \left(\frac{V}{2\pi^3} \right)^2 \int_{\mathbf{k}_1} d\mathbf{k}_1 \int_{\mathbf{k}_2} d\mathbf{k}_2 |M_{e-e}(\mathbf{k}, \mathbf{k}_2)|^2 \times \Phi(\mathbf{k}_1, \mathbf{k}, \mathbf{k}_2, \mathbf{k}_3) \delta(\varepsilon_{\mathbf{k}_3} + \varepsilon_{\mathbf{k}_2} - \varepsilon_{\mathbf{k}_1} - \varepsilon_{\mathbf{k}}). \quad (\text{H.3})$$

To simplify next calculation we introduce the following notations:

$$C = \frac{2\pi}{\hbar} \left(\frac{V}{(2\pi)^3} \right)^2, \quad \text{and since the } |M_{e-e}(\mathbf{k}, \mathbf{k}_2)|^2 = \left(\frac{e^2}{\partial_0 N \Omega_0} \frac{1}{\mathbf{k} - \mathbf{k}_2^2 + q_0^2} \right)^2, \quad \text{therefore}$$

$$|M_{e-e}(\mathbf{k}, \mathbf{k}_2)|^2 = |M_{e-e}(\boldsymbol{\kappa})|^2, \quad \text{where } \boldsymbol{\kappa} = \mathbf{k} - \mathbf{k}_2 \text{ and } |M_{e-e}(\boldsymbol{\kappa})|^2 = |M_{e-e}(\kappa)|^2.$$

We replace wave vector dependency to absolute value of that due to assumption of isotropic parabolic band. Then, with account of the new notations the Eq. (H.3) is given by

$$\left. \frac{\partial f}{\partial t} \right|_{e-e} = C \int_{\mathbf{k}_1} d\mathbf{k}_1 \int_{\mathbf{k}_2} d\mathbf{k}_2 |M_{e-e}(\kappa)|^2 \times \Phi \times \delta(\varepsilon_3 + \varepsilon_2 - \varepsilon_1 - \varepsilon) \quad (\text{H.4})$$

with

$$\Phi(\mathbf{k}_1, \mathbf{k}, \mathbf{k}_2, \mathbf{k}_3) = \Phi(k_1, k, k_2, k_3) = \Phi, \quad (\text{H.5})$$

$$\text{where } \varepsilon_{\mathbf{k}_i} = \varepsilon_{k_i} = \frac{\hbar^2 k_i^2}{2m_{cb}} = \varepsilon_i.$$

The integration by φ_1 and φ_2 is performed as follows

$$\begin{aligned}
\left. \frac{\partial f}{\partial t} \right|_{e-e} &= C \iiint k_1^2 \sin \theta_1 dk_1 d\varphi_1 d\theta_1 \iiint |M_{e-e}(\boldsymbol{\kappa})|^2 \times \Phi \times \delta(\varepsilon_3 + \varepsilon_2 - \varepsilon_1 - \varepsilon) k_2^2 \sin \theta_2 dk_2 d\varphi_2 d\theta_2 = \\
&= C 2\pi^2 \iint k_1^2 dk_1 d \cos \theta_1 \iiint |M_{e-e}(\boldsymbol{\kappa})|^2 \times \Phi \times \delta(\varepsilon_3 + \varepsilon_2 - \varepsilon_1 - \varepsilon) k_2^2 dk_2 d \cos \theta_2
\end{aligned} \tag{H.6}$$

The next step is integration by $\cos \theta_1$. To perform this action the energy in argument of the delta-function corresponded the energy conservation law is replaced by the equation through the wave vector. Also we replace differential $d \cos \theta_1$ by expression through the wave vector with help of momentum conservation law, and the corresponding derivation is $\boldsymbol{\kappa} = \mathbf{k} - \mathbf{k}_2 = \mathbf{k}_3 - \mathbf{k}_1 \Rightarrow \mathbf{k}_3 = \boldsymbol{\kappa} + \mathbf{k}_1$. Then $k_3^2 = \kappa^2 + k_1^2 + 2\kappa k_1 \cos \theta_1 \Rightarrow 2k_3 dk_3 = 2\kappa k_1 d \cos \theta_1$ and $d \cos \theta_1 = \frac{k_3 dk_3}{\kappa k_1}$.

$$\begin{aligned}
\text{Because } \cos \theta_1 &= \frac{k_3^2 - \kappa^2 - k_1^2}{2\kappa k_1} \quad \text{and} \quad -1 < \cos \theta_1 < 1, \quad \text{the integration domain is} \\
-1 < \frac{k_3^2 - \kappa^2 - k_1^2}{2\kappa k_1} < 1.
\end{aligned}$$

Solution of this inequality with respect to κ gives

$$\kappa \in |k_1 - k_3|, k_1 + k_3. \tag{H.7}$$

Thus, the corresponding derivation is

$$\begin{aligned}
\left. \frac{\partial f}{\partial t} \right|_{e-e} &= C 2\pi^2 \int k_1^2 dk_1 \iint k_2^2 dk_2 d \cos \theta_2 \int |M_{e-e}(\boldsymbol{\kappa})|^2 \times \Phi \times \delta\left(\frac{\hbar^2 k_3^2}{2m_{cb}} + \frac{\hbar^2 k_2^2}{2m_{cb}} - \frac{\hbar^2 k_1^2}{2m_{cb}} - \frac{\hbar^2 k^2}{2m_{cb}}\right) \frac{k_3 dk_3}{\kappa k_1} = \\
&= C 2\pi^2 \int k_1^2 dk_1 \iint k_2^2 dk_2 d \cos \theta_2 \int |M_{e-e}(\boldsymbol{\kappa})|^2 \times \Phi \times \frac{2m_{cb}}{\hbar^2} \frac{\delta(k_3 - \sqrt{k_1^2 + k^2 - k_2^2})}{2k_3} \frac{k_3 dk_3}{\kappa k_1} = \\
&= C 2\pi^2 \frac{m_{cb}}{\hbar^2} \int k_1^2 dk_1 \iint |M_{e-e}(\boldsymbol{\kappa})|^2 \times \Phi \times \frac{k_2^2}{\kappa k_1} dk_2 d \cos \theta_2
\end{aligned} \tag{H.8}$$

where $k_3 = \sqrt{k_1^2 + k^2 - k_2^2}$; $k_1^2 + k^2 \geq k_2^2$.

To perform integration by $\cos \theta_2$ we replace the corresponding differential by differential expressed through the wave vector: $\boldsymbol{\kappa} = \mathbf{k} - \mathbf{k}_2 \Rightarrow \kappa^2 = k^2 - 2kk_2 \cos \theta_2 + k_2^2$. Then $2\kappa d\kappa = -2kk_2 d \cos \theta_2$ and $d \cos \theta_2 = -\frac{\kappa d\kappa}{kk_2}$.

$$\begin{aligned}
\text{Because } \cos \theta_2 &= \frac{\kappa^2 - k^2 - k_2^2}{-2\kappa k_2} \quad \text{and} \quad -1 < \cos \theta_2 < 1, \quad \text{therefore the integration domain is} \\
-1 < \frac{\kappa^2 - k^2 - k_2^2}{-2\kappa k_2} < 1.
\end{aligned}$$

Solution of this inequality with respect to κ gives

$$\kappa \in |k_2 - k|, k + k_2 \quad . \quad (\text{H.9})$$

Thus, the corresponding integration derivation is

$$\begin{aligned} \left. \frac{\partial f}{\partial t} \right|_{e-e} &= C \, 2\pi \, \frac{m_{cb}}{\hbar^2} \iint \left(\int_{D_\kappa^{e-e}} |M_{e-e}(\kappa)|^2 \frac{1}{\kappa k_1 k k_2} d\kappa \right) \times \Phi \times k_1^2 k_2^2 dk_1 dk_2 = \\ &= \frac{m_{cb} V^2}{2\pi \hbar^3} \frac{1}{k} \iint_{k_1^2 + k^2 \geq k_2^2} \left(\int_{D_\kappa^{e-e}} |M_{e-e}(\kappa)|^2 d\kappa \right) \times \Phi \times k_1 k_2 dk_1 dk_2 \end{aligned} \quad (\text{H.10})$$

In result of previous steps we have two conditions for κ which are given by eq. (H.7) and eq. (H.9). Intersection of these sets gives integration region, $D_\kappa^{e-e} = |k_1 - k_3|, k_1 + k_3 \cap |k_2 - k|, k + k_2 \quad .$

In Eq. (H.10) we replace the momentum integration by energy integration. Then we can rewrite the *electron-electron* collision integral eq. (2.26) in terms of energy, and the expression is represented as eq. (2.28).

Appendix I. Auger scattering rate

The Auger scattering rate in our model is given by the following expression

$$\begin{aligned}
 \nu_{Auger} \varepsilon, n_e &= \frac{1}{2\pi\hbar^3} \left(\frac{e^2}{\dot{\mathbf{d}}_0} \right)^2 \frac{\hbar^2}{2\Delta} \left(\frac{m_{vb}}{m_0} + 1 \right) \left(\frac{m_{cb}}{\hbar^2} \right)^2 \frac{1}{k} \times \\
 &\times \iint_{\varepsilon_1 - \varepsilon - \varepsilon_2 \geq \Delta} \left(\int_{K_{Auger}} \frac{\kappa^2 d\kappa}{\kappa^2 + q_0^2} \right) F_{Auger}(\varepsilon_1, \varepsilon_2) d\varepsilon_1 d\varepsilon_2
 \end{aligned} \tag{I.1}$$

with

$$\begin{aligned}
 F_{Auger}(\varepsilon_1, \varepsilon_2) &= f(\varepsilon_2) [1 - f(\varepsilon_3c)] [1 - f(\varepsilon_1)] = \\
 &= f(\varepsilon_2) f(\varepsilon_3c) [1 - f(\varepsilon_1)]
 \end{aligned} \tag{I.2}$$

where $K_{Auger} = |k - k_1|, k + k_1 \cap |k_2 - k_3^c|, k_2 + k_3^c$ is the integration region.

References

- ¹ D. Hülsenberg, A. Harnisch, and A. Bismark, *Microstructuring of glasses*. Springer Series in Materials Science (Springer, 2008).
- ² K. Sugioka, M. Meunier, and A. Piqué, *Laser Precision Microfabrication* (Springer, 2010).
- ³ T. Brabec, *Strong Field Laser Physics* (Springer, 2008)
- ⁴ B.C. Stuart, M.D. Feit, A.M. Rubenchik, B.W. Shore, and M.D. Perry, Laser-Induced Damage in Dielectrics with Nanosecond to Subpicosecond Pulses, *Phys. Rev. Lett.* **74** (12) 2248-2251 (1995); DOI: 10.1103/PhysRevLett.74.2248.
- ⁵ H. Varel, D. Ashkenasi, A. Rosenfeld, R. Herrmann, F. Noack, and E.E.B. Campbell, Laser-induced damage in SiO₂ and CaF₂ with picosecond and femtosecond laser pulses, *Applied Physics A* **62** (3) 293-294 (1996); DOI: 10.1007/BF01575098.
- ⁶ C.B. Schaffer, A. Brodeur, and E. Mazur, Laser-induced breakdown and damage in bulk transparent materials induced by tightly focused femtosecond laser pulses, *Meas. Sci. Technol.* **12** (11) 1784 (2001); DOI:10.1088/0957-0233/12/11/305.
- ⁷ P.S. Tsai, B. Friedman, J. Squier, and D. Kleinfeld, Cutting Tissue With Ultrashort Pulsed Laser Light, *Optics and Photonics News* **15** (7) 24-29 (2004); DOI: 10.1364/OPN.15.7.000024.
- ⁸ M. Lenzner, J. Krüger, W. Kautek, and F. Krausz, Precision laser ablation of dielectrics in the 10-fs regime, *Appl. Phys. A* **68** (2) 369-371 (1999); DOI: 10.1007/s003390050906.
- ⁹ M. Lenzner, J. Krüger, S. Sartania, Z. Cheng, C. Spielmann, G. Mourou, W. Kautek, and F. Krausz, Femtosecond Optical Breakdown in Dielectrics, *Phys. Rev. Lett.* **80** (18) 4076-4079 (1998); DOI: 10.1103/PhysRevLett.80.4076.
- ¹⁰ W. Kautek, J. Krüger, Femtosecond pulse laser ablation of metallic, semiconducting, ceramic, and biological materials, *SPIE Proceedings* **2207** 600 (1994); DOI: 10.1117/12.184768.

-
- ¹¹ C.B. Schaffer, E. Mazur, Micromachining using ultrashort pulses from a laser oscillator, *Opt. Photonics News* **12** (4) 20-23 (2001); DOI: 10.1364/OPN.12.4.000020.
- ¹² W. Liu, O. Kosareva, I.S. Golubtsov, A. Iwasaki, A. Becker, V.P. Kandidov, and S.L. Chin, Femtosecond laser pulse filamentation versus optical breakdown in H₂O, *Appl. Phys.* **B** 76 (3) 215-229 (2003); DOI: 10.1007/s00340-002-1087-1.
- ¹³ C.B. Schaffer, A.O. Jamison, and E. Mazur, Morphology of femtosecond laser-induced structural changes in bulk transparent materials, *Appl. Phys. Lett.* **84** (9) 1441 (2004); DOI: 10.1063/1.1650876.
- ¹⁴ A. Kaiser, B. Rethfeld, M. Vicanek, and G. Simon, Microscopic processes in dielectrics under irradiation by subpicosecond laser pulses, *Phys. Rev.* **B61** (17) 11437 (2000); DOI: 10.1103/PhysRevB.61.11437.
- ¹⁵ T. Apostolova, Theoretical study of sub-to-picosecond laser pulse interaction with dielectrics, semiconductors and semiconductor heterostructures, *Journal of Physics: Conference Series* **113** 012045 (2008); DOI: 10.1088/1742-6596/113/1/012045.
- ¹⁶ T. Apostolova, Y. Hahn, Modeling of laser-induced breakdown in dielectrics with subpicosecond pulses, *J. Appl. Phys.* **88** (2) 1024 (2000); DOI: 10.1063/1.373772.
- ¹⁷ V.E. Gruzdev, Photoionization rate in wide band-gap crystals, *Phys. Rev.* **B75** (20) 205106 (2007); DOI: 10.1103/PhysRevB.75.205106.
- ¹⁸ A.V. Ivanov, Nonlinear light absorption on the surface of a transparent wide-gap crystal: I. Direct interband transitions, *Optics and Spectroscopy* **111** (5) 786-797 (2011); DOI: 10.1134/S0030400X11120101.
- ¹⁹ V.E. Gruzdev, Energy dependence of effective electron mass and laser-induced ionization of wide band-gap solids, *Proc. SPIE* **7132** 713206 (2008); DOI: 10.1117/12.804730.
- ²⁰ Yu.A. Il'inskii, L.V. Keldysh, *Electromagnetic Response of Material Media* (Plenum, New York, 1994).

²¹ C.F. Klingshirm, *Semiconductor Optics* (Springer, 1997).

²² B.K. Ridley, *Quantum Processes in Semiconductors* (Springer, 1999).

²³ D. Du, X. Liu, G. Korn, J. Squier, and G. Mourou, Laser-induced breakdown by impact ionization in SiO₂ with pulse widths from 7 ns to 150 fs, *Appl. Phys. Lett.* **64** (23) 3071 (1994); DOI: 10.1063/1.111350.

²⁴ X. Jing, Y. Tian, J. Zhang, S. Chen, Y. Jin, J. Shao, and Zh. Fan, Modeling validity of femtosecond laser breakdown in wide band gap dielectrics, *Applied Surface Science* **258** (10) 4741–4749 (2012); DOI: 10.1016/j.apsusc.2012.01.070.

²⁵ T. Otobe, First-principles calculations for multiphoton absorption in α -quartz under intense short laser irradiation, *J. Phys.: Condens. Matter* **22** (38) 384204 (2010); DOI:10.1088/0953-8984/22/38/384204.

T. Otobe, K. Yabana, and J.-I. Iwata, First-principles calculation of the electron dynamics in crystalline SiO₂, *J. Phys.: Condens. Matter* **21** (6) 064224 (2009); DOI:10.1088/0953-8984/21/6/064224.

K. Yabana, T. Sugiyama, Y. Shinohara, T. Otobe, and G.F. Bertsch, Time-dependent density functional theory for strong electromagnetic fields in crystalline solids, *Phys. Rev.* **B85** (4) 045134 (2012); DOI: 10.1103/PhysRevB.85.045134.

T. Otobe, M. Yamagiwa, J.-I. Iwata, K. Yabana, T. Nakatsukasa, and G.F. Bertsch, First-principles electron dynamics simulation for optical breakdown of dielectrics under an intense laser field, *Phys. Rev.* **B77** (16) 165104 (2008); DOI: 10.1103/PhysRevB.77.165104.

²⁶ B.C. Stuart, M.D. Feit, S. Herman, A.M. Rubenchik, B.W. Shore, and M.D. Perry, Nanosecond-to-femtosecond laser-induced breakdown in dielectrics, *Phys. Rev.* **B53** (4) 1749-1761 (1996); DOI: 10.1103/PhysRevB.53.1749.

B.C. Stuart, M.D. Feit, S. Herman, A.M. Rubenchik, B.W. Shore, and M.D. Perry, Optical ablation by high-power short-pulse lasers, *J. Opt. Soc. Am.* **B13** (2) 459-468 (1996); DOI: 10.1364/JOSAB.13.000459.

B.C. Stuart, M.D. Feit, S.M. Herman, A.M. Rubenchik, B.W. Shore, and M.D. Perry, Ultrashort-pulse optical damage, *Proc. SPIE* **2714** 616 (1996); DOI: 10.1117/12.240404.

²⁷ S.S. Mao, F. Quéré, S. Guizard, X. Mao, R.E. Russo, G. Petite, and P. Martin, Dynamics of femtosecond laser interactions with dielectrics, *Applied Physics* **A79** (7) 1695-1709 (2004); DOI: 10.1007/s00339-004-2684-0.

²⁸ M. Mero, A.J. Sabbah, J. Zeller, and W. Rudolph, Femtosecond dynamics of dielectric films in the pre-ablation regime, *Appl. Phys.* **A81** (2) 317-324 (2005); DOI: 10.1007/s00339-005-3216-2.

²⁹ J. Jasapara, M. Mero, and W. Rudolph, Retrieval of the dielectric function of thin films from femtosecond pump-probe experiments, *Appl. Phys. Lett.* **80** (15) 2637 (2002); DOI: 10.1063/1.1468893.

³⁰ T.Q. Jia, H.X. Chen, M. Huang, F.L. Zhao, X.X. Li, S.Z. Xu, H.Y. Sun, D.H. Feng, C.B. Li, X.F. Wang, R.X. Li, Z.Z. Xu, X.K. He, and H. Kuroda, Ultraviolet-infrared femtosecond laser-induced damage in fused silica and CaF₂ crystals, *Phys. Rev.* **B73** (5) 054105 (2006); DOI: 10.1103/PhysRevB.73.054105.

³¹ N. Sanner, O. Utéza, B. Bussiere, G. Coustillier, A. Leray, T. Itina, and M. Sentis, Measurement of femtosecond laser-induced damage and ablation thresholds in dielectrics, *Appl. Phys.* **A94** (4) 889-897 (2009); DOI: 10.1007/s00339-009-5077-6.

³² A.A. Manenkov, A.M. Prokhorov, Laser-induced damage in solids, *Sov. Phys. Usp.* **29** (1) 104-122 (1986); DOI: 10.1070/PU1986v029n01ABEH003117.

A.A. Manenkov, Fundamental mechanisms of laser-induced damage in optical materials: understanding after 40-years research, Proc. SPIE **7132** 713202 (2008); DOI: 10.1117/12.805478.

M.J. Soileau, 40 year retrospective of fundamental mechanisms, Proc. SPIE **7132** 713201 (2008); DOI: 10.1117/12.804556.

N. Bloembergen, Laser-induced electric breakdown in solids, IEEE J. Quantum Electron. **QE-10** (3) 375-386 (1974); DOI: 10.1109/JQE.1974.1068132.

³³ N.M. Bulgakova, R. Stoian, and A. Rosenfeld, Laser-induced modification of transparent crystals and glasses, Quantum Electronics **40** (11) 966-985 (2010); DOI: 10.1070/QE2010v040n11ABEH014445.

³⁴ J. Zeller, A.J. Sabbah, M. Mero, P.M. Alsing, J. McIver, and W.G. Rudolph, Femtosecond dynamics of highly excited dielectric thin films, Proc. SPIE **5273** 515 (2004); DOI: 10.1117/12.524456.

³⁵ B. Chimier, O. Utéza, N. Sanner, M. Sentis, T. Itina, P. Lassonde, F. Legare, F. Vidal, and J.C. Kieffer, Damage and ablation thresholds of fused-silica in femtosecond regime, Phys. Rev. **B84** (9) 094104 (2011); DOI: 10.1103/PhysRevB.84.094104.

³⁶ S.C. Jones, P. Braunlich, R.T. Casper, X.A. Shen, and P. Kelly, Recent progress on laser-induced modifications and intrinsic bulk damage of wide-gap optical materials, Opt. Eng. **28** (10) 1039-1068 (1989); DOI: 10.1117/12.7977089.

³⁷ E.G. Gamaly, The physics of ultra-short laser interaction with solids at non-relativistic intensities, Physics Reports **508** (4-5) 91-243 (2011); DOI: 10.1016/j.physrep.2011.07.002.

³⁸ H.D. Geiler, Laser energy deposition in insulators, Nucl. Instrum. Meth. Phys. Res. **B65** (1-4) 9-20 (1992); DOI: 10.1016/0168-583X(92)95007-E.

-
- ³⁹ A. Mermillod-Blondin, I.M. Burakov, Yu.P. Meshcheryakov, N.M. Bulgakova, E. Audouard, A. Rosenfeld, A. Husakou, I.V. Hertel, and R. Stoian, Flipping the sign of refractive index changes in ultrafast and temporally shaped laser-irradiated borosilicate crown optical glass at high repetition rates, *Phys. Rev.* **B77** (10) 104205 (2008); DOI: 10.1103/PhysRevB.77.104205.
- ⁴⁰ L. Sudrie, A. Couairon, M. Franco, B. Lamouroux, B. Prade, S. Tzortzakis, and A. Mysyrowicz, Femtosecond Laser-Induced Damage and Filamentary Propagation in Fused Silica, *Phys. Rev. Lett.* **89** (18) 186601 (2002); DOI: 10.1103/PhysRevLett.89.186601.
- ⁴¹ L.V. Keldysh, Ionization in the field of a strong electromagnetic wave, *Sov. Phys. JETP* **20** (5) 1307-1314 (1965).
- ⁴² B.H. Christensen, P. Balling, Modeling ultrashort-pulse laser ablation of dielectric materials, *Phys. Rev.* **B79** (15) 155424 (2009); DOI: 10.1103/PhysRevB.79.155424.
- ⁴³ B. Rethfeld, Unified Model for the Free-Electron Avalanche in Laser-Irradiated Dielectrics, *Phys. Rev. Lett.* **92** (18) 187401 (2004); DOI: 10.1103/PhysRevLett.92.187401.
- ⁴⁴ S.I. Anisimov, V.A. Khokhlov, *Instabilities in Laser Matter Interaction* (CRC Press, 1995).
- ⁴⁵ M. Li, S. Menon, J.P. Nibarger, and G.N. Gibson, Ultrafast Electron Dynamics in Femtosecond Optical Breakdown of Dielectrics, *Phys. Rev. Lett.* **82** (11) 2394-2397 (1999); DOI: 10.1103/PhysRevLett.82.2394.
- ⁴⁶ T.E. Itina, M. Mamatkulov, and M. Sentis, Nonlinear fluence dependencies in femtosecond laser ablation of metals and dielectric materials, *Optical Engineering* **44** (5) 051109 (2005); DOI: 10.1117/1.1904591.
- ⁴⁷ L. Jiang, H.-L. Tsai, A plasma model combined with an improved two-temperature equation for ultrafast laser ablation of dielectrics, *J. Appl. Physics* **104** (9) 093101 (2008); DOI: 10.1063/1.3006129.

-
- ⁴⁸ I.H. Chowdhury, A.Q. Wu, X. Xu, and A.M. Weiner, Ultra-fast laser absorption and ablation dynamics in wide-band-gap dielectrics, *Appl. Phys.* **A81** (8) 1627-1632 (2005); DOI: 10.1007/s00339-005-3326-x.
- ⁴⁹ F. Quéré, S. Guizard, and Ph. Martin, Time-resolved study of laser-induced breakdown in dielectrics, *Europhys. Lett.* **56** (1)138-144 (2001); DOI: 10.1209/epl/i2001-00499-9.
- ⁵⁰ S.R. Vatsya, S.K. Nikumb, Modeling of laser-induced avalanche in dielectrics, *J. Appl. Phys.* **91** (1) 344 (2002); DOI: 10.1063/1.1421207.
- ⁵¹ I.B. Bogatyrev, D. Grojo, P. Delaporte, S. Leyder, M. Sentis, W. Marine, and T.E. Itina, Non-linear absorption of 1.3- μm wavelength femtosecond laser pulses focused inside semiconductors: Finite difference time domain-two temperature model combined computational study, *J. Appl. Phys.* **110** (10) 103106 (2011); DOI: 10.1063/1.3662192.
- ⁵² Yu.A. Bychkov, A.M. Dykhne, Breakdown in semiconductors in an alternating electric field, *Sov. Phys. JETP* **31** (5) 928-932 (1970).
- ⁵³ V. Nathan, A.H. Guenther, and S.S. Mitra, Review of multiphoton absorption in crystalline solids, *J. Opt. Soc. Am.* **B2** (2) 294-316 (1985); DOI: 10.1364/JOSAB.2.000294.
- ⁵⁴ Y. Sun, S.A. Boggs, and R. Ramprasad, The intrinsic electrical breakdown strength of insulators from first principles, *Appl. Phys. Lett.* **101** (13) 132906 (2012); DOI: 10.1063/1.4755841.
- ⁵⁵ D. Arnold, E. Cartier, and D.J. DiMaria, Acoustic-phonon runaway and impact ionization by hot electrons in silicon dioxide, *Phys. Rev.* **B45** (3) 1477-1480 (1992); DOI: 10.1103/PhysRevB.45.1477.
- ⁵⁶ D. Arnold, E. Cartier, and D.J. DiMaria, Theory of high-field electron transport and impact ionization in silicon dioxide, *Phys. Rev.* **B49** (15) 10278-10297 (1994); DOI: 10.1103/PhysRevB.49.10278.

⁵⁷ J.M. Ziman, *Electrons and Phonons. The Theory of Transport Phenomena in Solids* (Clarendon Press, Oxford, 2007).

⁵⁸ T. Apostolova, D.H. Huang, P.M. Alsing, J. McIver, and D.A. Cardimona, Effect of laser-induced antidiffusion on excited conduction electron dynamics in bulk semiconductors, *Phys. Rev.* **B66** (7) 075208 (2002); DOI: 10.1103/PhysRevB.66.075208.

⁵⁹ A.M. Nikiforov, A.S. Epifanov, and S.V. Garnov, Heating of nonequilibrium electrons by laser radiation in solid transparent dielectrics, *Journal of Experimental and Theoretical Physics* **112** (1) 160-172 (2011); DOI: 10.1134/S1063776111010134.

S.V. Garnov, A.S. Epifanov, and A.M. Nikiforov, Effect of phonon spectrum heating on the formation of laser-induced electron plasma in wide-gap insulators, *Physics of Wave Phenomena* **20** (2) 81-90 (2012); DOI: 10.3103/S1541308X1202001X.

A.M. Nikiforov, A.S. Epifanov, and S.V. Garnov, Peculiarities of the electron avalanche for the case of relatively large photon energy, *Opt. Eng.* **51** (12) 121813 (2012); DOI:10.1117/1.OE.51.12.121813.

A.S. Epifanov, Avalanche ionization induced in solid transparent dielectrics by strong laser pulses, *Sov. Phys. JETP* **40** (5) 897-902 (1975).

A.S. Epifanov, A.A. Manenkov, and A.M. Prokhorov, Theory of avalanche ionization induced in transparent dielectrics by an electromagnetic field, *Sov. Phys. JETP* **43** (2) 377-382 (1976).

B.G. Gorshkov, A.S. Epifanov, and A.A. Manenkov, Avalanche ionization produced in solids by large radiation quanta and relative role of multiphoton ionization in laser induced breakdown, *Sov. Phys. JETP* **49** (2) 309-315 (1979).

B.G. Gorshkov, Yu.K. Danileiko, A.S. Epifanov, V.A. Lobachev, A.A. Manenkov, and A.V. Sidorin, Laser induced breakdown of alkali-halide crystals, *Sov. Phys. JETP* **45** (3) 612-618 (1977).

⁶⁰ H. Bachau, A.N. Belsky, I.B. Bogatyrev, J. Gaudin, G. Geoffroy, S. Guizard, P. Martin, Yu.V. Popov, A.N. Vasil'ev, and B.N. Yatsenko, Electron heating through a set of random levels in the conduction band of insulators induced by femtosecond laser pulses, *Applied Physics* **A98** (3) 679-689 (2010); DOI: 10.1007/s00339-009-5465-y.

H. Bachau, A.N. Belsky, P. Martin, A.N. Vasil'ev, and B.N. Yatsenko, Electron heating in the conduction band of insulators irradiated by ultrashort laser pulses, *Phys. Rev.* **B74** (23) 235215 (2006); DOI: 10.1103/PhysRevB.74.235215.

⁶¹ B. Rethfeld, Free-electron generation in laser-irradiated dielectrics, *Phys. Rev.* **B73** (3) 035101 (2006); DOI: 10.1103/PhysRevB.73.035101.

⁶² N. Sanner, O. Utéza, B. Chimier, M. Sentis, P. Lassonde, F. Légaré, and J.C. Kieffer, Toward determinism in surface damaging of dielectrics using few-cycle laser pulses, *Appl. Phys. Lett.* **96** (7) 071111 (2010); DOI: 10.1063/1.3309700.

⁶³ N.S. Shcheblanov, T. Derrien, and T.E. Itina, Femtosecond laser interactions with semiconductor and dielectric materials, *AIP Conf. Proc.* **1464** 79-90 (2012); DOI: 10.1063/1.4739862.

⁶⁴ N.S. Shcheblanov, T.E. Itina, Femtosecond laser interactions with dielectric materials: insights of a detailed modeling of electronic excitation and relaxation processes, *Appl. Phys. A* (2012); DOI: 10.1007/s00339-012-7130-0.

⁶⁵ C. Cercignani, *The Boltzmann Equation and Its Applications* (Springer-Verlag, 1988).

⁶⁶ R.L. Liboff, *Introduction to the Theory of Kinetic Equations* (Wiley, 1969).

-
- ⁶⁷ F.G. Bass, Yu.G. Gurevich, Hot Electrons and Strong Electromagnetic Waves in Semiconductors and Gas Discharge Plasma (Nauka, Moscow, 1975) [in Russian].
- ⁶⁸ C. Jacoboni, P. Lugli, The Monte Carlo method for semiconductor device simulation (Springer, 2002).
- ⁶⁹ F.T. Vasko, O.E. Raichev, Quantum Kinetic Theory and Applications. Electrons, Photons, Phonons (Springer, 2005).
- ⁷⁰ M. Lundstrom, Fundamentals of Carrier Transport (Cambridge University Press, 2009).
- ⁷¹ A. Haug, Theoretical Solid State Physics. Volume 1, 2 (Pergamon Press, 1972).
- ⁷² E.M. Epshtein, Scattering electrons by phonons in a strong radiation field, *Sov. Phys. Solid State* **11** (10) 2213-2217 (1970).
- E.M. Epshtein, Effect of a strong electromagnetic wave on the electronic properties of semiconductors. (Survey), *Radiophysics and Quantum Electronics* **18** (6) 579-598 (1975); DOI: 10.1007/BF01036952.
- ⁷³ V.I. Mel'nikov, Quantum kinetic equation for electrons in a high-frequency field, *JETP Letters* **9** (3) 120-122 (1969).
- ⁷⁴ H. Furuse, N. Mori, H. Kubo, H. Momose, and M. Kondow, Phonon scattering of hot electrons in intense mid-infrared laser fields, *Phys. Stat. Sol. (c)* **5** (1) 286-289 (2008); DOI: 10.1002/pssc.200776571.
- ⁷⁵ S.K. Sundaram, E. Mazur, Inducing and probing non-thermal transitions in semiconductors using femtosecond laser pulses, *Nature Materials* **1** (4) 217-224 (2002); DOI:10.1038/nmat767.
- ⁷⁶ A. Kaiser, Energieeinkopplung und -relaxation in Isolatoren bei Bestrahlung mit Subpikosekunden- Laserpulsen (Diplomarbeit) (TU Braunschweig, 1998).

⁷⁷ B. Rethfeld, Mikroskopische Prozesse bei der Wechselwirkung von Festkörpern mit Laserpulsen im Subpikosekundenbereich (Doktorarbeit) (TU Braunschweig, 1999).

⁷⁸ P.T. Landsberg, Recombination in Semiconductors (Cambridge University Press, 2003).

⁷⁹ D.F. Zaretskii, M.M. Yudkevich, Multiphoton intrinsic photoeffect in two-band semiconductors, *Sov. Phys. JETP* **72** (1) 146-150 (1991).

⁸⁰ W.V. Houston, Acceleration of Electrons in a Crystal Lattice, *Phys. Rev.* **57** (3) 184–186 (1940); DOI: 10.1103/PhysRev.57.184.

⁸¹ W.R. Heller, Kinetic-Statistical Theory of Dielectric Breakdown in Nonpolar Crystals, *Phys. Rev.* **84** (6) 1130–1150 (1951); DOI: 10.1103/PhysRev.84.1130.

⁸² V. Gruzdev, Laser-Induced Modification of Energy Bands of Transparent Solids, *AIP Conf. Proc.* **1278** 131-143 (2010); DOI: 10.1063/1.3507096.

V.E. Gruzdev, Analysis of the transparent-crystal ionization model developed by L.V. Keldysh*, *Journal of Optical Technology* **71** (8) 504-508 (2004); DOI: 10.1364/JOT.71.000504

⁸³ D.M. Wolkow, Über eine Klasse von Lösungen der Diracschen Gleichung, *Zeitschrift für Physik* **94** (3-4) 250-260 (1935); DOI: 10.1007/BF01331022.

⁸⁴ V.E. Gruzdev, private communication (2012).

⁸⁵ N.W. Ashcroft, N.D. Mermin, *Solid State Physics* (Saunders College Publishing, 1976).

⁸⁶ G.L. Bir, G.E. Pikus, *Symmetry and Strain-Induced Effects in Semiconductors* (Wiley, 1974).

⁸⁷ P.Y. Yu, M. Cardona, *Fundamentals of Semiconductors* (Springer-Verlag, 2010).

⁸⁸ M.V. Fischetti, Monte Carlo solution to the problem of high-field electron heating in SiO₂, *Phys. Rev.* **B53** (18) 1755-1758 (1984); DOI: 10.1103/PhysRevLett.53.1755.

M.V. Fischetti, D.J. DiMaria, S.D. Brorson, T.N. Theis, and J.R. Kirtley, Theory of high-field electron transport in silicon dioxide, *Phys. Rev.* **B31** (12) 8124-8142 (1985); DOI: 10.1103/PhysRevB.31.8124.

D.J. DiMaria, M.V. Fischetti, Vacuum emission of hot electrons from silicon dioxide at low temperatures, *J. Appl. Phys.* **64** (9) 4683 (1988); DOI: 10.1063/1.341252.

⁸⁹ V.N. Strekalov, The effect of electromagnetic fields on impact ionization, *Sov. Phys. Solid State* **14** (5) 1348 (1973).

V.N. Strekalov, Quantum kinetic equation and change of the threshold condition of impact ionization by the light, *Sov. Phys. Solid State* **15** (5) 930 (1973).

⁹⁰ P.M. Mednis, V.M. Fain, Excitation of cascade ionization in transparent dielectrics by a strong alternating electromagnetic field, *Sov. Phys. JETP* **35** (2) 429-432 (1972).

A.I. Rubinshtein, V.M. Fain, Theory of Avalanche Ionization in Transparent Dielectrics under the Action of a Strong Electromagnetic Field, *Sov. Phys. Solid State* **15** (2) 332-336 (1973).

⁹¹ P.P. Rajeev, M. Gertsvolf, P.B. Corkum, and D.M. Rayner, Field Dependent Avalanche Ionization Rates in Dielectrics, *Phys. Rev. Lett.* **102** (8) 083001 (2009); DOI: 10.1103/PhysRevLett.102.083001.

⁹² H.X. Deng, X.T. Zu, X. Xiang, and K. Sun, Quantum Theory for Cold Avalanche Ionization in Solids, *Phys. Rev. Lett.* **105** (11) 113603 (2010); DOI: 10.1103/PhysRevLett.105.113603.

⁹³ A. Mouskeftaras, S. Guizard, N. Fedorov, and S. Klimentov, Mechanisms of femtosecond laser ablation of dielectrics revealed by double pump–probe experiment, *Appl. Phys. A* (2012); DOI 10.1007/s00339-012-7217-7.

-
- ⁹⁴ V.V. Temnov, K. Sokolowski-Tinten, P. Zhou, A. El-Khamhawy, and D. von der Linde, Multiphoton Ionization in Dielectrics: Comparison of Circular and Linear Polarization, *Phys. Rev. Lett.* **97** (23) 237403 (2006); DOI: 10.1103/PhysRevLett.97.237403.
- ⁹⁵ A.C. Tien, S. Backus, H. Kapteyn, M. Murnane, and G. Mourou, Short-Pulse Laser Damage in Transparent Materials as a Function of Pulse Duration, *Phys. Rev. Lett.* **82** (19) 3883-3886 (1999); DOI: 10.1103/PhysRevLett.82.3883.
- ⁹⁶ J.D. Jackson, *Classical Electrodynamics* (Wiley, New York, 1999).
- ⁹⁷ D.J. Griffiths, *Introduction to Electrodynamics* (Prentice Hall, 1998).
- ⁹⁸ L.D. Landau and E.M. Lifschitz, *Course of Theoretical Physics Vol. 8: Electrodynamics of Continuous Media* (Pergamon, Oxford, 1960).
- ⁹⁹ V.L. Ginzburg, *The propagation of electromagnetic waves in plasmas* (Pergamon Press, 1970).
- ¹⁰⁰ P. Drude, *The Theory of Optics* (Dover Publications, 2005).
- ¹⁰¹ An.V. Vinogradov, Absorption of high-intensity light by free carriers in dielectrics, *Sov. Phys. JETP* **41** (3) 540-543 (1975).
- ¹⁰² An.V. Vinogradov, On the Drude formula for semiconductors, *Sov. Phys. JETP* **43** (3) 521-526 (1976).
- ¹⁰³ P. Audebert, Ph. Daguzan, A. Dos Santos, J.C. Gauthier, J.P. Geindre, S. Guizard, G. Hamoniaux, K. Krastev, P. Martin, G. Petite, and A. Antonetti, Space-Time Observation of an Electron Gas in SiO₂, *Phys. Rev. Lett.* **73** (14) 1990–1993 (1994); DOI: 10.1103/PhysRevLett.73.1990.
- ¹⁰⁴ P. Martin, S. Guizard, Ph. Daguzan, G. Petite, P. D'Oliveira, P. Meynadier, and M. Perdrix, Subpicosecond study of carrier trapping dynamics in wide-band-gap crystals, *Phys. Rev.* **B55** (9) 5799–5810 (1997); DOI: 10.1103/PhysRevB.55.5799.
- ¹⁰⁵ W. Franz, *Handbuch der Physik, Vol. 17, "Dielectric Breakdown"* (Springer, 1956).

J.J. O'Dwyer, *The theory of electrical conduction and breakdown in solid dielectrics* (Clarendon Press, 1973).

S. Whitehead, *Dielectric breakdown of solids* (Clarendon Press, 1951).

M. Levinshtein, J. Kostamovaara, S. Vainshtein, *Breakdown Phenomena in Semiconductors and Semiconductor Devices* (World Scientific, 2005).

V.Ya. Ushakov, *Insulation of high-voltage equipment* (Springer, 2004).

G.I. Skanavi, *Physics of Dielectrics: Region of Strong Fields* (Fizmatlit, Moscow, 1958) [in russian].

J.E. Carroll, *Rate equations in semiconductor electronics* (Cambridge University Press, 1985).

H. Fröhlich, *Theory of dielectrics: dielectric constant and dielectric loss* (Clarendon Press, 1958).

¹⁰⁶ Yu.P. Raizer, *Gas discharge physics* (Springer, 1991).

¹⁰⁷ R.S. Levitskii, E.Yu. Perlin, and A.A. Popov, Multiphoton generation of electron–hole pairs in crystals with deep impurities. I. Two-photon band–impurity transition probabilities, *Journal of Optical Technology* **77** (10) 593-597 (2010); DOI: 10.1364/JOT.77.000593.

R.S. Levitskii, E.Yu. Perlin, and A.A. Popov, Multiphoton generation of electron–hole pairs in crystals with deep impurities. II. Cascade processes, *Journal of Optical Technology* **78** (9) 570-574 (2011); DOI: 10.1364/JOT.78.000570.

A.V. Ivanov, E.Yu. Perlin, Prebreakdown excitation of crystals at double multiphoton resonance: I. Probabilities of interband transitions, *Optics and Spectroscopy* **106** (5) 677-684 (2009); DOI: 10.1134/S0030400X09050099.

A.V. Ivanov, E.Yu. Perlin, Prebreakdown excitation of crystals at double multiphoton resonance: II. Analysis of the effects of transformation of electronic band spectrum, *Optics and Spectroscopy* **106** (5) 685-690 (2009); DOI: 10.1134/S0030400X09050105.

M.A. Bondarev, A.V. Ivanov, and E.Yu. Perlin, Prebreakdown excitation of crystals at double multiphoton resonance: III. Forbidden transitions, *Optics and Spectroscopy* **112** (1) 106-113 (2012); DOI: 10.1134/S0030400X12010043.

E.Yu. Perlin, A.V. Ivanov, and A.A. Popov, Interband phototransitions involving free electrons: I. Crystals with a direct band gap, *Optics and Spectroscopy* **113** (4) 376-382 (2012); DOI: 10.1134/S0030400X12100074.

E.Yu. Perlin, A.V. Ivanov, and A.A. Popov, Interband phototransitions involving free electrons: Part II. Crystals with an indirect band gap, *Optics and Spectroscopy* **113** (4) 383-387 (2012); DOI: 10.1134/S0030400X12100086.

E.Yu. Perlin, K.A. Eliseev, E.G. Idrisov, and Ya.T. Khalilov, Nonlinear absorption of femtosecond light pulses under conditions of multiphoton resonances in solids, *Optics and Spectroscopy* **112** (6) 850-856 (2012); DOI: 10.1134/S0030400X12060148.

E.Yu. Perlin, K.A. Eliseev, E.G. Idrisov, and Ya.T. Khalilov, Nonlinear absorption of femtosecond light pulses accompanying two-photon resonance in bulk crystals and nanostructures, *Journal of Optical Technology* **78** (9) 563-569 (2011); DOI: 10.1364/JOT.78.000563.

A.V. Ivanov, R.S. Levitskii, and E.Yu. Perlin, Multiphoton avalanche generation of free carriers in a multiband crystal, *Optics and Spectroscopy* **107** (2) 255-263 (2009); DOI: 10.1134/S0030400X09080153.

¹⁰⁸ I.S. Grigoryev, E.Z. Meilikhov, and A.A. Radzig, Handbook of Physical Quantities (CRC Press, 1997).

¹⁰⁹ E.D. Palik, Handbook of Optical Constants of Solids (Academic Press, 1985).

¹¹⁰ H. Köster, Jr., K. Hübner, Statistics and transport behavior of electrons in SiO₂, Phys. Stat. Sol. (b) **118** (1) 293-301 (1983); DOI: 10.1002/pssb.2221180135.

Abstract

With the appearance of new ultra-short laser systems, extremely high laser intensities became accessible thus allowing laser treatment of practically all materials. As a result, extremely precise processing techniques are under development considerably extending the number of the corresponding industrial and medical applications. Further progress in this field requires a better understanding of fundamental processes involved in the laser interactions. In addition, the success of several national and international involving the development and use of high power laser systems depends on the capacity of careful definition of damage threshold of their optical components. These points illustrate the importance of a detailed numerical modeling of laser interactions with dielectric materials.

Under laser irradiation, seed electrons appear in the conduction band of dielectric materials due to photo-ionization process. Colliding with a third-body, these electrons are further heated in laser field. When the threshold electron energy is reached, electron-impact ionization begins. At the same time, the considered laser pulses are so short that electron sub-system has no time to reach an equilibrium state. The resulting optical properties are affected and the definition of the damage criterion should be revised. The proposed approach accounts for the non-equilibrium and provides a detailed description of all the involved processes. In particular, we consider the photo- and impact-ionization processes, as well as electron-electron, electron-phonon and electron-ion collisions. The electron energy distribution and heating of electronic and phonon subsystems is discussed. The role of laser parameters (wavelength, pulse duration, fluence) and material properties (energy gap, band structure) is investigated. The thermalization time is calculated and characterizes the non-equilibrium state as a function of laser pulse duration. A novel thermal criterion is proposed for damage definition based on the electron and phonon energies. The calculated damage thresholds are compared with recent experimental findings. An analysis of other criteria (classical optical breakdown and thermal) is also performed.